Summer 2020

A framework for a successful additive repair system

Todd E. Sparks

Recommended Citation

Sparks, Todd E., "A framework for a successful additive repair system" (2020). *Doctoral Dissertations*. 2920.

https://scholarsmine.mst.edu/doctoral_dissertations/2920

A FRAMEWORK FOR A SUCCESSFUL ADDITIVE REPAIR SYSTEM

by

TODD EUGENE SPARKS

A DISSERTATION

Presented to the Graduate Faculty of the

MISSOURI UNIVERSITY OF SCIENCE AND TECHNOLOGY

In Partial Fulfillment of the Requirements for the Degree

DOCTOR OF PHILOSOPHY

in

MECHANICAL ENGINEERING

2020

Approved by

Frank Liou, Advisor
K. Krishnamurthy
Joseph Newkirk
J. Kieth Nisbett
Ashok Midha

ABSTRACT

The goal of this research is to generate a revolutionary improvement to the usability and usefulness of additive repair technology by integrating a set of tools into a seamless work flow. Insufficient automation in the current repair process is a huge hurdle in achieving cost-effective, reliable repairs. Many opportunities have been missed due to inconsistency, quality issues and lack of robustness and flexibility. The present work addresses deficiencies in preparatory steps such as 2D and 3D geometry processing, parameter estimation, and path planning as well as on-machine execution of the path plan. The bulk of the effort is focused on directed energy deposition techniques (DED), however many of the concepts are also applicable to powder bed fusion processes (PBF).

ACKNOWLEDGMENTS

There are quite a few people that I feel the need to acknowledge as being instrumental in getting me to this point:

- I would like to thank my family for the years of patience, love, support, and humor.

- I would like to thank Dr. Frank Liou for his advice and support, as well as for fostering the culture of exploration in LAMP lab in which I thrived.

- I would be remiss in not thanking my other committee members, Dr. Krishnamurthy, Dr. Newkirk, Dr. Nisbett, and Dr. Midha, for putting up with me.

- Finally, I need to thank my fellow LAMP students and PINE employees, whom acted as a sounding board and sanity check on many, many occasions.

TABLE OF CONTENTS

Page

LIST OF ILLUSTRATIONS

LIST OF TABLES

1. INTRODUCTION

Remanufacturing is a production batch process of disassembly, cleaning, and refurbishment (or part replacement) of products at the end of their life [23]. Scrap-material recycling involves separating a product into its constituent materials and reprocessing the materials for use in similar or degraded applications. Both in industry and academia, a significant amount of attention is given to material recycling in which the geometry of the product (and the associated value) is destroyed and only the constituent materials are led into a new cycle of usage. Arguably, a more dramatic reduction in environmental impact can be made by product reuse in which the geometrical form of the product is retained and the product is reused for the same purpose as during its original life-cycle, or for secondary purposes. Many of today's current repair procedures like closing and filling cracks through mechanical pressure or welding, rebuilding worn surfaces using metal spraying and welding, etc. do not lend themselves to automated operations [10]. Manual operations such as Tungsten inert gas (TIG) welding add several variables to the repair process that adversely affect the quality and cost of the finished product. An automated remanufacturing process will be able to offer excellent repair quality and part consistency. Since a remanufacturing system often involves material removal and additive tasks, the study of how to effectively integrate and automate the hybrid process for remanufacturing will substantially impact in the overall environment.

Efforts are being made so that AM processes or materials can be qualified for critical defense or aerospace applications. Furthermore, for naval aircraft, salt water, stack gases, jet exhaust, and austere maintenance conditions combine to form a highly corrosive environment. Therefore the AM restored components for the Navy should possess greater resistance to general corrosion, galvanic corrosion, pitting, exfoliation, stress corrosion cracking, and corrosion fatigue [8]. Traditional repair processes rely on welding or brazing

for material addition. Both of these processes induce a large HAZ (Heat Affected Zone) which can be detrimental to the final part's performance and life. The proposed MMD technology is a process which directly deposits a fully dense metal part without intermediate steps and introduces a much smaller HAZ due to the usage of a high density laser power. This process has been reported to be used in repair of Integrally Bladed Rotors (IBR) [35]. However, lack of automation results in much higher repair cost, and introduces inconsistencies in repair quality, which dramatically reduces the lifetime of the restored parts. These drawbacks have significantly limited the application of the metal repair technology.

An effective part-restoration process for AM process to greatly improve restoration reliability and consistency is needed. A laser metal deposition process is often used to build a 3D part layer by layer, in which material is often injected on a relatively flat surface. The process planner or controller for such additive applications is based on parallel slicing information. However, for a damaged part, the geometric shape is unpredictable; thus, the traditional algorithms in layered manufacturing are not suitable for restoration. Another challenge in restoration is to identify the damaged portion of the part. In order to automate the restoration process, an effective process planner to drive the remanufacturing process is greatly needed. The restoration process should be robust for the quality restoration of various damage conditions.

When approaching a repair task, the first step is to address how best to restore the component geometry based up both the part topology and the nature of the damage necessitating the repair. Realistically, there are two paths to consider:

- Resurface the part. - (Effort $\propto$ Surface Area) This method preserves the existing material. This method is the most efficient way to repair worn surfaces, but it cannot repair deep cracks. Any severe concavities or narrow gaps may prevent this method from being used due to accessibility issues for the laser and powder stream.

- Replace the damaged features. - (Effort $\propto$ Volume) This method requires machining away damaged features, then replacing them via deposition. This is the least material and labor efficient method, but it avoids the accessibility issues via pre-machining.

The core of this work is a framework by which many of the AM process decisions can be made. This framework, discussed in Section 4, is comprised of a engine handles the processing of all computational tasks to achieve some desired result as quickly as possible by scaling to use the available resources. The framework is configured to process various AM-specific functionality, discussed in Sections 5-8, to satisfy a need in a specific AM task. An example of a hybrid AM repair task is included in Appendix 10.

2. LITERATURE REVIEW

Since its inception, rapid prototyping technology has been of interest to various industries that are looking for a process to produce a part directly from a CAD model with minimal manual operations. Directed energy deposition (DED) processes offer a path to directly manufacture fully dense metal parts without intermediate steps. DED processes typically uses metal powders or wire as the build material. In a powder-based DED process, metal powder is injected into a laser- generated melt pool which quickly solidifies into metal layers [14, 16, 26]. A hybrid DED process combines a powder or wire DED process with a material removal process, typically CNC milling [5]. The Laser the Aided Manufacturing Process (LAMP) at Missouri University of Science and Technology (MST) has developed a five-axis hybrid system which integrates material deposition and removal processes [19–22, 36–38, 41, 42]. The system combines both deposition and machining in a single set–up which eliminates part re-setup, providing a significant advantage in the repair process. In more recent years, hybrid DED technology has seen several commercial implementations, such such as DMG-Mori Seiki's Lasertec 65, Mazak's INTEGREX i-400 AM, and Hybrid Manufacturing Technology's AMBIT system [13].

Remanufacturing is a production batch process of disassembly, cleaning, and refurbishment (or part replacement) of products at the end of their life [23]. A dramatic reduction in environmental impact can be made by product reuse in which the geometrical form of the product is retained and the product is reused for the same purpose as during its original life-cycle, or for secondary purposes. Many of today's current repair procedures like closing and filling cracks through mechanical pressure or welding, rebuilding worn surfaces using metal spraying and welding, etc. do not lend themselves to automated operations [10]. Manual operations such as Tungsten inert gas (TIG) welding add several variables to the repair process that adversely affect the quality and cost of the finished product. If a part can

be repaired and reused for its initial product function, not only will the material waste and amount of landfill be reduced, but also energy and matter consumption during manufacture will be reduced because existing components are utilized. In addition, the utilization of existing components reduces the enterprise's costs associated with producing or acquiring new components. Therefore, the impact of part repair is on multiple fronts [2, 10, 12, 15]. An automated remanufacturing process will be able to offer excellent improved consistency over a manual process. Since a remanufacturing system often involves material removal and additive tasks, a hybrid DED process is a good candidate to enable a "circular economy" of continuously restored materials [17].

Hybrid DED equipment is capable of the operations necessary to implement quality repairs to metal components, however there is a gap in the existing knowledge base for precisely how to string together the operations into a coherent repair process. For example, Onuike, et al demonstrated an effective repair of an Inconel 718 part using a hybrid process, but commented on difficulties with repair site preparation and the inhomogeneity of their resultant material, citing a need for further parameter and build orientation optimizations [30]. Finding an optimized parameter set and implementing a qualification procedure for for AM repair activities involves a rigorous process investigation into key AM system process variables and their allowable ranges [33]. A rapid probabilistic qualification procedure involving a collaboration between experimental and modeling efforts was proposed by Peralta, et al in an attempt to shortcut the costly and time consuming AM qualification process [32].

Parameter optimization in AM in general and DED in specific can be a complicated mutli-objective optimization problem that can be addressed in a variety of ways. Concentrations of thermal energy from scan path choices made by the computer aided manufacturing (CAM) system affect the stress distribution in the resulting part[29, 44]. The CAM system can alter path strategies to affect the spread of heat input, which can be used to mitigate stresses induced by thermal concentrations [29]. An analysis of the CAM's path plan's mean

line length can be a useful predictor for the resulting mechanical properties of a printed component [6]. Finite element analysis can be used to model the relationships between the thermal history of an AM build and the resulting microstructure and mechanical properties [25, 47]. Data fusion models, such as the statistical process control and quality monitoring system proposed by Grasso, et al combine data from in-situ monitoring via support vector machines (SVM) to perform classification for process status decisions [11]. SVM is a deep learning technique used to segment a high order data cloud into meaningful groups. In AM, it is often employed to do in-situ categorization of process status [4, 39]. This menagerie of tools and disparate work flows is what this work seeks to unify into a framework to advance the applications of additive manufacturing.

3. MOTIVATION

Metal additive manufacturing is *difficult*. Since the "tool" is generally a laser or electron beam, there is no guaranteed contact position with the workpiece. Heat transfer during the process is hopelessly non-steady state, which makes the consistency of the resultant material a constant object of concern. The rate at which events occur during processing tends towards conditions that are outside most available metallurgical data. The potential to produce or repair functional, high-value metal components on-demand via a digitally driven process is significant enough to make addressing these issues worthwhile.

The majority of Directed Energy Deposition (DED) process developments began with a simple CNC machine style motion system and the ability to toggle a laser and material feed system. The next evolution was to add some manual controls to allow a process expert to tune the process during operation. Much of the current efforts are focused on closing up the control loops and taking the human live adjustments out. The present document catalogs an attempt to address a set of enabling technologies that both provides a platform for process exploration and allows for finer control and configuration of the AM process.

4. METHODOLOGY

Underpinning the computational end of the repair system is a task processing engine. This engine handles the processing of all computational tasks to achieve some desired result as quickly as possible by scaling to use the available resources. The task processing engine, as seen in Figure 4.1a, is comprised of:

- A task coordination module (orange) is responsible for starting tasks whenever the data for that task is present and the resources for completing it are available.

- A resource monitor (yellow) tracks the number of free CPU cores and the amount of free memory.

- A key:value pair storage system (grey) acts as thread-safe data warehouseing service.

- A list of tasks to be completed (blue) specifies the algorithm to run, the keys from which the input data should be pulled, and what keys should store the output data.

- A list of currently running tasks (green). Each task in the running list is spawned as a separate thread so that they can run in parallel. A running task transacts with the key:value storage for data i/o and is terminated by the task coordination module to free memory upon completion.

Figures 4.1 and 4.2 illustrate an application-neutral example of how the task processing system works. The flow of events would be as follows:

1. Upon initialization, the task system is given a set of tasks to complete, as seen in the "To Do" list in Figure 4.1a.

2. The first task in the list requires no input data from storage and system resources are available, so task coordination module allows it to start.

(a) To Do list seeded with tasks.

(b) The first task is executed, depositing its output data into storage
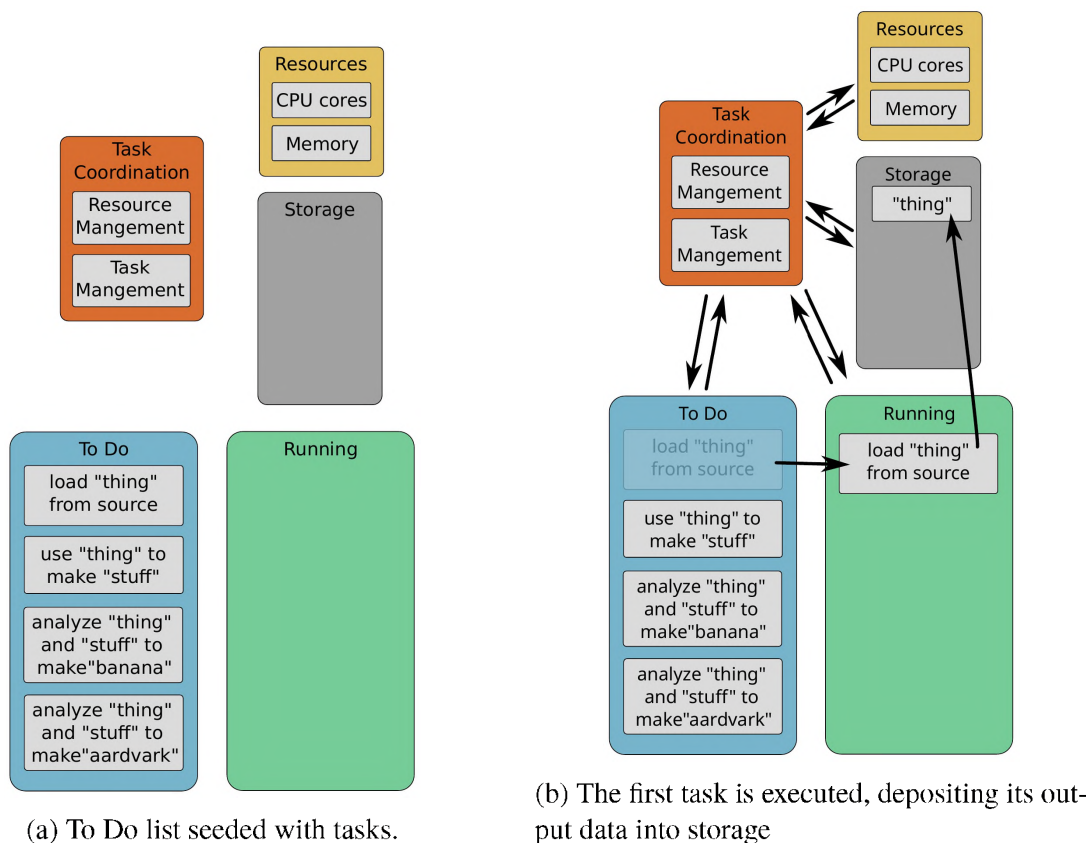
Figure 4.1. Illustrating a simple example of loading a file from disk.

3. The first task executes, which deposits "thing" in the storage, as seen in Figure 4.1b. Having completed its work, this task is then terminated by the task coordination module.

4. As seen in Figure 4.2a, the second task requires "thing", which now exists in the storage. Thus, the task coordinator allows the second task to execute, which deposits "stuff" and is, in turn, terminated.

5. The final two tasks require both "thing" and "stuff", which prevented them from initializing earlier. Now that those entries both exist in storage, these tasks can be allowed to start *simultaneously*. Upon completion, each of these tasks would deposit their output into the shared storage and be terminated, as seen in Figure 4.2b.
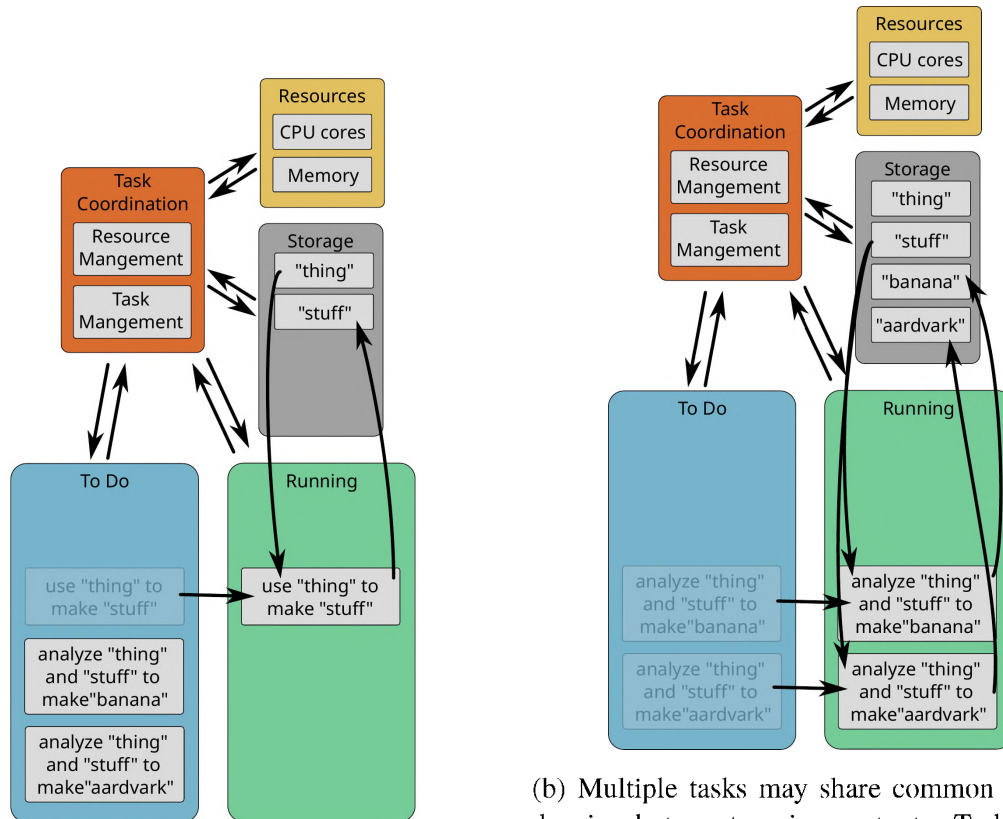
(a) A task with a dependency is allowed to execute once that dependency is met.

(b) Multiple tasks may share common dependencies, but create unique outputs. Tasks sharing dependencies will be executed in parallel if possible.

Figure 4.2. Illustrating task dependencies and parallelism.

With respect to the present repair system, the task processing engine exists as a subsystem within the user-facing control PC. The relationship between the task processing engine and the other logical elements of the system is described in Figure 4.3. This maintains the relationship of the control PC handling the numerically intensive, timing insensitive tasks while the CRio within the MBE controller handles the timing sensitive tasks, such as the triggering of the lasers and powder dispensing systems. Repair-relevant tasks to be handled by the task processing system include:

• Geometry reconstruction from probe data.

• Path planning for additive and subtractive processes
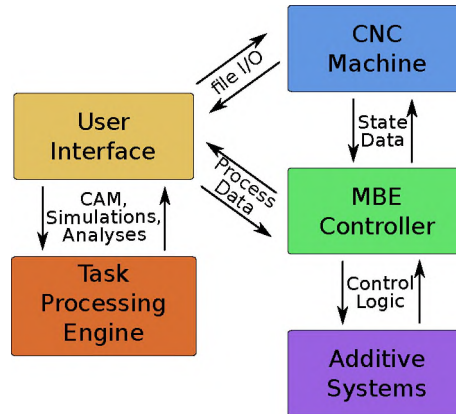
Figure 4.3. The task processing engine provides the CAM, simulation, and geometry processing services needed for the repair system.

- Path sequencing for residual stress minimization

- Comparison of path strategy options

5. GEOMETRY ANALYSES

5.1. DATA FITTING

5.1.1. Voxel Fits. A voxel represents a volume in 3D space, analogous to the way a pixel represents an area in the 2D space of a bitmap image. The simplest voxel representation of a solid object is essentially a 3D boolean array (i.e. a 3D truth table) which describes if each volume represented by a bit is occupied by the component (bit value of 1/True) or not (bit value of 0/False). This conversion procedure is illustrated in Figure 5.1. First, a CAD model (Figure 5.1a) is placed within a bounding set of cubes (Figure 5.1b), each of which map to array indices on the voxel's data structure. Each cube is tested for the presence or absence of the CAD geometry. This information is then recorded as a 1/True or 0/False in the voxel data structure. The resulting voxel model (Figure 5.1c) can be used for any number of operations. For example, collision detection between objects is very computationally cheap to compute in voxel space. Further discussion of voxel model applications can be found in Section 6.4. Figure 5.2 illustrates the basic procedure of a voxel fit figure of merit

(a) An arbitrary shape representing CAD data.

(b) Conversion to a boolean array.

(c) Voxel representation of the CAD data.
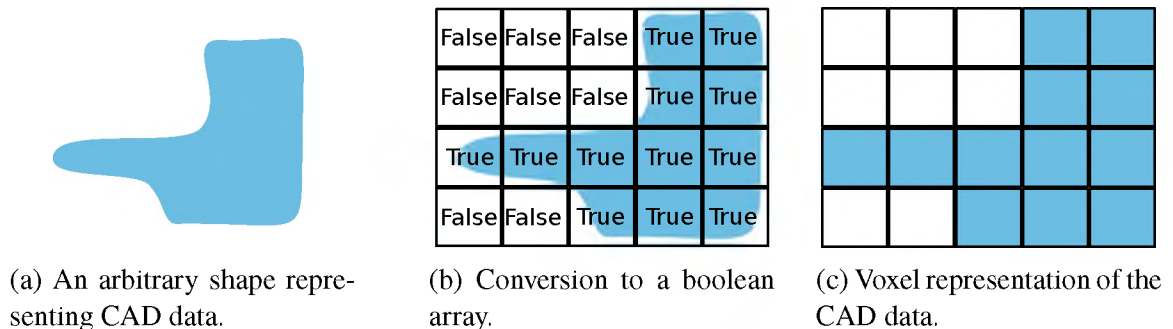
Figure 5.1. Conversion of CAD surface data to a solid voxel representation.

computation. A the original geometry from Figure 5.1a was rotated and translated slightly before being converted to a voxel representation (Figure 5.2a). An AND operator between the original voxel model (Figure 5.1c) and this new model would return a new volume with

the three yellow cells. This would indicate 3 out of the 12 cells in the original model are in agreement with the new model, giving the current orientation a fitness value of 0.25 (i.e. 3/12).

Applying these techniques to the task at hand, a CAD model can be aligned with a scanned model of a real component. Figure 5.3a shows the two models placed, unaligned, into the same space. Red voxels represent the original model. Blue voxels represent the scanned model. Yellow voxels represent the volumes where the models coincide. A Nelder-Mead simplex with six degrees of freedom (X-Y-Z translation and A-B-C rotation) was then used to find the transform necessary to align the two models. Since Nelder-Mead is a minimization technique, the figure of merit used is one minus the fitness described above.
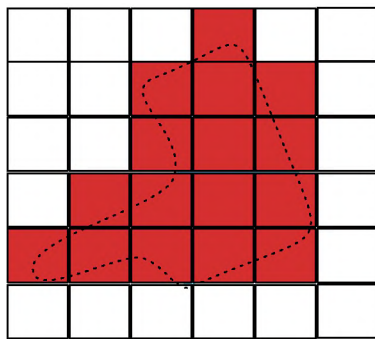
(a) The model from Figure 5.1a in a different orientation.
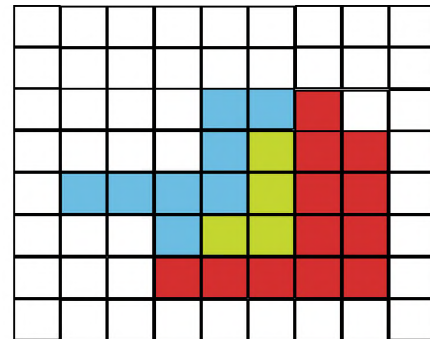
(b) Computed agreement between two models.

Figure 5.2. Computing the agreement between two voxel models.

5.1.2. RANSAC Fitting. RANSAC, or RANdom SAmple Consensus, is a method of fitting data to a model that is extremely robust at removing outlier data (e.g. measurement noise or part damage in the case of a repair task). RANSAC is an interative method that compares models generated from random subsets of the input data. The RANSAC methodology assumes that a given data set is composed of inliers (i.e. "good" data points) and outliers (i.e. erroneous points which should not be included in a model fit). By

<div style="text-align:center">(a) Unaligned models.   (b) Aligned models.</div>
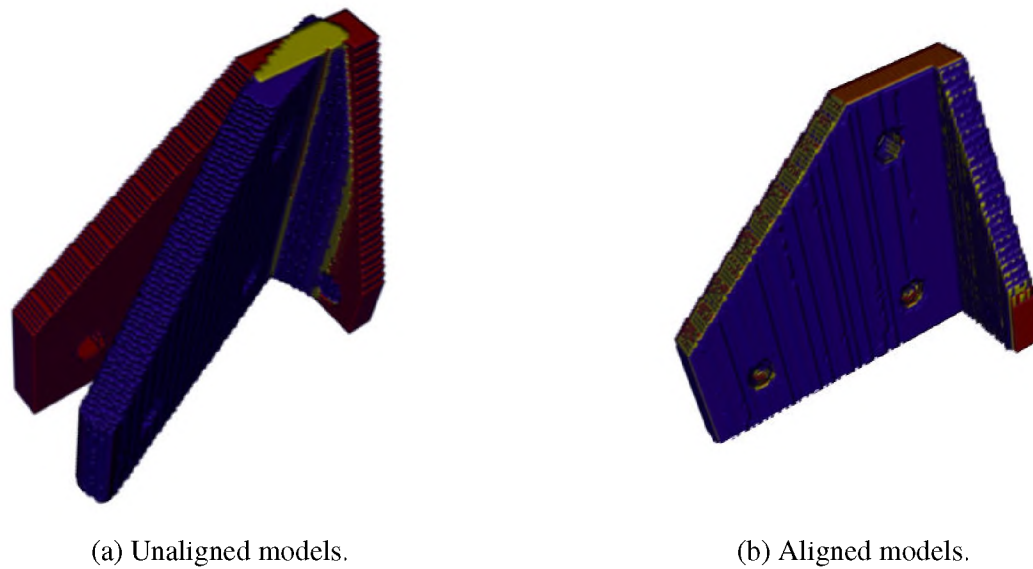
Figure 5.3. Voxel-based fitting methodology demonstration - Red voxels are members of the CAD model. Blue voxels are members of the reverse-engineered model. Yellow voxels represent areas where the two voxel models overlap.

randomly sampling points from the data set to create a model, RANSAC is attempting to create model parameters from a data subset that does not include any of the outlier points. After each random model parameter estimation, the model's fitness is tested.

Model fitness is generally determined by the number of points in the original data set that fits the model. In this way, any model that was computed from an outlier point is quickly removed from contention. When a model with good agreement is determined, inliers and outliers are determined by their distance to the idealized model values. Optionally, a model can be further refined by computing the model against all of the inlier values. In this way, a method that is sensitive to outliers, such as a least squares fit method, can be used for the final refinement fit. A comparison of a RANSAC line fit with a more conventional least squares line fit is shown below in Figure 5.4.

Figures 5.5-5.8 illustrate how RANSAC can be applied to an additive repair task. In this example, we will compute the additive tool paths needed to repair an erroneous drill mark on an arbitrary planar surface. The damaged surface (Figure 5.5a) was first

(a) A least squares line fit to a randomly generated data set representing a line and noise.

(b) RANSAC line fit to the same data set.
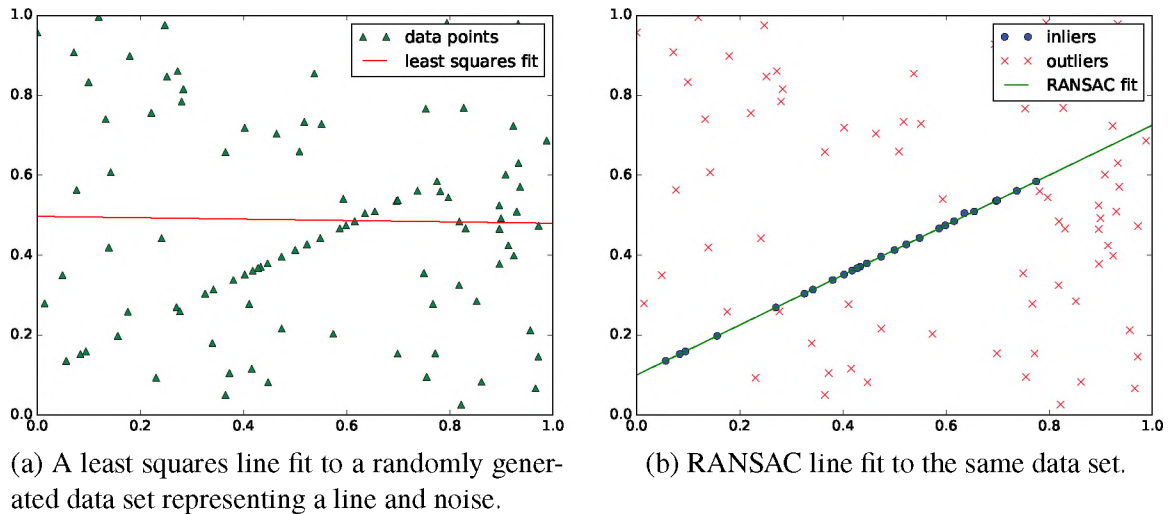
Figure 5.4. RANSAC demonstration of a line fit to a data set with many outliers.

scanned with a Shining3d OptimScan-5M Metrology 3d Scanner at Missouri S&T (Figure 5.5b). This scanned surface data is then passed to a RANSAC plane fitting routine, which returns the fit plane, as well as the inliers and outliers , as seen in Figure 5.6. From the inlier/outlier classification from the RANSAC fit, the geometry of the component's surface and the damage surface an be extracted from the scan data by comparing inlier/outlier membership in the facets of the STL surfaces, as seen in Figure 5.7.

The extracted defect model from Figure 5.7b, along with the plane definition from the RANSAC fit in Figure 5.6, can now be used to do path planning for repairing the defect. First, the model is sliced along the plane normal, as seen in Figure 5.8a. From slice information, a 2D path plan can be created for each slice. Figure 5.8b shows a raster infill typical of most additive planning systems. Figure 5.8c shows an offset infill pattern where each successive path is equidistant from the previous. Finally, Figure 5.8d shows a continuous spiral infill pattern. A discussion on 2D path plan patterns is included in Section 7.1.2.
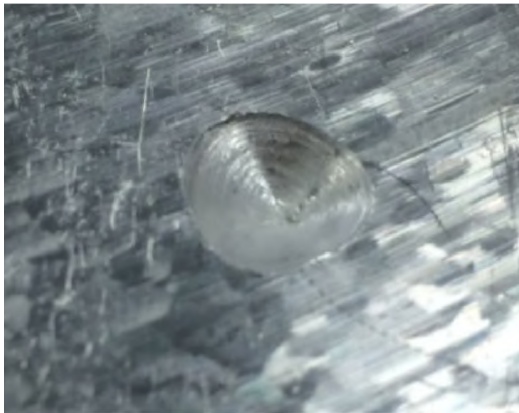
(a) The damage to be repaired: A drill mark on a surface.
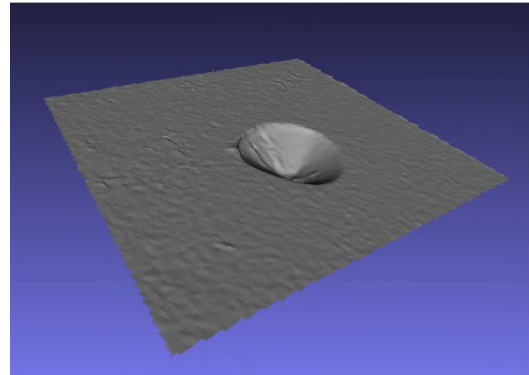
(b) 3d scanned surface of the damaged area.

Figure 5.5. A damaged metal surface and its 3D scanned representation.
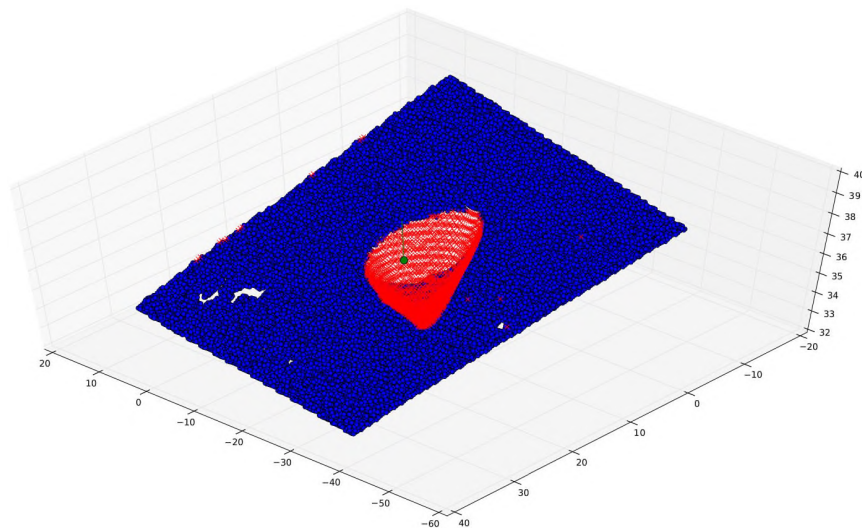
Figure 5.6. Feature extraction via a RANSAC based fitting algorithm: A blue dot indicates a point determined to be part of the original surface while the red X indicates a point that is a member of the defective geometry. A green dot and line indicates a point in the nominal surface's plane as well as its normal direction.

5.2. SUPPORT DESIGN

The first step in the support generation activity is to identify points on the model that require support. This is done by a set of per-vertex, per-edge, and per-facet inspections on the model mesh. Checks are made against three configuration options: support density
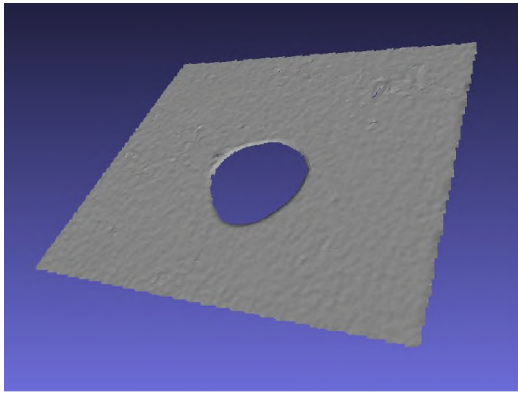
(a) The nominal surface, as extracted from the RANSAC fit data.
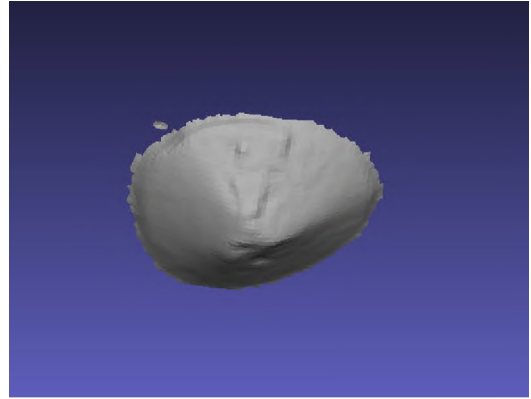
(b) The damage surface, as extracted from the RANSAC fit data.

Figure 5.7. The original scanned surface mesh decomposed by the vertex classification from the RANSAC fitting routine.
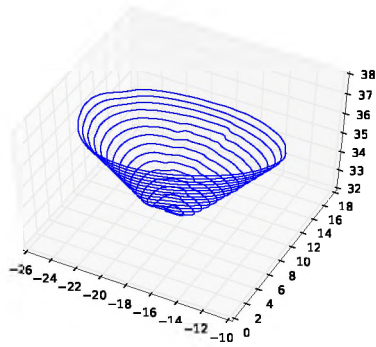
(a) Slices of the extracted damage surface model.
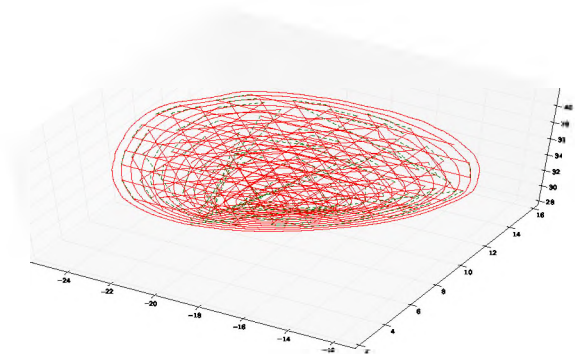
(b) Raster infill with 0°, 45°, 90°, and 135°raster angles.
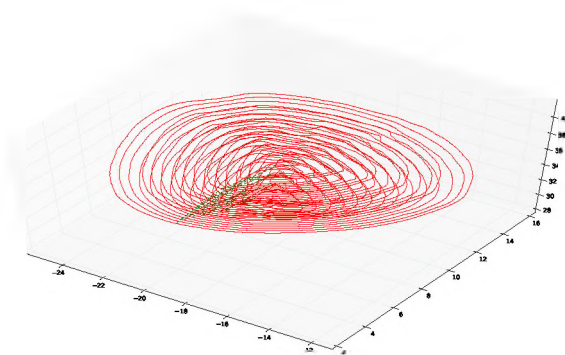
(c) Offset infill.
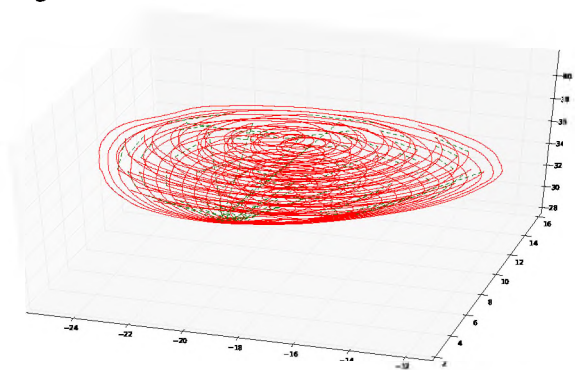
(d) Continuous spiral infill.

Figure 5.8. Slicing and path planning for the repaired volume.

(expressed in supports per mm^3), the overhang capability of the print system (expressed as a limit on the dot product of a normal vector with the -z direction), and a dihedral angle tolerance to ensure good support of sharp or thin features. As illustrated in Figure 5.9, the initial set of support points are curated via the following methodology:

- The vertices laying on the bottom face (floor) of the bounding box are added. This is to ensure the lowest point of the model is always supported.

- Vertex points are included when the vertex normal (defined as the mean of the normals of all the facets the vertex is a member of) meets the overhang requirement for support.

- If at least vertex connected one an edge meets the overhang requirement and the edge's dihedral angle is less than the threshold, points along the edge are added.

- If the facet normal meets the support requirement, the facet area is multiplied by the support density to determine how many support contact points to distribute along the facet surface. If this results in less than one support, a single support is added at the facet centroid.

Each time a point is added to the support contact point list, it is associated with the normal direction that was tested and the status under which it was added (floor, edge, face, etc). After iterating through all the facets in the model, the support point list is generally overpopulated. In fact, some points can be included multiple times for different reasons. In the end, we would not want to populate the same position with multiple supports. To decimate the support, the points are binned spatially by the defined support density, then one support is selected from each bin according to a configurable priority list. The one exception to this is all of the floor points should be included. After this support decimation process, the support contact list is considered complete.
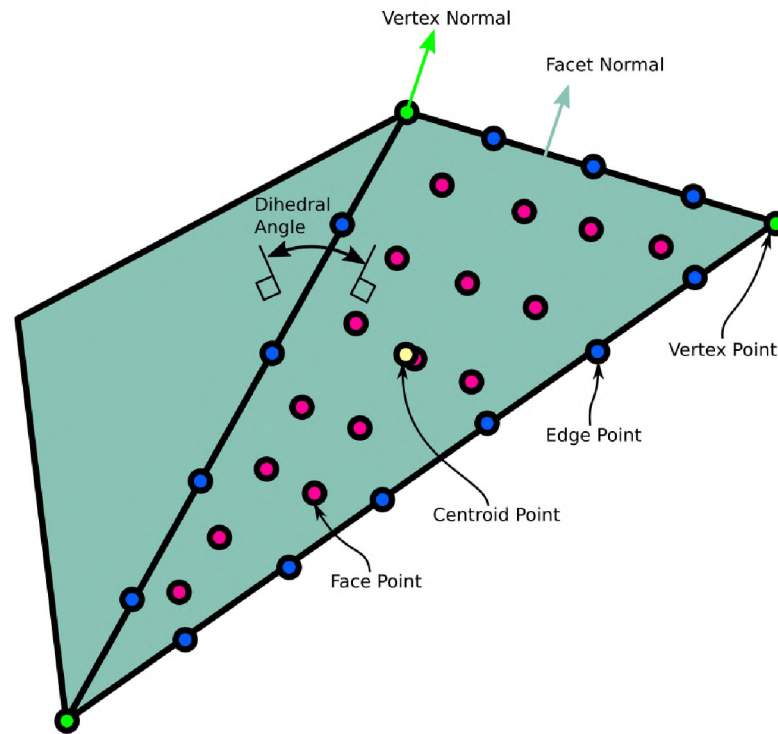
Figure 5.9. Support contact distribution nomenclature.

The support routing activity creates a path for the support to follow from the support contact point to its terminus on either the build plate or the model itself in the case of features where no route can be found to the build plate. Two routing implementations currently exist. Both begin by first adding a route point some configurable distance from the support point in the associated normal direction. After that, the two algorithms diverge:

- *Truncated supports* - The truncated support model is the fastest to compute and the least elegant. The support route is merely projected down until it terminates on either the model or the build plate.

- *Adaptive supports* - The adaptive support routing algorithm computes a path for each support that attempt to avoid model intersections as much as possible. As illustrated in Figure 5.10, the adaptive support algorithms projects the last point in the support

route downwards through successive slices of the model. When an intersection with the part slice is detected, A circle is drawn representing the maximum search area for redirecting the support route. The diameter of this circle is determined by the maximum overhang angle defined for the machine/material profile and the number of layers since the last point was added to the route. The search circle is cut with the current model slice to determine the valid search area for the next point. If no solution can be found, the support is terminated on the model as in the truncated support case. Otherwise, the process continues until the build plate is reached.

Examples of supports created with these routing techniques can be seen in Section 6.6. Parts printed from these models can be observed in Section 5.2.
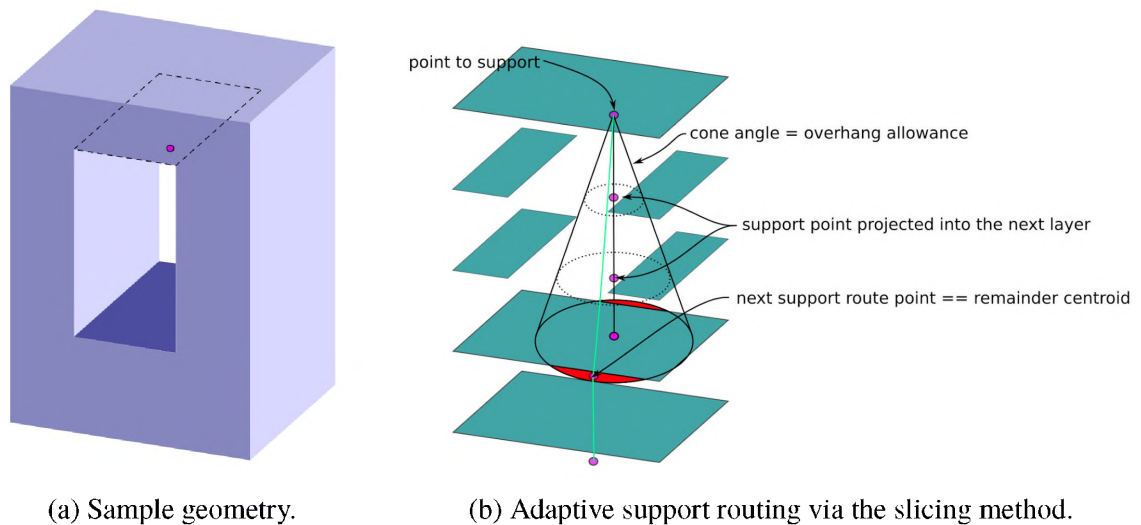
(a) Sample geometry.   (b) Adaptive support routing via the slicing method.

Figure 5.10. The adaptive support routing algorithm computes a path for each support that attempt to avoid model intersections as much as possible.

Supports were created for the three different overhang sizes using a combination of two support generation tools. First, a gyroid infill calculator which can operate on a volume. Second, a point-to-point loft tool which draws in supports at specific positions. The test print included 3 different parameterizations of lofted pin patterns (labeled loft1, loft2, and loft3), a gyroid infill, and a gyroid supported platform with lofted pins. The loft2 pin type

of support consistently produced the best print quality, as you can see in Figure 5.11. The gyroid supported platform with pin supports consistently produced the worst print quality, as observed in Figure 5.12. Of the two path patterns available to the Renishaw AM250 at Missouri S&T, the stripe pattern produced the smoothest result, as observed in Figure 5.13b. The checkerboard pattern seen in Figure 5.13a produced a regular quilt-like texture with significant variation.
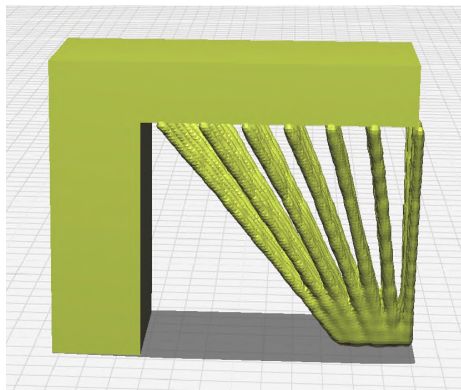
(a) 9.0mm overhand with generated support.
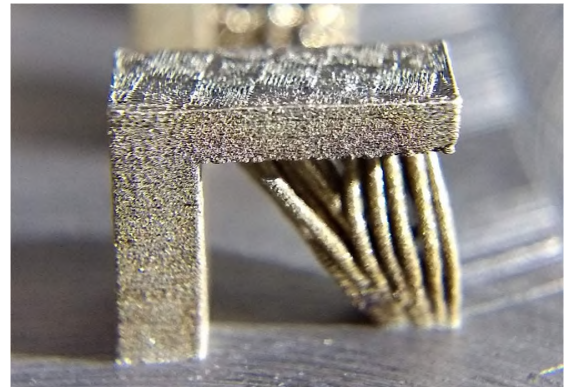
(b) Result after printing and machining away the support.

Figure 5.11. The straight lofted pin supports with 1.25mm contact spacing performed the best in both the stripe and checkerboard infill types.
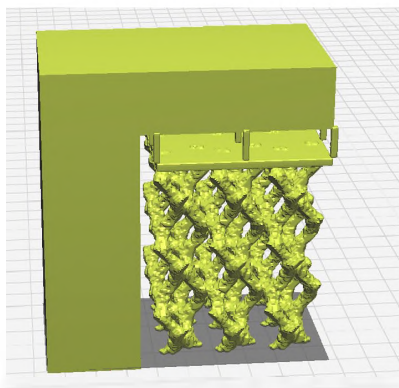
(a) 6.0mm overhand with generated support.
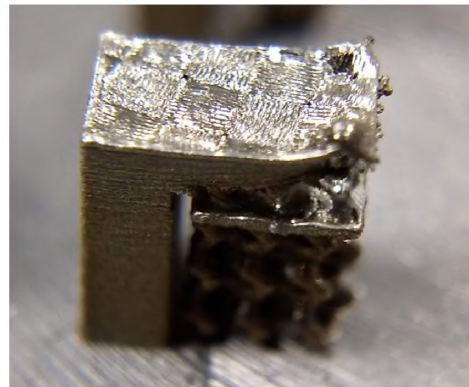
(b) Result after printing and machining away the support.

Figure 5.12. The gyroid platform with lofted pins at a 2mm spacing performed the worst in both the stripe and checkerboard infill patterns.

<div align="center">(a) Checkerboard.   (b) Stripe.</div>
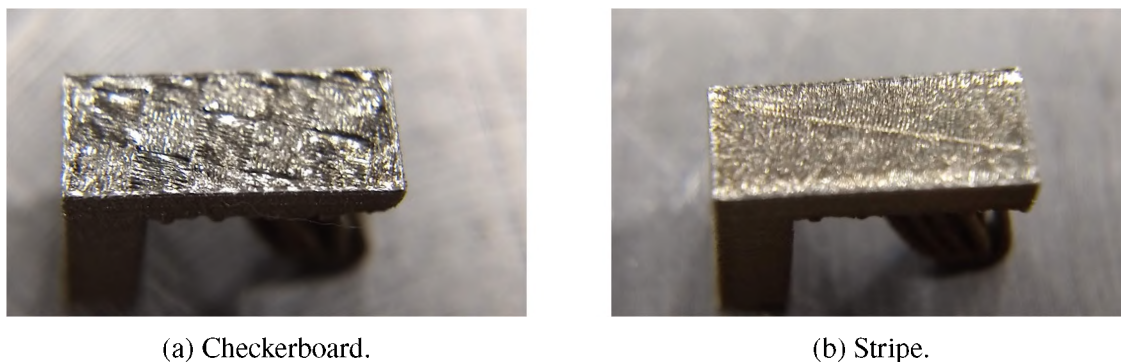
Figure 5.13. Top surface texture comparison for the two infill patterns from the Renishaw build processer in Magics for for Missouri S&T's AM250.

Residual stresses in each part are inferred from a comparison of measurements of the top surface before and after support removal. Support removal was accomplished with a slitting saw on a Haas TM1-P vertical milling machine, as seen in Figure 5.14a. The saw was positioned such that the supports were cut from the underside of the cantilever. The paths were generated using the log file from the scripting that arranged the randomized parts on the build plate. Typical results from the slitting saw operation can be seen in Figure 5.15.

Similarly, the specimen top surfaces were measured via a Wengler OPT2001 laser displacement sensor, seen in Figure 7.12a. The analog output from the sensor was connected to an analog input with a 12bit ADC on the CNC machine controller so that the measurements could be commanded from a CNC macro. Like the slitting saw program, the measurement program was generated from the same log file used to generate the slitting saw paths.

Figures 5.16 and 5.17 show the complete raw data of the scans. In both figures, (a) is the as-printed surfaces while (b) is the surface after machining. The two blue lines per specimen define the best-fit plane of that specimen's surface. From this bird's eye view of the data, we can glean two things:

- The rougher texture of the checkerboard infill pattern can be observed larger Z range of the plots in Figure 5.16 that the Z range of the plots in Figure 5.17.

(a) Support removal was accomplished via a 2" diameter, 3/32in thick slitting saw.
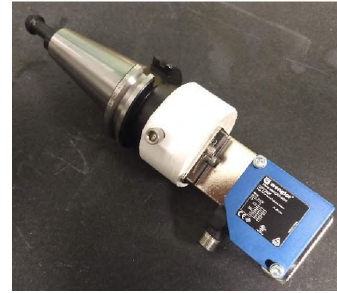
(b) A Wengler OPT2001 laser displacement sensor was used to do all of the height measurements.

Figure 5.14. Data collection for this experiment was accomplished by scanning the top surface of each specimen with the laser displacement sensor both before and after the supports were severed from the cantilever with the slitting saw.

(a) The lower density support structures tended to deflect during the machining operation.

(b) The higher density support structures retained their shape during machining.

Figure 5.15. Typical results from support removal via slitting saw.

• The spikes present in Figure 5.16 correspond to the usage of the support pattern seen in Figure 5.12b.

Figure 5.18 shows the measurement results for the gyroid platform with lofted pins at a 2mm kerboard infill patterns seen in Figure 5.12b for both infill types. The red line represents the best fit surface of the as-printed part. The blue line is the best fit surface for the machined part. The checkerboard infill version seen in Figure 5.18a represents what,

(a) As-printed.

(b) After machining.
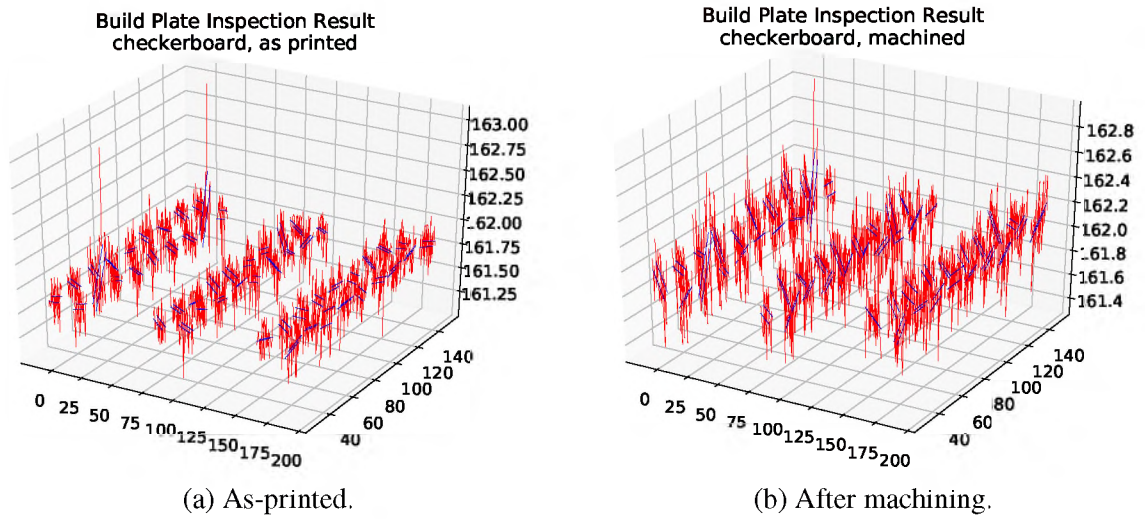
Figure 5.16. Raw measurements for the checkerboard infill pattern.

(a) As-printed.

(b) After machining.
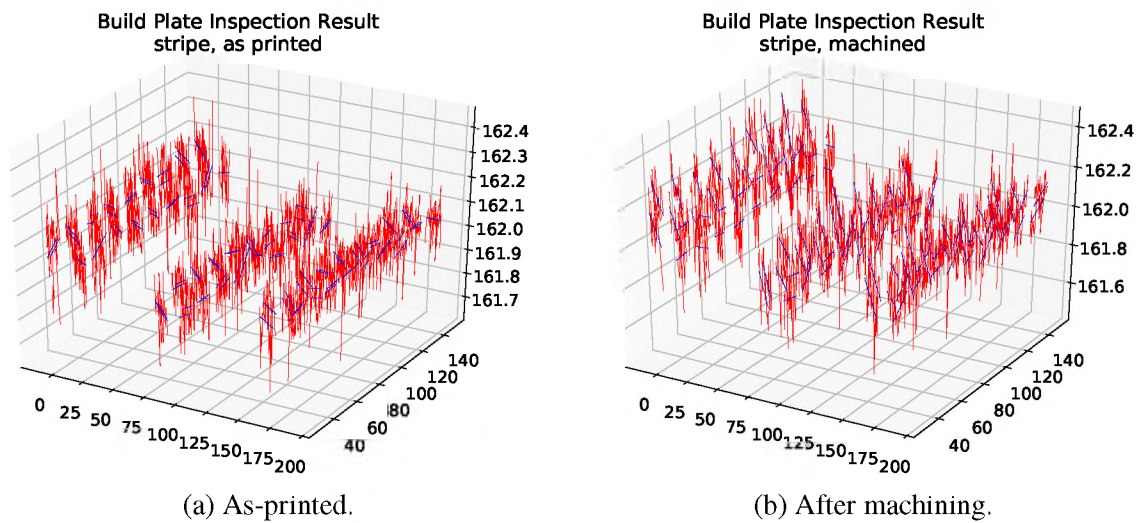
Figure 5.17. Raw measurements for the stripe infill pattern.

based upon *visual* inspection, a human would call the worst result of any print. However, the red and blue best fit lines are very nearly parallel, indicating low deformation when we removed the supports.

446

(a) Checkerboard infill. (b) Stripe Infill.
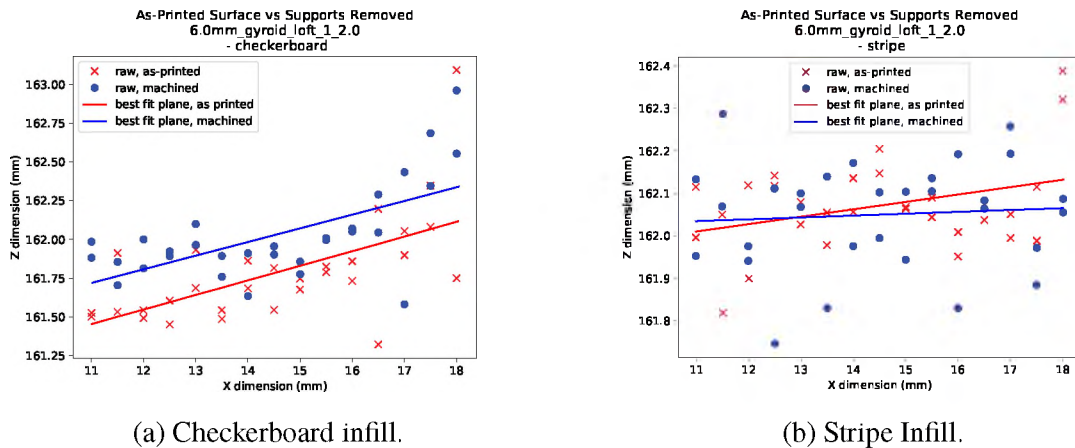
Figure 5.18. Comparison of the two infill styles for the 6.0mm overhang with the gyroid loft style supports.

Similarly, 5.19 shows the measurement results for the lofted pin pattern specimens. The specimen shown in Figure 5.19b is *visually* the best result, however it does show some shift in surface orientation after removing the supports. When looking a this change in angle for a larger number of specimens, such as the 6mm specimens shown in Figure 5.20, we can see that, while the range stays approximately the same, the mean shift in angle is less for the checkerboard infill type than for the stripe infill type. This corresponds to the notion that mean line length in a 2d path plan is proportional to in-plane stresses, which was uncovered during a literature review during the Phase I Option.

(a) Checkerboard infill.

(b) Stripe Infill.
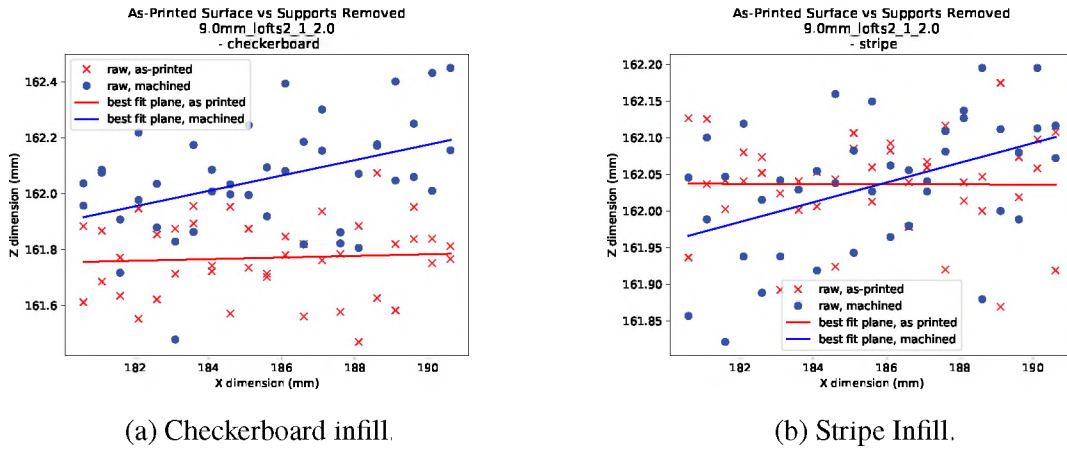
Figure 5.19. Comparison of the two infill styles for the 9.0mm overhang with the lofted straight pin style supports.

(a) Checkerboard infill.

(b) Stripe Infill.
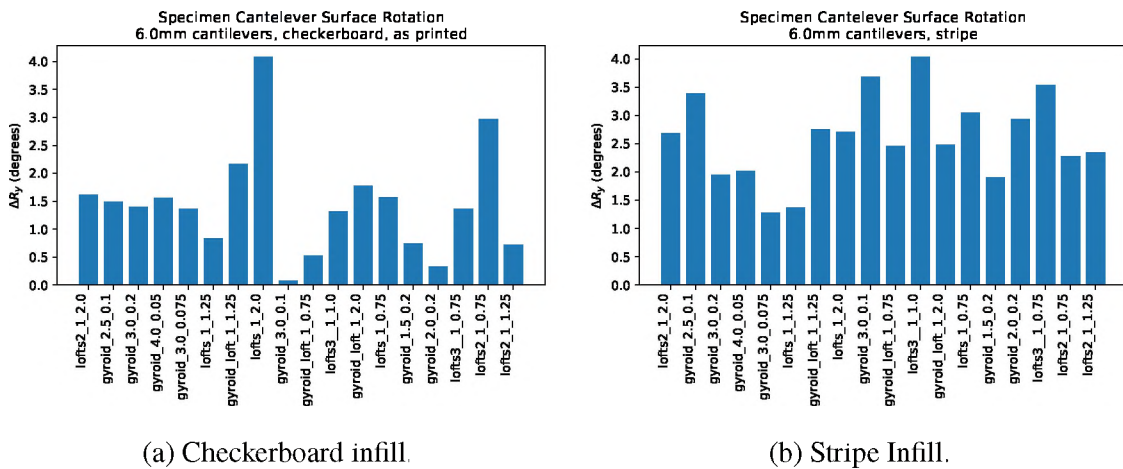
Figure 5.20. ΔR_y for all 6mm specimens.

6. GEOMETRY MANIPULATION

6.1. GEOMETRY DECOMPOSITION FOR AM APPLICATIONS

Process planning for non-powder bed metal additive systems with 4+ axes of articulation is still in its infancy. Multiaxis machines unlock the possibility of building components without support structures (or at the very least minimizing them). The missing link is the planning tools for machine operators to use to create process plans to take advantage of the available machine architectures.

6.1.1. Procedural Decomposition for Multi-axis Applications. Existing additive process planners for 3 axis processes require support structures for any unsupported geometry. These support structures must be made of a material than can survive the processing environment and is compatible with the part material. Typically this means that the support will be made of the same material as the part. The support structure solution adds cost due to an increased volume of deposition and to increased machining necessary to remove the support. The desire to avoid machining large volumes of material is generally a major factor in choosing to produce a component by additive means, so you can see how this is an undesirable characteristic of an additive process plan.

The decomposition methodology divides geometry of a target component into substructures suitable for additive manufacturing. Each substructure is defined as a geometry that is accessible from a set of view angles, θ, from a known starting surface, as indicated in Figure 6.1. The view angle parameter θ is used to accommodate various process capabilities to create overhanging geometry and is defined as the allowed deviation from surface normal. Each decomposition step proceeds piece-wise fashion as defined by a geometry interrogation interval, δ. The geometry processing procedure for this method proceeds as follows:

1. Initialze the procedural decomposition process with:

    • Model geometry, G_{model}

    • An empty set of subcomponents g_i

    • An initial interrogation surface, $S_{interrogation}$, is either a provided input to the algorithm or can be assumed to be the contact surface between the target geometry and pre-existing material.

    • An interrogation surface waiting list, initialized as an empty set, $S_{waiting}$.

2. Equation 6.1 defines an operator P which computes the next inspection volume, $G_{interrogation}$, as a function of the current inspection base surface, $S_{interrogation}$, extruded a distance δ along the build direction $\hat{n}$ with a side wall draft angle θ.

$$G_{interrogation} = P(S_{interrogation}, \delta\hat{n}, \theta) \tag{6.1}$$

3. An intersection volume, $G_{intersection}$, is created by computing the boolean intersection between the interrogation volume and the model geometry, as descrdibed in Equation 6.2.

$$G_{intersection} = G_{model} \cap G_{interrogation} \tag{6.2}$$

4. The next step depends on the status of $G_{intersection}$:

    • If $G_{intersection}$ is empty, the current subcomponent g_i is complete. Initialize g_{i+1} as empty geometry.

    • If $G_{intersection}$ is is populated, update g_i using Equation 6.3 and remove the material from the model via Equation 6.4.

$$g_i = g_i \cup G_{intersection} \tag{6.3}$$

$$G_{model} = G_{model} \cup (\neg G_{intersection} \tag{6.4}$$

5. If G_{model} is empty, the decomposition process is complete.

6. The selection of a new $S_{interrogation}$ is dependent upon the status of the latest g_i:

- If g_i contains material, surface(s) are created using Equation 6.5.

- If g_i is empty (i.e. the previous subcomponent was just completed), a new interrogation surface is needed to start the new subcomponent:

  - If $S_{waiting}$ is not empty, remove the first entry from that list and store it in $S_{interrogation}$

  - If $S_{waiting}$ is empty, a single surface is selected from the result of Equation 6.6, where $G_{removed}$ is the sum of all material removed by the prior decomposition activities. At this step, multiple surface results are common and indicate possible branching geometry. All results after the first are stored in $S_{waiting}$ to serve as the initial interrogaction surface for future subcomponents.

$$S_{continuation} = \Gamma(G_{remainder}, g_i) \qquad (6.5)$$

$$S_{continuation} = \Gamma(G_{remainder}, G_{removed}) \qquad (6.6)$$

$$G_{removed} = \bigcup_{i=1}^{n} g_i \qquad (6.7)$$

7. Return to step 2.

Substructures are iteratively removed from the target component geometry until all of the geometry has been processed. This iteration can be automated or human-guided. Figure 6.3 shows a complete example of the decomposition process carried out on the geometry from Figure 6.1. The sample geometry requires 3 iterations, resulting in 3 separate substructures, as illustrated in Figure 6.2. Each iteration of decomposition method will result in one substructure and 0 or more remaining pieces of geometry.
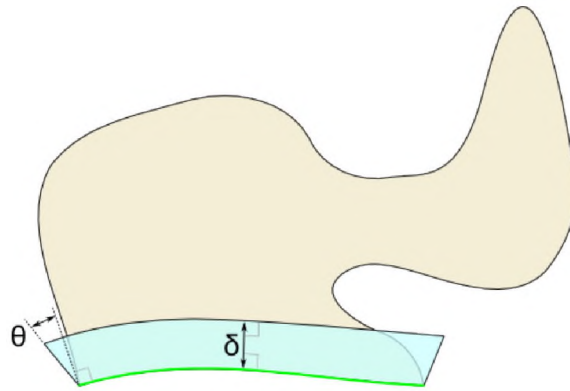
Figure 6.1. Procedural decomposition nomenclature.

6.1.2. Erosion-based Geometry Decomposition. The first decomposition routine developed is based on the image processing erode and dilate operations, as applied to a voxel geometry. The erode operator *shrinks* the solid material by 1 voxel per side. The dilate operator *expands* the material by 1 voxel per side. Decomposing a part via this method requires iterative uses of the erode operator, checking for three possible stop conditions after each iteration:

1. The first condition is a check for a larger than expected reduction in the bound box dimension. As illustrated in Figure 6.4, this is indicative of the removal of a thin portion of the geometry.

2. The second condition, shown in Figure 6.5, is made by counting the number of objects in the voxel volume.

3. The final condition is the trivial result where all of the volume is eroded away before conditions 1 or 2 are triggered. This means the process is done and no further decomposition of the geometry is possible via this algorithm.

After a stop condition is reached, the dilate operator is used to reverse the material removal on the remainder. Finally, boolean operations are used to create the decomposed geometry. Figures 6.6a-6.6b show this process applied to the geometry from Figure 6.4.
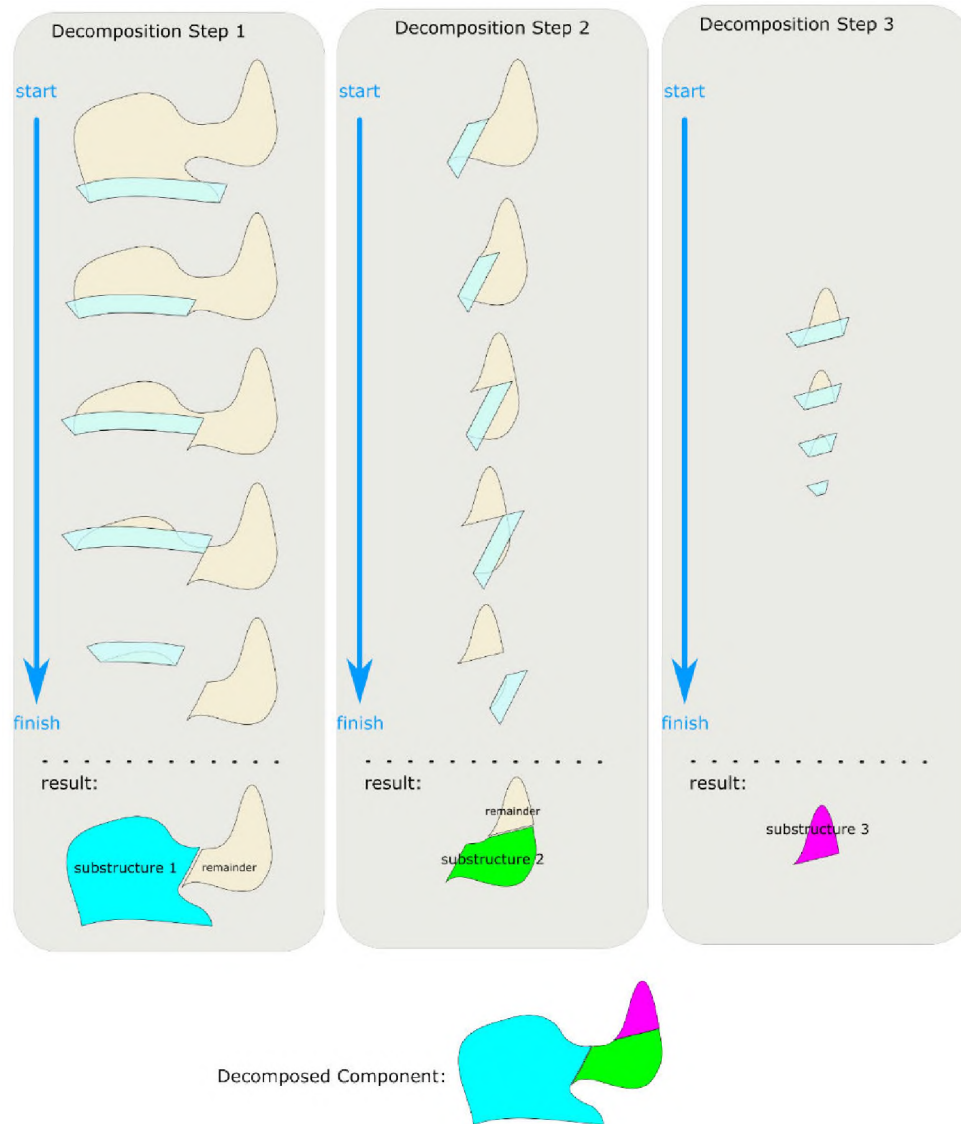
Figure 6.2. Decomposition process example.

Figures 6.6c-6.6d show this process applied to the geometry from Figure 6.5. The sub-geometry results from the decomposition activities (i.e. the red and blue bits) can, in turn, be recursively passed through the erosion-based decomposition algorithm until everything exits with condition 3, signifying completion.

(a) Starting surface selection.   (b) Final result.
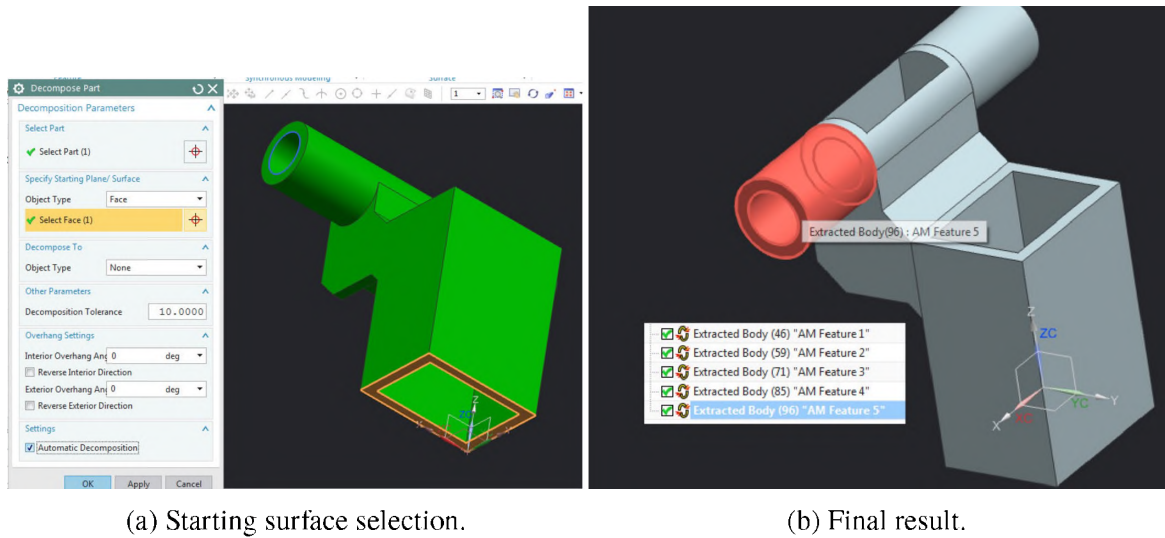
Figure 6.3. A sample implementation of the procedural decomposition method.

(a) Original geometry.   (b) Erode iteration 1.   (c) Erode iteration 2.   (d) Stop condition 1 reached.
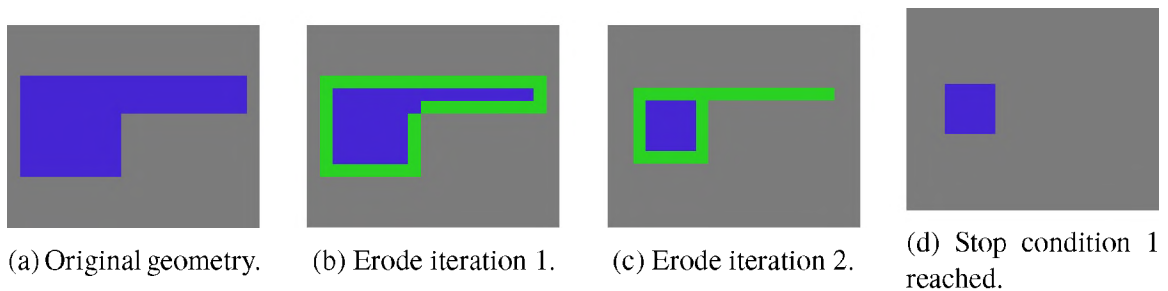
Figure 6.4. Detection condition 1: bound box reduction.

(a) Original geometry.   (b) Erode iteration 1.   (c) Erode iteration 2.   (d) Stop condition 2 reached
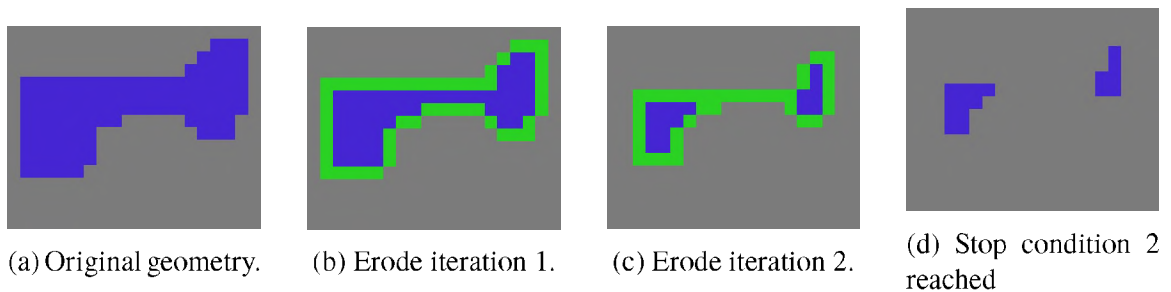
Figure 6.5. Detection condition 2: volume separation.

An example of the complete erosion-based decomposition process was applied to a bracket, seen in Figure 6.7. The original geometry can be seen in Figure 6.7a. The decomposition, noted by the different colors of the sub-geometries, can be seen in Figure 6.7b.

(a) Dilate operation applied.

(b) Boolean operation to separate geometry.

(c) Dilate operation applied.

(d) Boolean operation to separate geometry.
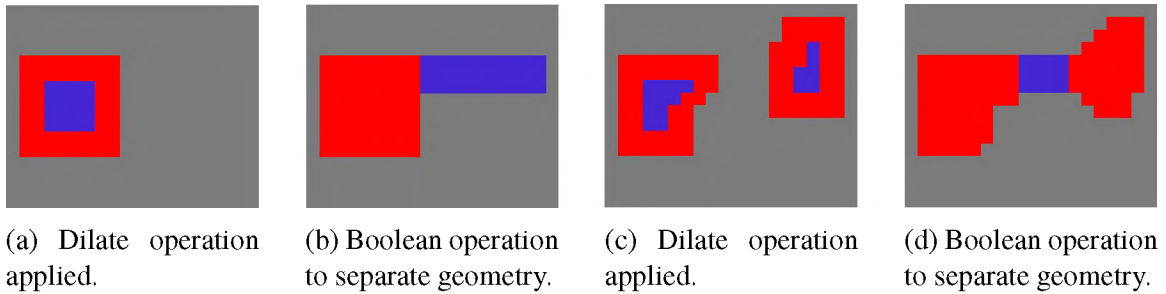
Figure 6.6. Computation of the decomposition result after the detection of a stop condition.

(a) Bracket CAD geometry.

(b) Decomposed bracket.
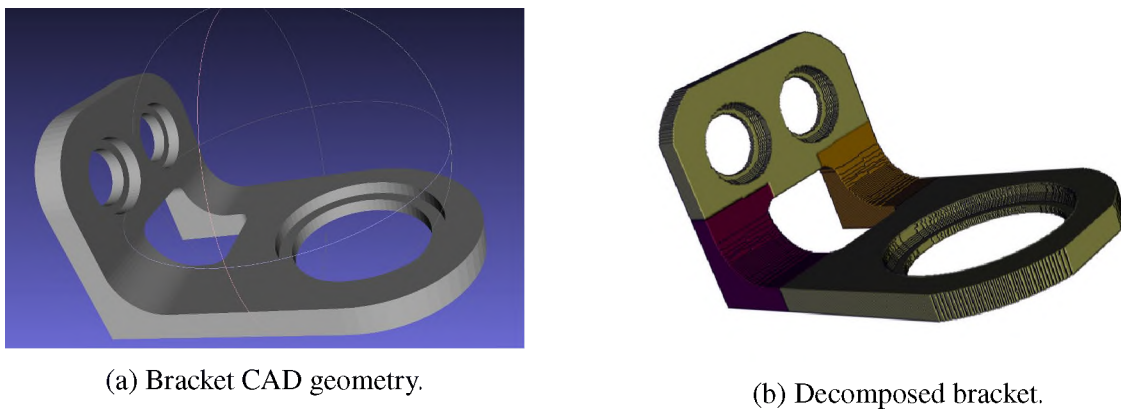
Figure 6.7. Erosion-based decompositon demonstration for a bracket.

6.2. RAFT

In 3D printing, a raft is a structure built to separate the part being printed from the build surface. In FDM printing this is often done to alleviate adhesion and bed leveling issues. For the present purpose, the raft makes removal of the part from the substrate via wire EDM simpler. The raft structure, such as the one shown in Figure 6.8, is computed by projecting the three-dimensional part into a two-dimensional shape, extruding it some amount, then applying the pillaring operation used for the pillared supports to create a raised bed.
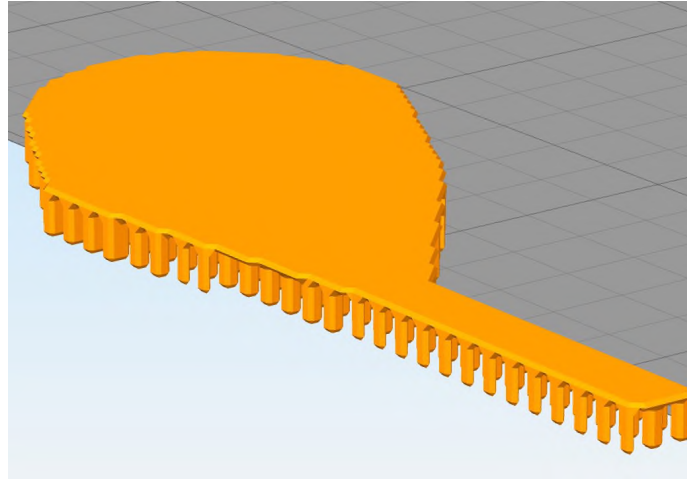
Figure 6.8. Raft structure.

6.3. SHIELD

A class of support structure was devised to protect delicate or thin components from the wiper used to spread powder. This structure type was inspired by the morphologically similar ooze shield used for multi-material FDM printing. The shield is defined as a non-contacting, bounding volume which can be removed from the part after separation from the substrate. The shield structure serves several purposes:

- The shield's primary function is to protect the part geometry from wiper forces.

- The shield provides attachment locations for horizontal supports.

- The shield constrains the non-contact, removable supports.

Initially, the shield was a simple solid structure. However, the solid form of the shield made powder removal difficult. To combat this, two alternate shield forms were devised. First, a shield constructed from a cellular structure, shown in Figure 6.9a, was created from an expanded wire network model propagated through the original solid shield geometry. This cellular form of the shield offers clear attachment points for the horizontal supports and readily allows powder removal. However, the file size of the resultant STL can quickly grow to unmanageable levels, particularly for the Renishaw system used for

demonstration. To make the file size manageable, second shield form was created, shown in Figure 6.9b. This second form uses a set of procedurally generated pillars to suspend a solid shield only in regions near the part.
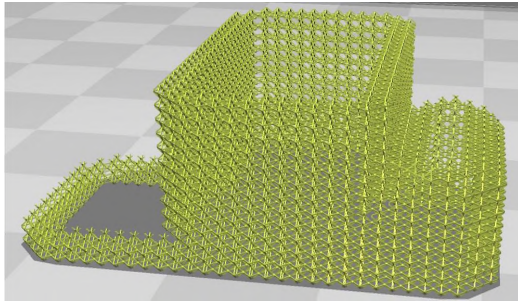
(a) Cellular form of the wiper shield.
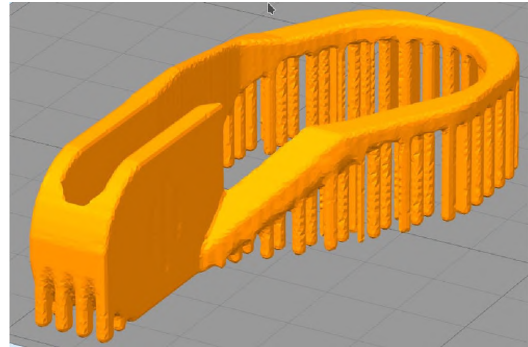
(b) Pillared form of the wiper shield.

Figure 6.9. Wiper shield morphologies.

6.4. TOPOLOGICAL COMPUTATIONS FOR REPAIR AND PRODUCTION 3D PRINTING

Voxel representations of 3D models allow for the usage of image processing techniques to do topological computations. For example, the erode and dilate operators used in binary image processing can be applied in 3 dimensions as well. This allows for extraction of surface-at-depth information from a model. Gaussian filter operators can be used for smoothing. Combinations of these can be used to locate sharp corners or other such details of interest in additive path planning. Computing the degree of similarity between two models can easily be computed by counting the number of voxels that are 1/True in both model's voxel representation. This can be done by simply counting the number of voxels that return 1/True from an AND operation where the two models to be compared are the operands.

Two other useful topological analyses that can be conducted with a voxel-space model representation are the internal volume mask and the clearance volume. Both of these analyses rely upon slice sets taken from 3 mutually orthogonal directions, as seen in Figure 6.10b. Both of these example analyses would not be used for tool path generation, but are rather a source of meta-data that would normal direction computations or rapid movement computations for 5-axis paths, or how 3d scanning results are to be understood.

- *Internal volume mask:* By creating volumes bound by the holes (i.e. the red contours), a set of internal volumes which mask the model surface where the surface normal direction would intersect the model, as shown in Figure 6.11a. i.e. The internal volume mask covers up areas where a multi-axis deposition system would not have nominal access for repair or a 3D scanning system would be unlikely to get a good surface measurement. Alternatively, this volume could be used for support calculation to make a non-printable object printable. Since a CNC mill does not need to always been orthogonal to the surface it is machining, milling can be used to remove the additional support material in many cases.

- *Clearance volume:* By computing volumes bound by the convex hull of the solid edges (i.e. the blue contours) a clearance volume can be created. This shape, shown in Figure 6.11b, defines a surface a milling tool or deposition head can travel on, with an orthogonal tool axis, and never collide with the part. In practical terms, this indicates to the path planning system when a detailed collision check is necessary. If the tool is on or outside the clearance volume, the orientation has "cleared" the collision check, hence the name.
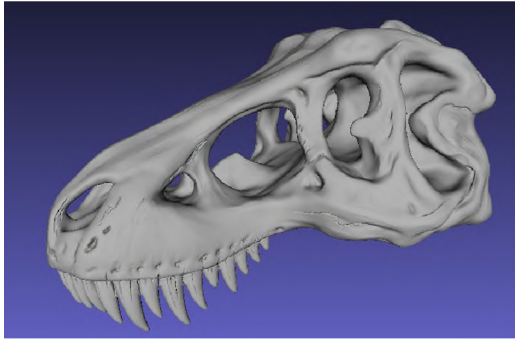
(a) A tyrannosaur skull - a topologically complex CAD model used as an example for the computations in this section.
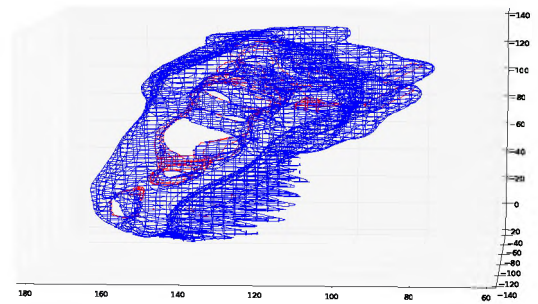
(b) The skull from Figure 6.10a sliced in 3 mutually orthogonal directions. Blue contours indicate solid edges while Red contours indicate hole edges.

Figure 6.10. CAD model and slices of a tyrannosaur skull used for the topological inspection discussion (Model courtesy of MakerBot via Thingiverse).
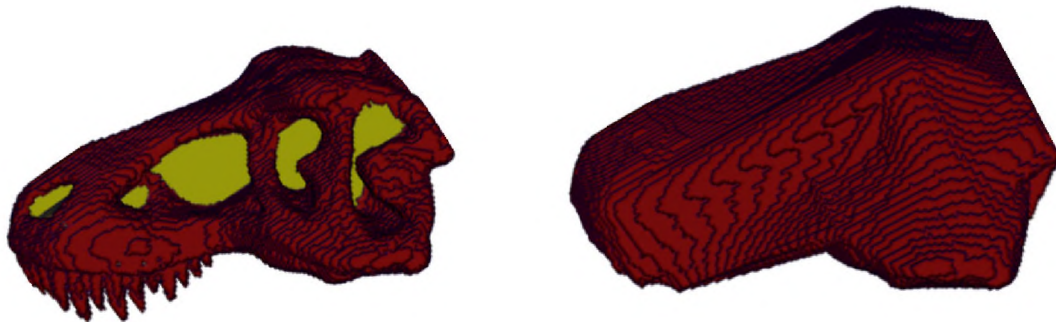
(a) Internal volume mask computation

(b) Clearance volume computation

Figure 6.11. Example topological computations using data from the slices shown in Figure 6.10b.

6.5. GEOMETRY FACTORS

The objective of the geometry factors computation is to account for global shape effects on the fatigue life. The intent is to capture some of the classical concerns for fatigue life, such as the stress concentration factor from sharp internal corners. For tessellated mesh geometry, this can be simply considered as a measure of the per-edge dihedral angles, as seen in Figure 6.12a.

38

The importance of a piece of locational information, such as the dihedral angle measurements or path effects measurements discussed in Section 8.1, in the context of the present fatigue tool can be informed by examining the position relative to the surface and/or volume of the part. This is accomplished through the use of a truncated signed distance function (TSDF) computed over a voxel representation of the object. An example TSDF for a tyrannosaurus rex skull is shown in Figure 6.12b. The TSDF computation results in a 3D field of data where an iso-value surface drawn at a value of 0 would re-create the original geometry. Negative values are interior to the shape (e.g. increasingly orange in the figure), giving us a mechanism to evaluate the severity of a potential defect site by its distance to the surface. Alternatively, the TSDF can be used to assess the cost of a sharp angle by how "heavy" the section that feature resides near. The positive values in the TSDF result (not pictured in Figure 6.12b) represent distance from the model's surface. Applications using the positive side of the TSDF include the routing of support pillars and computation of collision-free rapid motion paths for machining.
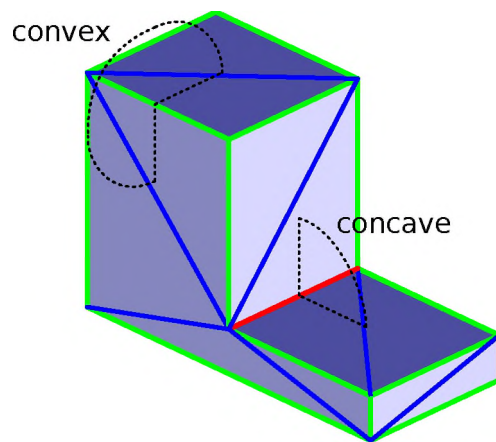
(a) Per-edge dihedral angle computation - The green edges are convex edges. The blue edges are flat. The red edge is a concave edge.
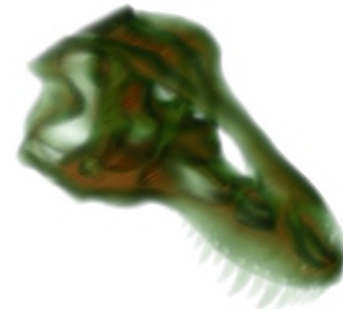
(b) Truncated Signed Distance Function (TSDF) of a tyrannosaurus rex skull. The colors scale represents distance to the nearest surface, where green tones are near surface and the orange tones are more interior.

Figure 6.12. Example global geometry computations which are useful for fatigue performance estimation.

6.6. SUPPORT GENERATION

The loft tool allows for the wholesale creation of support structures from geometric and numerical model data, such as the trees seen in Figure 6.14a as well as the connections to a gyroid infill as seen in Figure 6.14b. These structures have been printed on Missouri S&T's Renishaw AM250. As you can see in Figure 6.14c, these builds were all successful in that they completed without causing the build to fail or affecting their neighbors. This is attributed to the fact that we understand the basic requirements for support generation from the Phase I experiences, especially for such a simple geometry. The question at hand here is how the different support styles affect residual stresses and ease of removal.
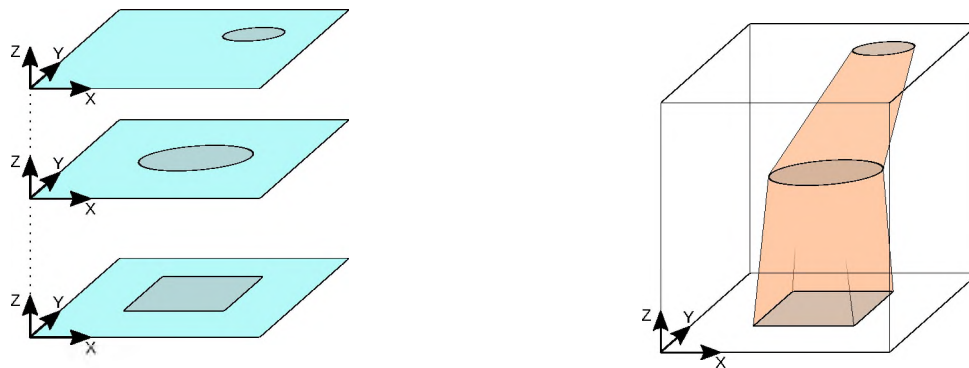
(a) Three 2D guide curves on individual planes sitting in 3D space.

(b) The resultant 3D object from the given guide curves.

Figure 6.13. The 3D lofted object is constructed by computing intermediary shapes between guide curves, drawing the curves into a 2D pixel data object, then converting the stack of 2D pixel data objects into a 3D voxel object.

The direct mesh method for creating supports uses the same support route data as the loft method discussed in Section 6.6 to create arbitrary polygonal cross section pin support. As seen in Figure 6.15, the support route defines a path from a support point where contact

(a) Support trees constructed by the union of multiple loft structures.

(b) Hybrid support structure using lofts to connect to a gyroid infill.

(c) Test builds of the loft supports.
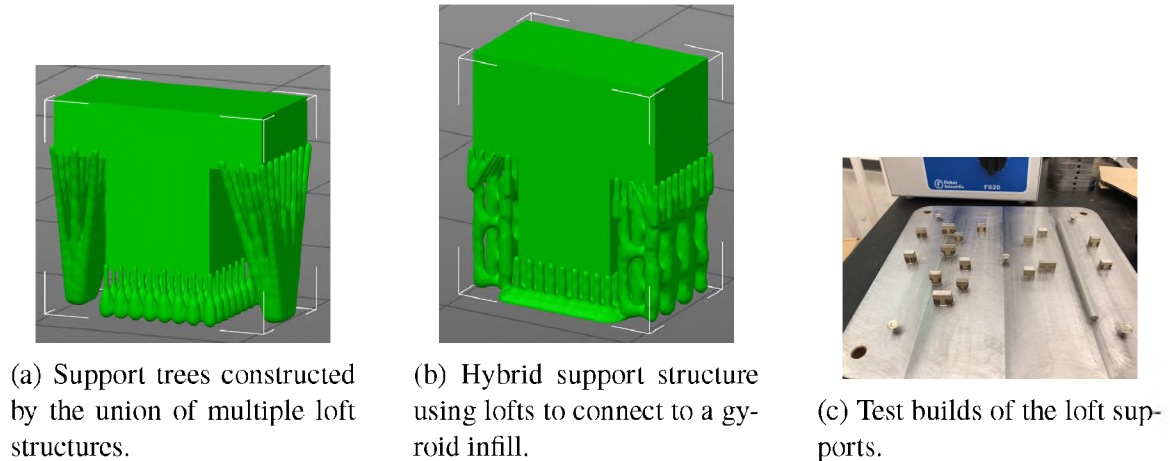
Figure 6.14. Application of the loft construction concept to support generation.

is made with the component to a base contact point, which is nominally on the build plate but may also be on the part itself in cases where the support could not be routed to the plate by the rules given to the support routing algorithm. Sample output from the direct mesh creation utility can be seen in Figure 6.16. The direct mesh support creation algorithm can be summarized as:

1. At each control point along the support path seen in Figure 6.15a, a polygon is inscribed in a circle. The radius of this circle is defined by the machine/material profile while the number of sides of the polygon is a user preference. The circle radius generally should taper towards the contact point with the part. The precise dimension of the circle can by modified by inferring support strength requirements from field data.

2. Facets are stitched together by creating 2 triangles per consecutive polygon side, as seen in Figure 6.15b. Care is taken to ensure the right hand rule is followed to ensure the winding number of the facet is strictly 1. This ensures that the correct side of the facet is "out".

3. The top and bottom polygons are closed with facets sharing a central point. As seen in Figure 6.15c, the position of the central point can be extended along the last support route direction by a configurable amount in order to ensure contact with the supported component.

(a) Support route and sizing specification.

(b) Facet creation for the sides.

(c) The contact point facets are modifed by an *ingress* value at the center point.

(d) The completed sample pin support.
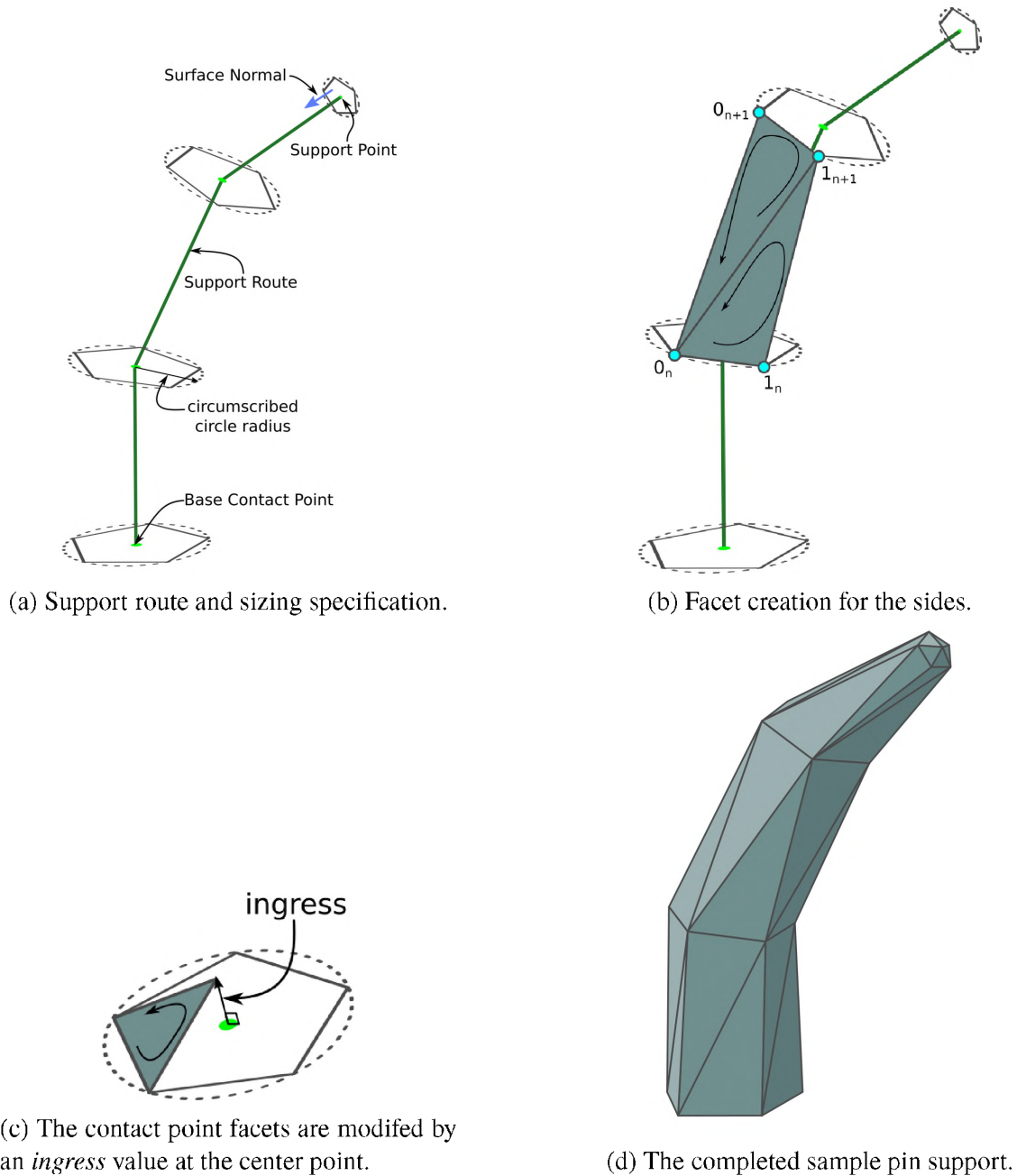
Figure 6.15. Direct mesh pin support creation process.
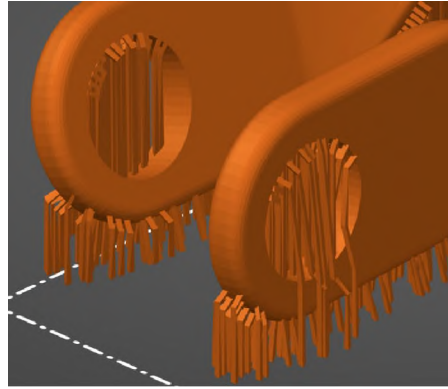
(a) Yoke.
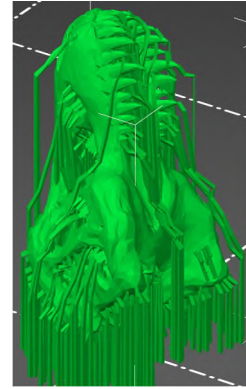
(b) Tyrannosaurus rex skull.

Figure 6.16. Adaptive route, direct mesh pin supports with a triangular cross section.

7. ROBUST CAM FOR ADDITIVE MANUFACTURING

The planning suite is a python-based, modular, flexible set of planning utilities that can be reconfigured for various deposition tasks. Sections 7.1-7.1.3 outline the functionality of the major subcomponents of the process planning suite. Sections 7.2-7.4 discuss three use cases of the suite.

7.1. PROCESS PLANNER

The process planning module is the main, user-facing utility of the suite. It is responsible for interpreting user intent, importing and exporting model data, as well as managing the input to and output from the other three modules.

The process planning module is composed of several sub-components, as described in figure 7.1. The model preprocessor converts input model data into a more efficient internal format (STL data files are notoriously bloated storage formats) before passing the data on to the model data manager. The process data manager takes the process information from the input data, then iteratively queries the model data manager for the requisite information to complete the task. The model data manager handle's requests for slices (from the slicing engine) and 2d paths (from the pattern engine). The model data manager also requests any best-fit analyses or creation of secondary models, such as the clearance volume discussed later in Section 6.4. Finally, the process planner sequences the paths received from the pattern engine and sends the completed additive paths to the post processor.

7.1.1. Slicing Engine. The slicing engine performs the mathematical operations, inspections, and book keeping needed to create 2D slices of 3D models. First, it intersects the slicing plane with every triangle in the input model. This returns a set of unorganized line segments. Next, the line segments are sorted into closed loop contours. Finally, the

contours are inspected to determine if they describe solid edges or hole edges. Solid edges surround a solid object, while hole edges describe holes within solid objects. A sample sliced object is shown below in Figure 7.2.
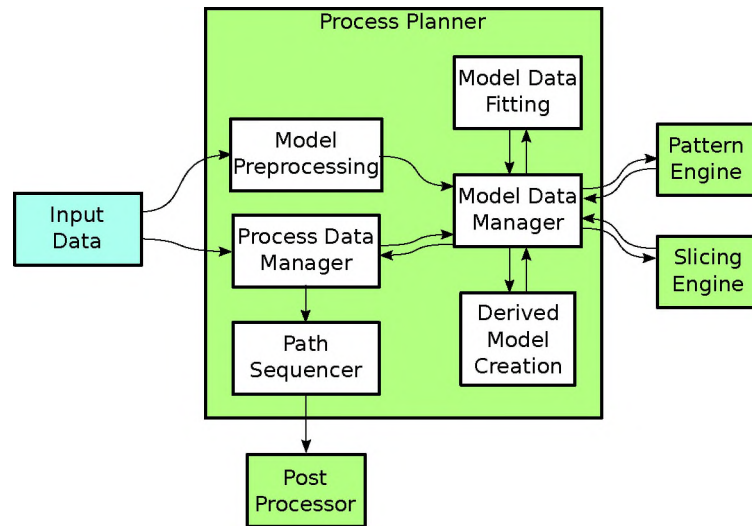
Figure 7.1. Data flow through the process planner module.
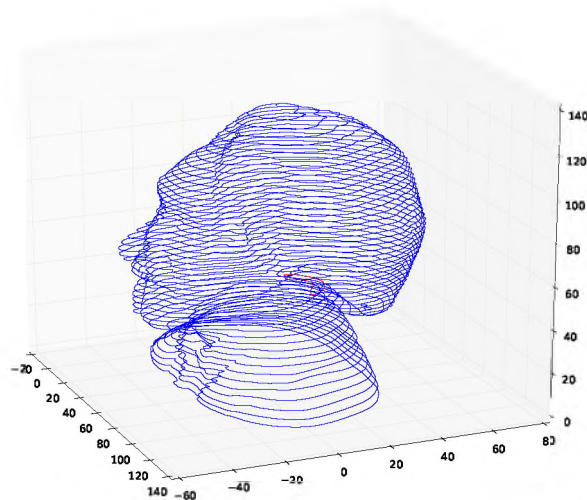
Figure 7.2. Slicing engine demonstration - a bust of Einstein. Solid edges are blue. Hole edges are red.

7.1.2. Pattern Engine. The pattern engine takes contour data and generates infill patterns. There are currently three supported patterns for additive manufacturing: raster, offset, and spiral, as illustrated in Figure 7.3. In additive manufacturing, the most likely site for a defect is at the edge of a deposited path, so it is good practice to use sets of patterns which inhibit the possibility of defect site stack up. For example, most additive manufacturing path planners use raster pattern infill with alternating raster directions to ensure no paths in consecutive layers can be in the same direction. Pattern and sequence of operation (which is handled later by the post processor, section 7.1.3) also have residual stress implications.

(a) Raster infill pattern Parameters: raster line direction, spacing.

(b) Offset infill pattern Parameters: spacing.

(c) Spiral infill pattern Parameters: pitch, orientation (i.e. clockwise or counterclockwise).
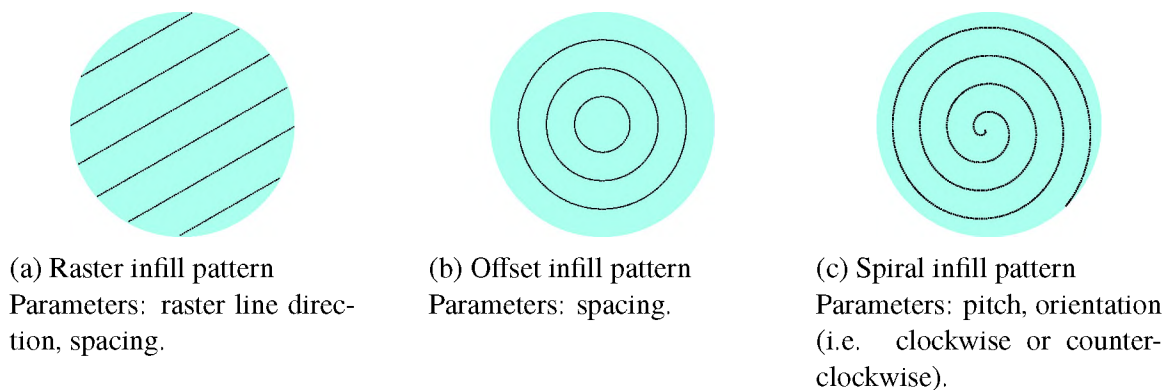
Figure 7.3. Pattern engine functionality.

An optimized figure of merit for various patterns applied to input contours is difficult to define. However, some rules of thumb can by laid out plainly:

• Sharp turns resulting in "pointy" paths often result in over-depositing due to both the dynamics (i.e. it cannot stop and accelerate instantly) of the additive machine ad the overlap of the laser.

• Paths spacing less than the desired amount will result in over-depositing.

• Paths spacing more than the desired amount will result in under-depositing.

- Paths with long non-deposition times (i.e. the total length of the dashed lines) are not efficient.

- Long, continuous deposition paths tend to work better than starting and stopping many times.

Figures 7.4 and 7.5 show all three patterns applied to two different geometries. Judging from the rules of thumb outlined above, it can be judged that the offset paths (Figures 7.4c and 7.5c) are the least desirable due to areas of both over- and under-deposition. The raster path (Figure 7.4b appears to be the best fit for the simple bracket geometry since it has the best area coverage with the fewest problems. The spiral path (Figure 7.5d) appears to be the best for the die casting core geometry due to its long, continuous deposition paths.

(a) Simple bracket geometry. (b) Raster infill pattern. (c) Offset infill pattern. (d) Spiral infill pattern.
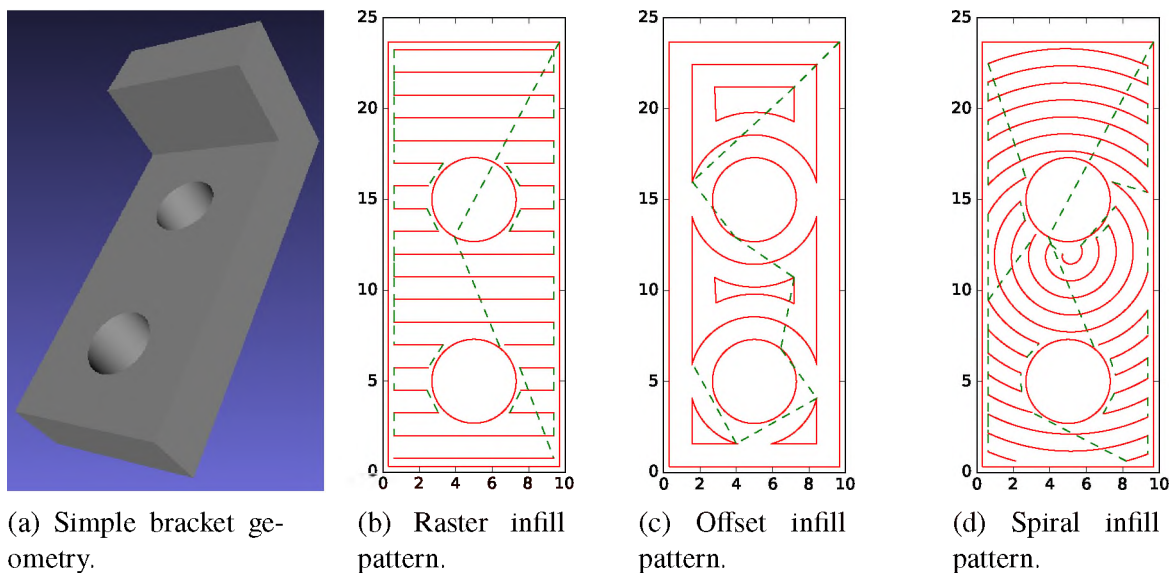
Figure 7.4. Pattern engine infill patterns applied to a slice from a simple bracket.

7.1.3. Post Processor. The post processor's primary task is to take non-machine specific process information and turn it into machine-specific instructions, generally some dialect of G-code, as illustrated in Figure 7.6. Another task left to the post processor is to connect the additive paths. The previous tools are only concerned with paths where work is being done, i.e. there are no positioning maneuvers where the machine is not
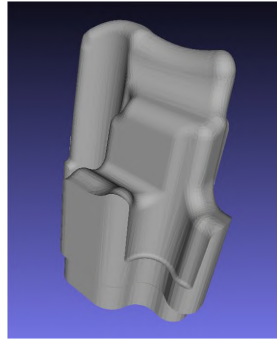
(a) High pressure die casting core.
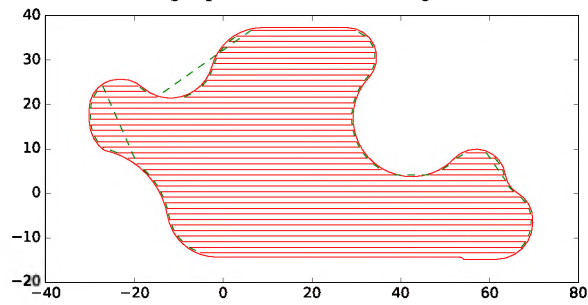
(b) Raster infill pattern.
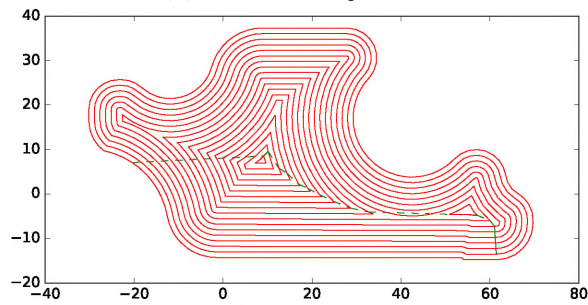
(c) Offset infill pattern.
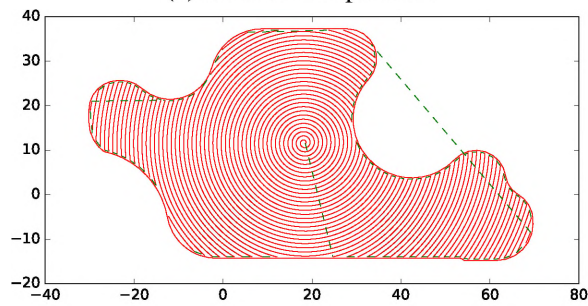
(d) Spiral infill pattern.

Figure 7.5. Pattern engine infill patterns applied to a slice from a high pressure die casting core. (Model courtesy of Toyota).

doing some sort of work. If the previous path does not end exactly where the next path begins, the post processor must calculate an appropriate connection path. Based upon the machine's restrictions, the post processor can connect paths with a simple line or create a more complex path that is tangent to both paths being connected. This smoother path is useful in reducing machine vibration in systems where that is deleterious. Lastly, if the machine settings allow it, the post processor can reverse a path if it would reduce the total distance where work is not being done.
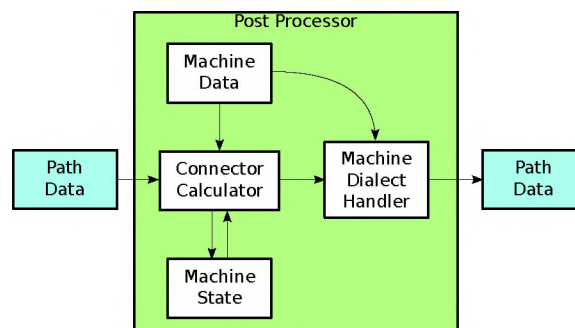
Figure 7.6. Data flow through the post processor module.

7.2. PROCESS PLANNING FOR MANUFACTURING

Process planning for the production of a component, seen in Figure 7.7, is a straight-forward process. A user (or some other upstream software tool) supplies a part geometry and a task descriptor which contains process information such as the desired layer thickness, beam spacing (i.e. the nominal distance between parallel lines in the path plan), laser power information, powder or wire feed information, etc. The process planner modules, as outlined above, then do their respective tasks, as described in Sections 7.1 through 7.1.3, to produce code which can run on an additive system to produce the printed object.

Power planning along a path is another feature that can be applied at this stage. This technique is discussed in Section 8.2
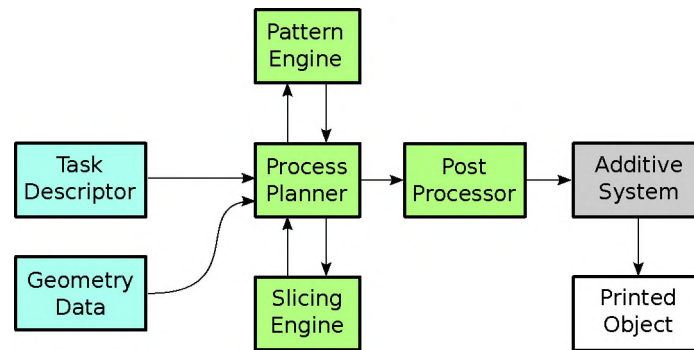
Figure 7.7. Path planning for general purpose 3D printing.

7.3. PROCESS PLANNING FOR REPAIR

Repairing a component is a more complicated case to handle than part production. General purpose automated repair path planing, outlined in Figure 7.8, differs from production in the following ways:

- Some form of reverse engineering data is required to determine which subset of the part geometry is sent to the slicing engine.

- Alignment of the physical component in the additive system should match with the coordinate system in the part's CAD data. If not, then the carefully determined repair volume(s) may not be placed correctly.

- The component may not match its CAD data well at all, even in areas that are not considered a defect. This becomes mathematically complicated to determine what the damaged volume is. For some of these cases, feature-based repair, outlined below in Section 7.4, can be applicable. When feature based repair cannot work, however, we are stuck with volumetric RANSAC fits such as the one described in Section 5.1.2
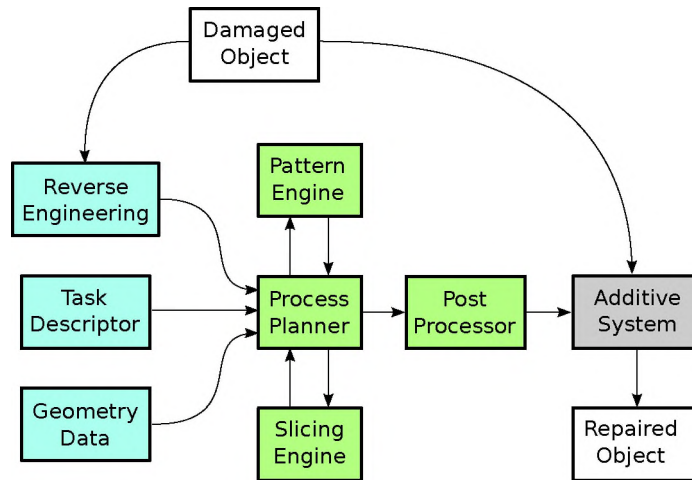
Figure 7.8. Data flow for an automated repair process.

7.4. FEATURE-BASED REPAIR PLANNING

The feature-based repair planning paradigm describes a repair job as a set of well-defined, discrete activities. In a feature-based repair process, as seen in Figure 7.9, these activity definitions then translate into paths, which in turn translate into machine-specific code.
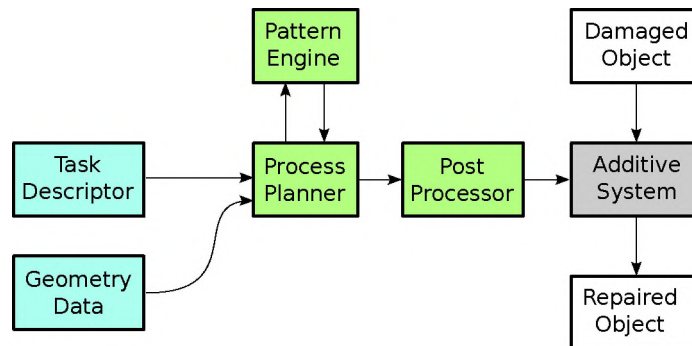
Figure 7.9. Data flow for a feature-based repair process.

Filling on a surface as shown in Section 5.1.2 is a good example of one type of repair feature. Any mathematically describable surface (e.g. planar, cylindrical, conical, spherical, or even spline surfaces) is a valid target for a RANSAC based fitting approach to do this kind of Feature based repair. By working from reverse engineering data, this type

of repair does not need a CAD model, nor would it be troubled by real-world tolerances w.r.t. CAD data. The only real limitation to a RANSAC surface fitting approach for a repair feature is the need to have enough data of the known good surface to match to. For example, the fit seen in Figure 5.6 was accomplished with approximately 40% of the data points belonging to the damaged section.

A second type of feature-based repair activity is a procedure based repair. This can be though of as an analog to the conversational features on modern CNC milling machines. For these types of features, the repair geometry needs to be expressed in a few simple parameters. This class of repair could include:

- Repair the rim of a hole given an axis, diameter, and location, such as in the example shown in Figure 7.10.

- Clad a shaft given an axis, start plane, end plane, start radius, and end radius.

- Infill a polygon given a set of points defining the boundary.
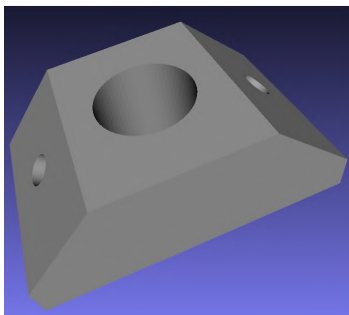
(a) Sample part with holes to be repaired.
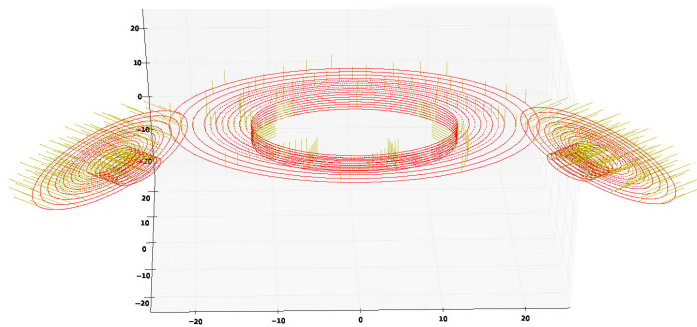
(b) Procedurally generated offset tool path with laser approach directions for 5 axis repair.

Figure 7.10. Hole rim feature based repair example.

7.5. INSPECTION-BASED CAM

The initial probe input for the region of interest (ROI) for a repair activity is conducted by a machine operator using an on-machine probe system. A CNC macro can communicate with a PC via TCP packets. This allows the probing cycle to report the measured point to the control PC. Using a simple planar polygonal region as an exmaple, the ROI selection work flow proceeds as such:

1. (optional) The operator can make the probing process a little easier by first marking out the ROI with a marker.

2. The operator initiates ROI point data collection on the controller.

3. Following the on-screen instructions, the operator sequentially probes points around the perimeter of the ROI in a counterclockwise fashion using a provided probe macro.

4. The controller performs two tests on the collected points for validity:

   - Compute the winding number about the centroid of the shape described by the probe points. If the winding number is precisely 1, such as shown in Figure 7.11a, the polygon is ordered correctly. If the number is -1, then the points were probed in a clockwise fashion, such as shown in Figure 7.11b. This can be corrected by reversing the order of the points. If this winding number is any value other than +/-1, it would indicate loops in the polygon, thus then the operator intent is unclear and the data collection should be redone.

   - If there are any self-intersections in the polygon, such as the one shown Figure 7.11c, the points as ordered do not form a valid shape. A valid shape can be recovered by computing the convex hull of the input points, but this does not necessarily preserve the operator's intent. The safe choice in this case is to require the data collection to be repeated.

5. The controller displays the validated ROI shape for the operator to confirm.

6. After confirmation, the ROI is passed onto the path planner for the creation of a detailed inspection plan.

(a) Probing of 4 points in a counter-clockwise fashion, resuling in a correctly oriented polygon.

(b) Probing of 4 points in a clockwise fashion, resuling in a incorrectly oriented polygon. Failing to catch this error would result in algorithms down the line thinking the polygon is facing down.

(c) Incorrect probing of 4 points resulting in a self-intersecting shape (red edges). A valid shape can be recovered by using a convex hull operation (red lines).

Figure 7.11. Inspection-based CAM probing procedures.

7.5.1. A Cost-Effective Inspection Tool. The measurement tool has been prototyped, as seen below in Figure 7.12a. The sensor used in the measurement tool, a Wengler OPT2001, produces an analog voltage proportional to the distance from a fixed point beneath the sensor. The measurement axis of the sensor is aligned with the spindle axis. When using the sensor to measure a point in 3d space, the value can be computed as $[X_{CNC}, Y_{CNC}, Z_{CNC} + V_{sensor}scale + offset]$, where V_{sensor} is the sensor voltage, $scale$ is the scale factor to convert voltage to mm, and $offset$ is the linear offset to the tool length offset position, as described in Figure 7.12b.

Two implementations of this sensor system were explored during this activity. The first implementation, discussed in Section 7.5.2, used a separate device (an Arduino UNO) to read the sensor value which was later combined on a PC with the reported position of the CNC machine to create a measured point in the machined workspace. This was abandoned for the method described in Section 7.5.2 which uses a calibration procedure to
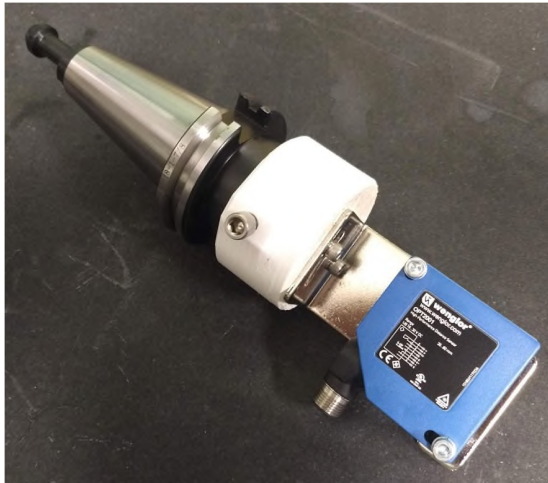
(a) Prototype of the measurement tool for repair inspection
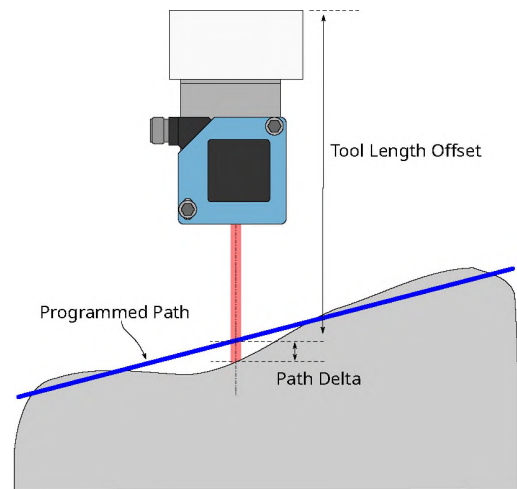
(b) The measurement tool measures the differential from a defined path along the tool axis.

Figure 7.12. Prototyping and testing of the measurement tool.

seed constants into the CNC machine's memory which allow for the computation of precise measured positions on-machine, essentially turning the CNC machine into a rudimentary non-contact 3D scanner.

7.5.2. Externally Calibrated Scanning. As we have previously reported, a Wengler OPT2001 laser distance sensor is used in this project for inspection of parts to feed data to the path generation process. The OPT2001 is currently wired directly into one the Haas NGC control's analog inputs. This allows the O88011 single point measurement macro, previously reported and seen again in Listing 7.1 for clarity's sake, to directly compute the position the measurement laser intersects a surface in 3D space within the current work coordinate system by using slope and offset calibration values stored in the Haas NGC memory and report that position back to the control PC over the DPRNT interface. The O88013 macro, seen in Listing 7.3, is used to specify a rectangular grid of measurement points. Finally, the O88012 macro is used to send a simple message to the control PC over DPRNT to indicate that point collection is complete.

Listing 7.1. O88011.nc - Single point measurement macro

```
 1  %
 2  (macro  for  laser  probe  measurement)
 3  G103  P1  (lookahead  to  0)
 4  G4P50
 5  #10824=0.2*[#5043 -#13022*#10825/100000+#10826]
 6  G4P10
 7  #10824=#10824+0.2*[#5043 -#13022*#10825/100000+#10826]
 8  G4P10
 9  #10824=#10824+0.2*[#5043 -#13022*#10825/100000+#10826]
10  G4P10
11  #10824=#10824+0.2*[#5043 -#13022*#10825/100000+#10826]
12  G4P10
13  #10824=#10824+0.2*[#5043 -#13022*#10825/100000+#10826]
14
15  DPRNT[#5041[44],#5042[44],#10824[44]]
16  G103
17  M99
18  %
```

Listing 7.2. O88012.nc - Macro for telling the control PC to end measurement recording

```
1  %
2  (macro  for  laser  probe  measurement  end)
3  DPRNT[D]
4  M99
5  %
```

Listing 7.3. O88013.nc - Measurement macro for a rectangular grid

```
1  %

2  ( Patch scan program )

3  (    Syntax: G65 P88013 X<x count> Y<y count> Q<increment>
      )

4

5  ( set up counter variables)

6  #10827=0 (X)

7  #10828=0 (Y)

8

9  G91

10 N1 WHILE [#10828 LT #25] DO1

11 G65 P88011 (SCAN FIRST POINT)

12 N2 WHILE [#10827 LT #24] DO2

13 G1 X[#17]

14 G65 P88011 (SCAN EACH POINT ALONG X)

15 #10827=[#10827+1]

16 END2

17 #10827=0

18 G1 X[−#17*#24]Y[#17]

19 #10828=[#10828+1]

20 END1

21 G65 P88012

22 G90

23 M99

24 %
```

7.5.3. Internally Calibrated Scanning. An improvement has been made to the inspection subsystem of the project. In the previously reported implementation, the analog signal from the Wengler OPT2001 displacement sensor was read using a 0-5V 10-bit analog to digital converter (ADC) aboard an Arduino UNO. The Arduino would then report the measurement to the control PC over a USB connection. During investigations into the Haas Next Generation Control (NGC), several direct analog inputs were discovered. These inputs are accessible as variables within g-code on the Haas. While undocumented, experimentation indicated the inputs are 0-5V, 12-bit ADCs. This presented an opportunity to use the laser displacement sensor directly from within the Haas NGC, making the measurement data available within the controller itself. This ability would improve the utility of the sensor by making the tool accessible to general operation of the machine rather than purely an accessory for repair system.

To use the Wengler OPT2001, a calibration must be established to relate the integer values acquired from the ADC on the Haas NGC to actual measurements. The process proceeds like this:

1. The measurement tool is placed into the CNC spindle.

2. Position the tool above a reference surface.

3. Record the spindle to surface distance as the tool length offset for tool 51, the measurement tool.

4. On the control PC, execute the python script 'calibrate.py', seen in Listing 7.4. The python script will listen for measurements from the CNC machine, compute the slope and intercept values for the calibration, and then populate them into the CNC machine's variable memory for later use.

Listing 7.4. calibrate.py

```
1  from HaasPy.haasCom import *
```

```python
import sys
import numpy
a=haas()
a.ip="192.168.0.3"
if a.start():

        print("start calibrate.nc on the CNC")
        data=[]
        for i in range(15):
            data.append(a.dprntListen())
            print("measurement {:}".format(len(data)
                ))

        points=[]
        for line in data:
            split=line.split(",")
            points.append([float(split[0]),float(
                split[1])])

        points=numpy.array(points)
        fit=numpy.polyfit(points[:,1],points[:,0],1)
        a.setVariables({a.variables["displacement sensor
             scale"]:fit[0]*100000,a.variables["
            displacement sensor offset"]:fit[1]})
        print(a.getVariables([a.variables["displacement
            sensor scale"],a.variables["displacement
            sensor offset"]]))
```

5. Execute 'calibrate.nc', seen in Listing 7.5, on the CNC machine. This script will take sets of 5 measurements positions +0.5in, +0.0in, and -0.5in from the reference surface. These measurements are sent to the control PC via the DPRNT interface. calibrate.nc:

Listing 7.5. calibrate.nc

```
1   %
2   G54
3   H51 G43
4   G90
5   G103P1
6   G1Z0.5F10.0
7   G4P50
8   DPRNT[0.5,#13022[44]]
9   G4P10
10  DPRNT[0.5,#13022[44]]
11  G4P10
12  DPRNT[0.5,#13022[44]]
13  G4P10
14  DPRNT[0.5,#13022[44]]
15  G4P10
16  DPRNT[0.5,#13022[44]]
17  G4P10
18  G1Z0.0
19  G4P50
20  DPRNT[0,#13022[44]]
21  G4P10
22  DPRNT[0,#13022[44]]
```

```
23   G4P10

24   DPRNT[0,#13022[44]]

25   G4P10

26   DPRNT[0,#13022[44]]

27   G4P10

28   DPRNT[0,#13022[44]]

29   G4P10

30   G1Z-0.5

31   G4P50

32   DPRNT[-0.5,#13022[44]]

33   G4P10

34   DPRNT[-0.5,#13022[44]]

35   G4P10

36   DPRNT[-0.5,#13022[44]]

37   G4P10

38   DPRNT[-0.5,#13022[44]]

39   G4P10

40   DPRNT[-0.5,#13022[44]]

41   G4P10

42   G103

43   M30

44   %
```

Now that the probe is calibrated, measurements can be taken for points in the current fixture coordinate system using the O88011 macro, seein in Listing 7.1. The macro can be called using the G65 macro call code, G65P88011, within a gcode program. The macro call averages several measurements for stability, computes the Z values of the measured point in the current fixture offset, then reports the X, Y, and Z coordinates of the measurement

point over the DPRNT for an external application to use (e.g. repair inspection). However, since this information is stored in Haas NGC variables, it is also available to other external applications via the machine data collection (MDC) interface or for later usage within the same gcode as it was called.

7.6. ADDITIVE CAM STRESS IMPLICATIONS

Infill patterns can greatly affect the residual stress and deformation in the finished component [45]. Residual stresses can be classified into 3 types by a characteristic length, l_o over which the stresses equilibrate:

• *Type I* stresses are long range stresses affecting the macroscopic dimensions of a part, $l_{o,I} \approx$ the structure's scale;

• *Type II* stresses effect the region of small number of grains, $l_{o,II} \approx 3 - 10$ grain sizes;

• *Type III* stresses are microscopic stresses working over atomic scales within a grain, $l_{o,II} < 1$ grain size [46].

Dividing the layers into smaller pieces and infilling each with a random raster direction has been shown to reduce deformation [7]. Both build rate and thermal history can be optimized by modifying scan patterns [27]. Hatch length is slightly negatively correlated with shrinkage in-plane (Figures 7.13a-7.13b) and highly positively correlated with shrinkage out of plane (Figure 7.13c) [34]. In cladding, using a thicker layer can help to reduce residual stresses or even introduce beneficial compressive stresses [31]. However, this technique may not be applicable to powder bed processing due relatively low laser power of those systems w.r.t. cladding setups.

To leverage the knowledge of the phenomena discussed above in the 2d path planning for the infill of arbitrary shapes, a shape decomposition algorithm was implemented in path planning system. The decomposition algorithm, based on raster data representation of
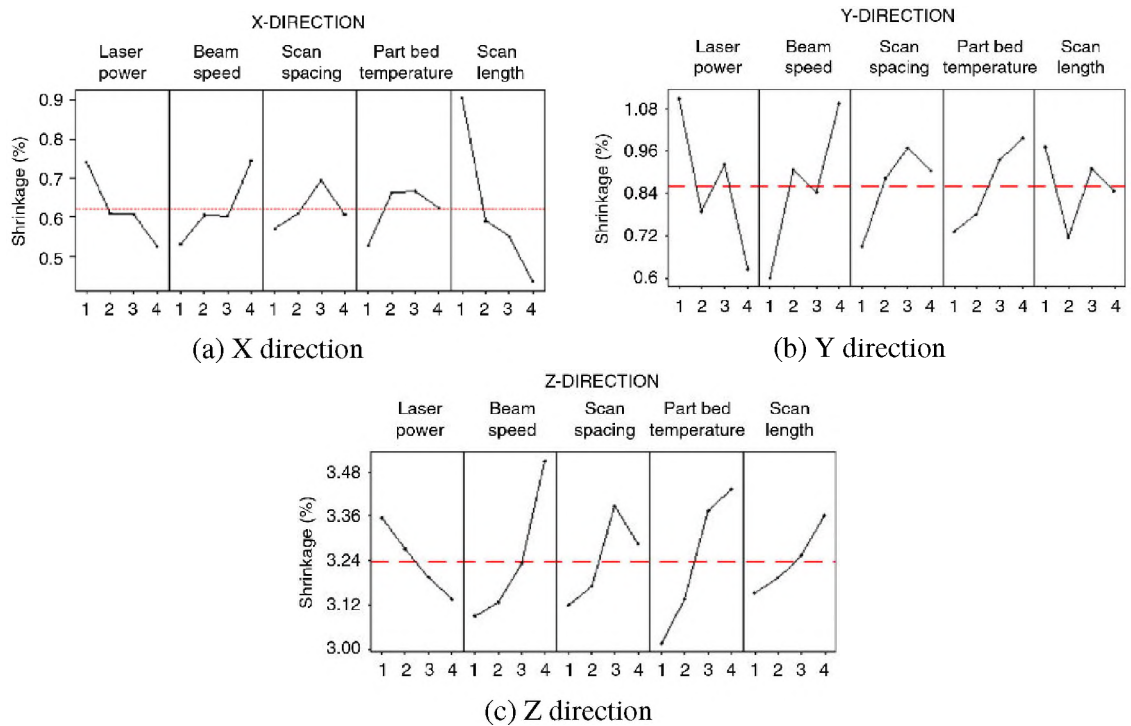
Figure 7.13. Effect of process parameters on shrinkage by direction [34].

the shape, is designed to reduce an arbitrary shape into a set of strictly convex polygons. Regions to be removed from the shape are grown from a seed position. Seed positions can be selected from any edge, any convex edge, or from an interior position at a maximal distance from an edge. The seed is then grown by iteratively dilating and intersecting with the original shape until a stop condition is reached. Stop conditions include the accumulation of a maximum desired per-region area or if proceeding to the next growth step would result in the region being no longer strictly convex. After the stop condition is reached, the newly grown polygonal region is removed from the original shape and the process begins again, proceeding until the original shape is consumed in the process. Figure 7.14 contains an example where this algorithm is applied to a polygon with a concave feature before the individual regions were infilled by a an adaptive spiral toolpath. Using this type of algorithm, we can manage the mean line length of the tool path. Also, sequencing of the regions used to build up the desired shape will also be an important factor.
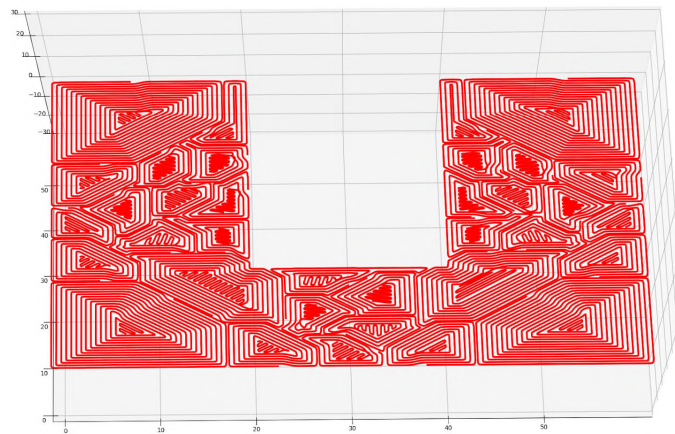
Figure 7.14. Spiral infill of a decomposed shape.

8. META-CAM ANALYSIS, PREDICTION, AND FEEDBACK

8.1. DEFECT DENSITY ESTIMATION FOR FATIGUE LIFE CONSIDERATIONS

Path and slicing strategies are conventionally considered to be important for determining the resulting properties of components produced via AM methods. This is doubly important in metal AM due to the importance of the thermal history on the final part properties. Specimens produced in the same build with the same parameters can have significantly different fatigue performance [18]. Fatigue performance can be improved by altering the scan strategy to avoid near-surface porosity [24, 40, 43].

8.1.1. Voxel-based Defect Probability Mapping. Fatigue performance can be improved by altering the scan strategy to avoid near-surface porosity [24, 40, 43]. Inter-layer and intra-layer conditions in the scan path that can contribute to defect formation, irrespective of the quality of the parameter set (e.g. laser power, scan speed, hatch spacing, layer thickness) used for the print. Here we present a model for mapping the inter-layer effects into a three dimensional field representing a probabilistic sense of where defects may occur during a part build. The intent of this activity is to provide a link between the more fundamental Murakami-type sense of how a particular defect could effect fatigue performance and the actual behavior of a full component build by helping to understand the probable locations of the defects. This defect map can also provide a tool to evaluate scan path strategies for sensitivity to fatigue performance issues. What it cannot capture, however, are any issues that will not vary based upon the scan pattern, such as a problem with the powder itself.

Fracture planes can follow defects, such as lack of fusion or porosity [1]. In the case of the commonly used Gaussian mode fiber laser use for LPBF processes, porosity defects from keyholing are more likely to occur along the path of the beam's central axis

while lack of fusion defects are more likely to occur at the outer edges of the beam where the power density is lower [9, 28]. Power density can also greatly effect the propensity of defect formation [3]. Figure 8.1 illustrates the likely location of defects with respect to a cross-section of a gaussian beam traveling along a scan path.
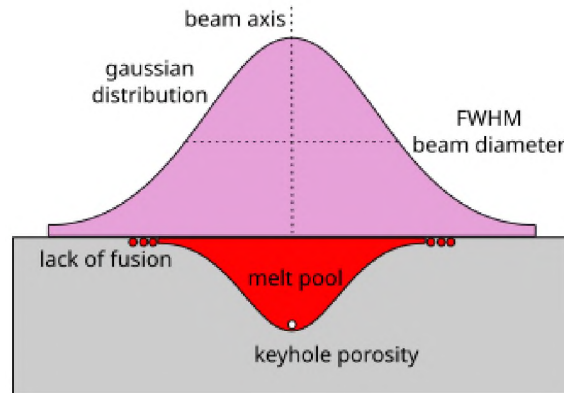
Figure 8.1. Probable defect locations with respect to the profile of a guassian beam.

To create a defect probability map for each defect type, four pieces of data are extracted from each individual scan path in the build plan, as illustrated in Figure 8.2a:

- Tracking scan start locations (blue dot) and scan end locations (red dot) will help to capture effects, if any, of starting and stopping the laser. These effects would include items such as laser power ramp rates or timing issues.

- The scan path (black curve) represents the center-line of the motion where the beam has the highest intensity, and thus the probable locations for any keyhole porosity.

- The bead edge (the green curve) is computed by the Minkowski sum of the scan path and the beam diameter. The edge is the location where the power density is the lowest and thus lack of fusion defects are more likely.

To capture the stack-up of defect sites in an inter-layer sense, the intersection of consecutive layers is computed, as seen in Figure 8.2b. The concept here is that the creation of *contiguous* defects is the most deleterious to performance. The scan path plan itself

cannot dictate the formation of individual defects, but what it can perhaps do is influence how those defects are allowed to spatially distribute themselves. Tracking areas of possible contiguous defects can allow us to evaluate a path. Creating a stack of these consecutive layer intersections creates a voxel volume representing the probable defect location sites for that particular defect type.

(a) Nomenclature of defect generating features.

(b) Intersection of defect features in successive layers.
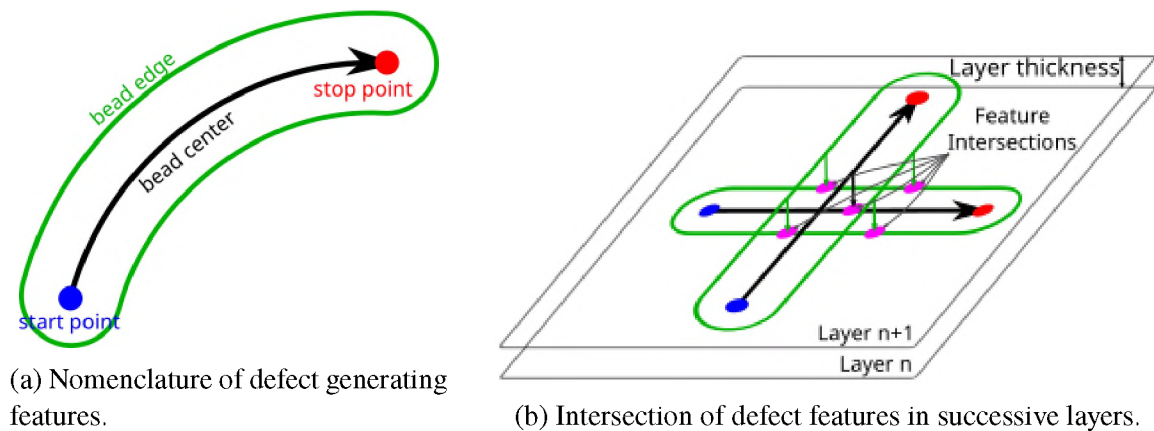
Figure 8.2. Defect map construction.

Figure 8.3a illustrates a simple example of the defect map concept applied to the keyhole porosity defects within a simple cylindrical specimen build. Note that the 90°raster rotation results in regularly spaced columns of contiguous potential defect sites. Since the contour scan for a vertically built cylindrical object is stacked directly on top of the previous one, the defect map should also indicate a contiguous shell of potential defect sites around the object. The spotty nature of the shell in Figure 8.3a is attributed to off-by-one problems from the discretization of the path data into voxel space. Accuracy issues with voxel-space computations for the defect map prompted the creation of a vector based map computation tool, which can be seen in Figure 8.3b. Further discussion on the vectors space defect mapping tool can be found in Appendix 8.1.2.
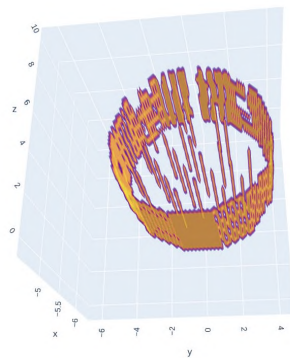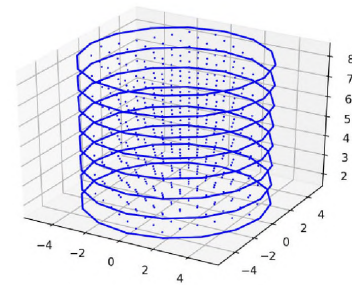
(a) Voxel space computation.   (b) Vector space computation.

Figure 8.3. Sample keyhole defect map for a cylindrical object printed with a single contour scan and 90°raster rotation infill.

The maps for each of the defect types can be superposition to generate a probability field for defects. In Equation 8.1, the defect probability map is expressed as the sum of each defect map D_i multiplied by a weighting factor W_i. The weighting factor could be a simple scalar proportion or, preferentially, another field of the same dimension as D_i that is generated from modeling data. For example, a field representing the temperature of the previous layer could be used to modify the probabilities of keyholes or lack of fusion. i.e. A higher temperature should retard the lack of fusion probability and enhance the keyholing probability. We are just beginning to explore the implications of this kind of probability map, but pairing it with a stress simulation to generate part reliability of a particular build plan via a Monte Carlo method seems like a good option.

$$P_{defect} = \sum_{i=0}^{n} D_i W_i \tag{8.1}$$

8.1.2. Vector-based Defect Probability Mapping. Figures 8.4-8.6 illustrate the computation of the interactions of path features in consecutive layers. The green lines represent the scan paths for consecutive layers while the blue lines represent the interactions of the features of interest. Path center, perimeter, and endpoint interactions are illustrated for scan path data with and without contour passes.

(a) with contours.   (b) without contours.
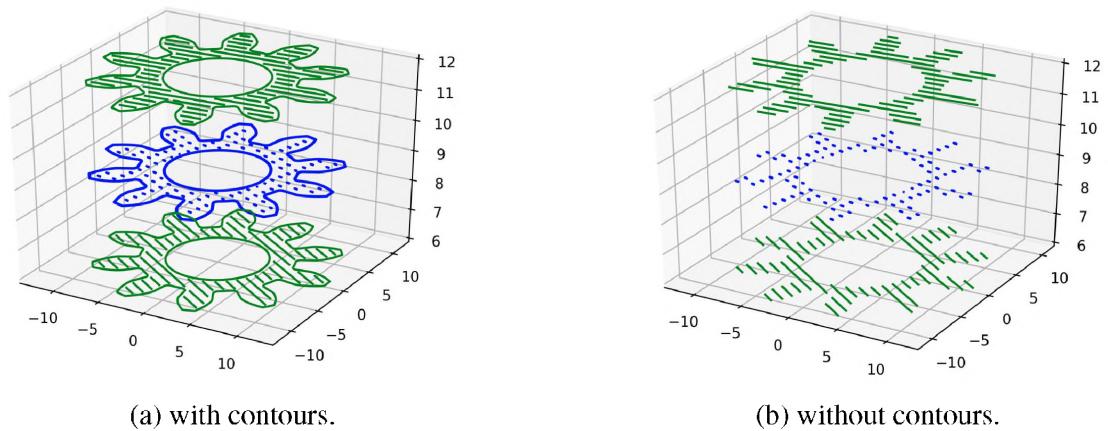
Figure 8.4. Path center interactions.

(a) with contours.   (b) without contours.
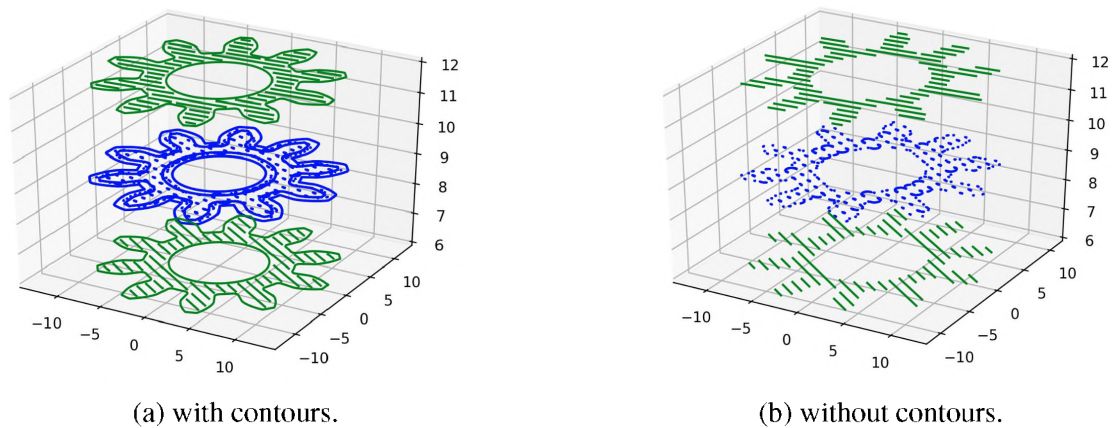
Figure 8.5. Path perimeter interactions.

| (a) with contours. | (b) without contours. |
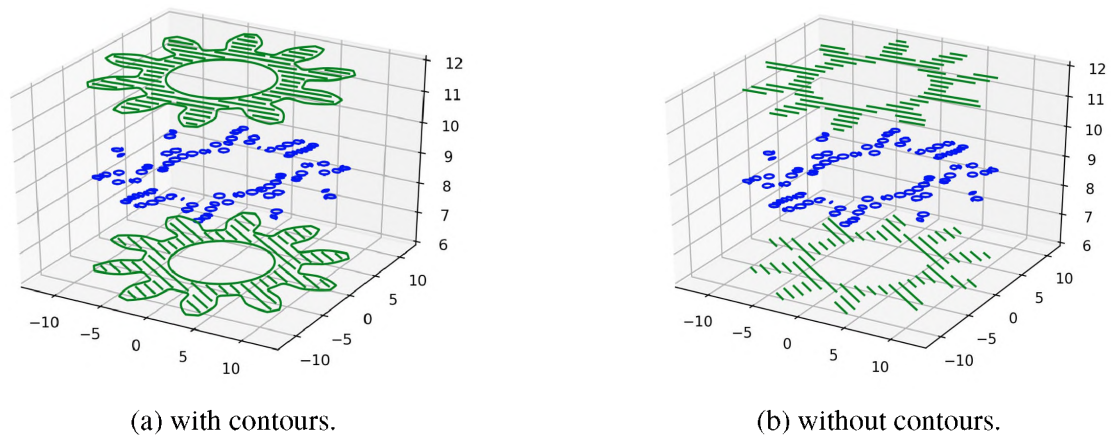
Figure 8.6. Path end interactions.

Figures 8.7 and 8.8 illustrate the observable difference in potential defect site organization made by changing the raster rotation value between consecutive layers. Note the higher degree of disorder seen in Figure 8.8b than 8.7b. This is due to the 67° raster rotation practically never reproducing the same raster axis (the least common multiple of 67 and 180 is 12060) while the 90°raster rotation produces the same axis every other layer.

8.2. PATH-BASED LASER POWER PREDICTION

LP^2 is a methodolgy for scheduling laser power along a path with the objective of creating a stable solidification rate. The issue with using a constant laser power is that the operator has to optimize the power level for a worst case scenario, typically the start of the process. This results in variations in both geometry and material properties as the melt pool size and temperature gradients vary with the local energy balance conditions around the melt pool. This is illustrated below in Figure 8.9. Feedback systems are inherently reactionary, and thus can only react to conditions that have already drifted away from nominal.

The laser power prediction method uses:

* an additive path describing the path of the laser through space
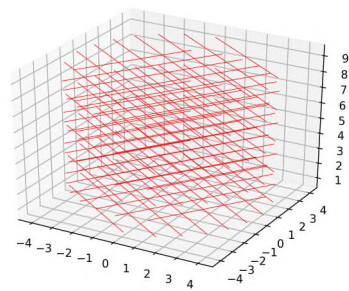
(a) Scan path.
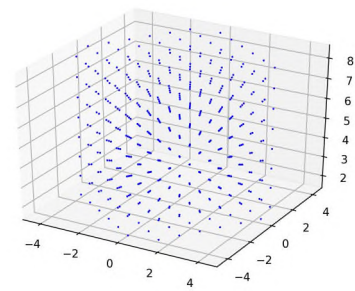
(b) Path center interactions.
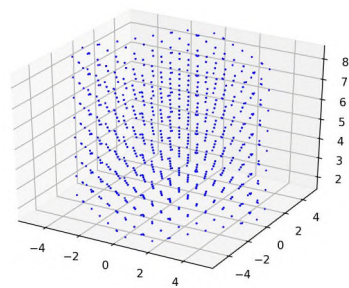
(c) Path perimeter interactions.
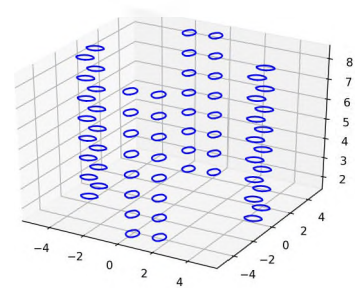
(d) Path end interactions.

Figure 8.7. Path interactions for a 90° raster infill.

- a geometric representation of the geometry that the additive path is intended to create

- a description of the thermodynamic characteristics of the manufacturing environment

- Thermophysical characteristics of the materials involved

to create a simplified thermodynamic model. This model is used to predict an appropriate input laser power at definable intervals along the laser path. It accomplishes this by using the path and geometric representation of the part being produced to create an idealized geometry that allows for tenable calculations. This idealized geometry model, shown below in Figure 8.10a, is composed of three elements: the melt pool, a hot zone around the melt pool, and the rest of the component being constructed. A key element in the LP^2 model is
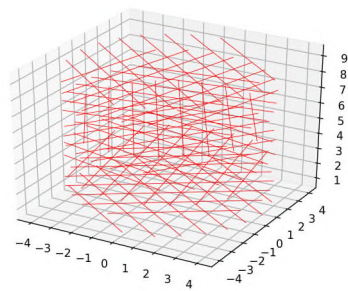
(a) Scan path.
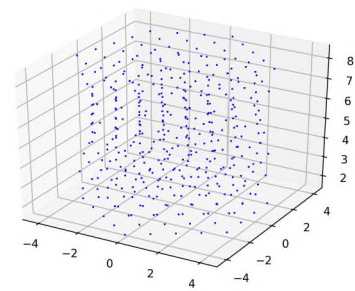
(b) Path center interactions.
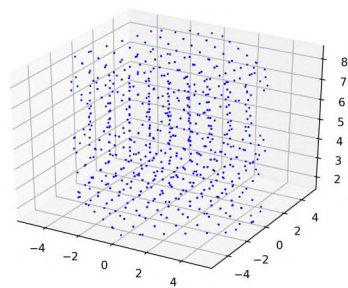
(c) Path perimeter interactions.
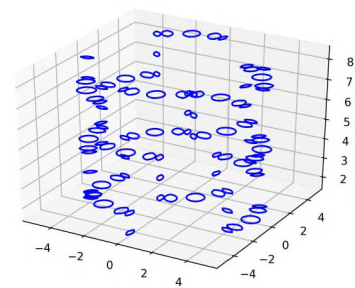
(d) Path end interactions.

Figure 8.8. Path interactions for a $67°$ raster infill.

a good estimator of the hot zone shape and connectivity to the bulk of the structure. This is accomplished by intersecting a hemisphere oriented in the direction of the tool axis with the part geometry, as shown in Figure 8.10b.

The LP^2 model's advantage over a more conventional Eulerian finite element or finite difference model can be simply visualized by noting the number of calculations (represented here as green arrows) necessary to compute the heat conduction through the domain shown in Figure 8.11. Applying domain-specific knowledge to create the simplified model for LP^2 allows for the computation of laser power with higher frequency and good numerical stability.

(a) Process start – Too little energy in the system.

(b) Mid Process – Appropriate energy is present content in the system.

(c) End of Process – Too much energy is present in the system.
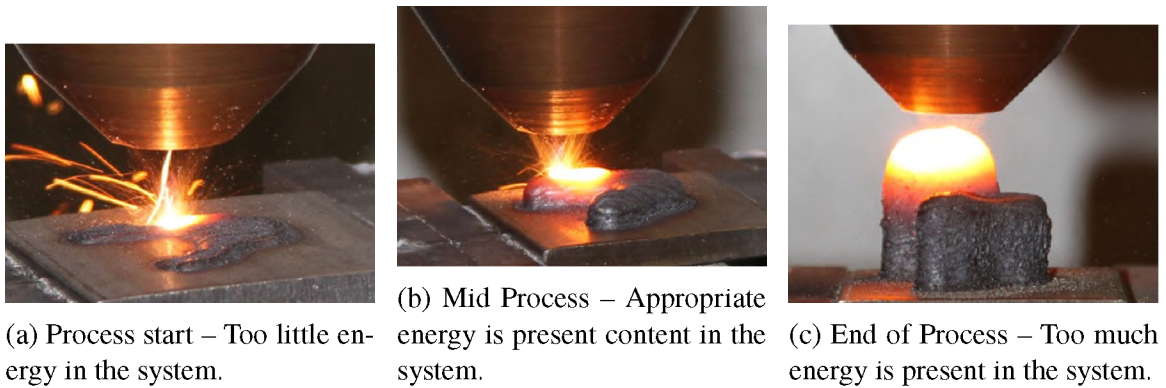
Figure 8.9. Images showing the effect of using constant laser power during an additive build process.

(a) Zones used in the LP^2 model.

(b) Sample hot zone estimations via hemisphere intersection.
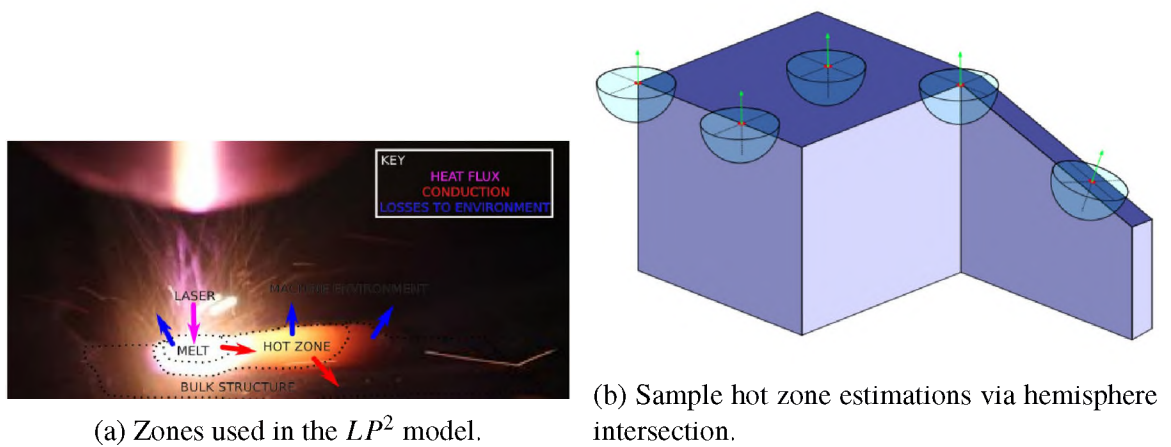
Figure 8.10. Slicing and path planning for the repaired volume.

Before describing the procedure, there is a good deal of nomenclature that must be described:

- Material properties

    – Specific heat, C_p

    – Thermal conductivity, k

    – Density, ρ

73

(a) Conventional FEM model   (b) Simplified LP^2 model
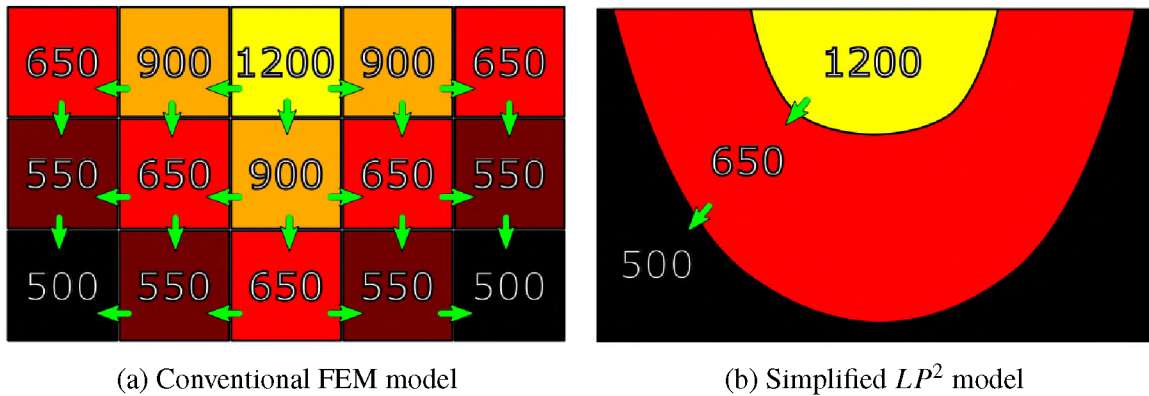
Figure 8.11. Relative calculation volume of numerical modeling techniques.

- Laser absorption coefficient, α

- Liquidus temperature, T_l

- Emissivity, ϵ

- Heat of fusion, H_f

• Machine parameters

- Maximum laser power, Q_{max}

- Abmient temperature, T_∞

- Machine temperature, T_{mach}

- Powder supply temperature, T_p

- Area for part→machine heat transfer, A_{mach}

- Convection coefficient for the machine environment, h

• Deposition parameters

- Layer thickness, d_l

- Track width, w

- Remelt thickness as a fraction of layer thickness, r

- Scan speed, f

- Substrate mass, m_{sub}

- Target superheat, T_{super}

- LP^2 process settings

  - Target hot zone radius, r_{hot}

  - Target melt pool temperature, $T_{melt} = T_L + T_{super}$

  - Target hot zone temperature, $T_{t}arget$

  - Laser power prediction interval, i_p

- Nomenclature

  - Let s describe the length along the deposition path.

  - let P describe the deposition path such that $P(s)$ is the cartesian coordinate of a point s distance along the path.

  - Let $\hat{t}(s)$ describe the tool axis direction at a distance s along the path.

  - Let G describe the deposition geometery.

  - let $Z(r, p, \hat{n})$ describe a hemisphere of radius r with the circular surface centered at point p with a normal direction of $\hat{n}$.

Prior to iterating along the additive path, initial values should be seeded into the data structures. The initial energy content of the build is expressed in Equation 8.2. The initial build mass is assumed to be the equivalent to the substrate, as expressed in Equation 8.3. The initial temperatures of the build and hot zone elements are expressed in Equations 8.4 and 8.5, respectively. Finally, the distance along the path is initialized at 0 in Equation 8.6.

$$H_{build} = C_p T_\infty M_{sub} \qquad (8.2)$$

$$m_{build} = m_{sub} \tag{8.3}$$

$$T_{build} = T_\infty \tag{8.4}$$

$$T_{hot} = T_\infty \tag{8.5}$$

$$s = 0 \tag{8.6}$$

Additionally, it is useful to pre-compute items that will remain constant throughout the computation. Equations 8.7 and 8.8 compute the maximum hot zone volume and area, respectively. The surface area of the melt pool is computed in Equation 8.9. The mass per unit length of the additive path is expressed in Equation 8.10. Finally, the time interval needed to travel one inspection interval along the additive path is computed via Equation 8.11.

$$V_{max} = \frac{2}{3} r_{hot}^3 \pi \tag{8.7}$$

$$A_{max} = 2 r_{hot}^2 \pi \tag{8.8}$$

$$A_{melt} = \frac{1}{4} w^2 \pi \tag{8.9}$$

$$m_{ul} = w d_l \rho \tag{8.10}$$

$$\delta t = \frac{i_p}{f} \tag{8.11}$$

Once the preparatory work is in place, the laser power prediction activity proceeds as follows:

1. Update V_{hot} and A_{hot} estimates for the current geometry positions using Equations 8.12 and 8.13, respectively.

$$V_{hot} = G \cap Z(r_{hot}, P(s), \hat{t}(s)) \tag{8.12}$$

$$A_{hot} = \frac{V_{hot} A_{max}}{V_{max}} \tag{8.13}$$

2. Compute rate of heat egress from the melt pool via conduction (Equation 8.14), convection (Equation 8.15), and radiation (Equation 8.16).

$$H_{cond} = \frac{kA_{hot}}{r_{hot}}(T_{melt} - T_{hot})\Delta t \qquad (8.14)$$

$$H_{conv} = hA_{melt}(T_{melt} - T_{hot})\Delta t \qquad (8.15)$$

$$H_{rad} = \epsilon\sigma A_{melt}(T_{melt}^4 - T_{hot}^4)\Delta t \qquad (8.16)$$

3. Compute an amount of energy needed to bring incoming material and remelted material up to the desired melt pool temperature.

$$H_{powder} = m_{ul}i_p((T_{melt} - T_p)C_p + H_f) \qquad (8.17)$$

$$H_{remelt} = m_{ul}i_p r((T_{melt} - T_hot)C_p + H_f) \qquad (8.18)$$

4. Sum the losses at the melt pool and the energy needed to melt material to get the total input energy required at this step. Use that to estimate a viable laser power. Note that the expression in Equation 8.20 is constrained by the output capacity of the laser system employed.

$$H_{total} = H_{remelt} + H_{powder} + H_{cond} + H_{conv} + H_{rad} \qquad (8.19)$$

$$Q_{laser} = min(Q_{max}, \frac{H_{total}}{\alpha\Delta t}) \qquad (8.20)$$

5. Update the mass of the build to include the newly deposited material.

$$m_{build} = m_{build} + m_{ul}i_p \qquad (8.21)$$

6. If accurate model data is not readily available at computation time, estimate a spherical radius and surface area via Equations 8.22 and 8.23.

$$r_{build} = \sqrt[3]{\frac{3m_{build}}{4\rho\pi}} \qquad (8.22)$$

$$A_{build} = 4r_{build}^2\pi \qquad (8.23)$$

7. Estimate significant losses to the environment from the hot zone, build, and machine. Radiation from the hot zone is computed in Equation 8.24.

$$H_{hot} = \epsilon\sigma A_{hot}(T_{hot}^4 - T_\infty^4)\Delta t \qquad (8.24)$$

$$H_{mach} = \frac{kA_{machine}}{r_{build}}(T_{build} - T_{mach})\Delta t \qquad (8.25)$$

$$H_{env} = hA_{build}(T_{build} - T_\infty)\Delta t \qquad (8.26)$$

8. Update the internal energy estimate of the build and recompute its temperature.

$$H_{build} = H_{build} + Q_{laser}\Delta t - H_{mach} - H_{hot} - H_{env} \qquad (8.27)$$

$$T_{build} = \frac{H_{build}}{C_P} \qquad (8.28)$$

9. Update the hot zone temperature estimate using Equation 8.29. The tuning parameter f is used to scale how quickly the hot zone temperature estimate scales with increasing build temperature. In practice, a value of 0.5 was sufficient to provide reasonable results.

$$T_{hot} = fT_{build} + (1 - f)T_{target} \qquad (8.29)$$

10. Update the position along the deposition path via Equation 8.30.

$$s = s + i_p \qquad (8.30)$$

Figures 8.12 and 8.13 show the results of the LP^2 algorithm applied to two simple geometries. The path specified in Figure 8.12a is a single track wall, which results in the predicted power profivle seen in Figure 8.12b. Note that the predicted laser power requirement has a periodic component superpositioned with an exponential decay component. The flat $2kW$ predicted for the first few seconds is due to the algorithm desiring more power than the laser configured for the study could output, so the output is capped. The periodic component is due to the back-and-forth motion caused by the shape of the desired geometry. The exponential decay component is a result of the part and workpiece heading towards some steady state temperature. The helical path for creating a cylinder as seen in Figure 8.13a is as close to a steady state process as metal AM will ever get. This is one of the reasons that a hollow cylindrical boss is a common demo for new metal AM systems. Figure 8.13 shows the predicted power profile for the helical path.

8.3. FEEDBACK SENSING

A new feedback sensor design has been designed with the following design criteria:

- The sensor should provide an estimator of enthalpy present in the melt pool area. (i.e. How hot is it? This is an area of high thermal gradients, so a single temperature measurement can be misleading.)

- The sensor should provide an estimator for the current melt pool location. (i.e. Is the melt pool in the correct location w.r.t. the processing head?)

- The sensor should provide a mechanism to judge the sensor alignment.
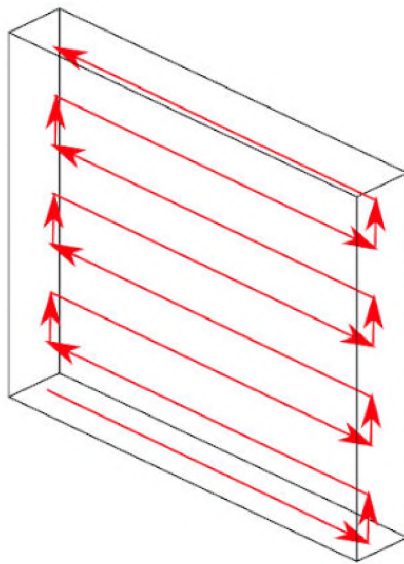
(a) Deposition path for a wall structure.   (b) Predicted laser power for a wall structure.
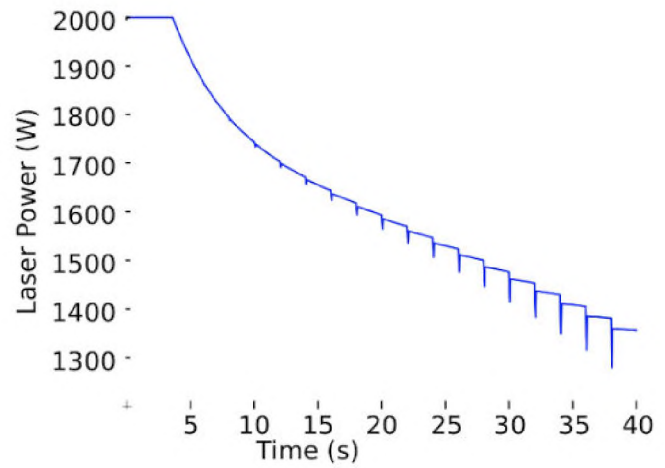
Figure 8.12. LP^2 applied to a simple thin wall deposit.
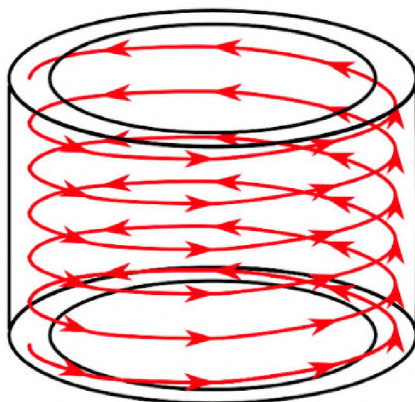
(a) Helical deposition path for a cylin-
drical structure.
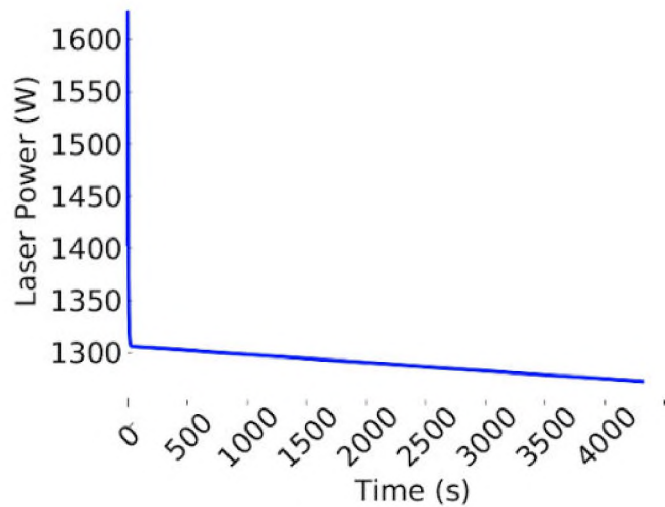
(b) Predicted laser power for a cylindrical structure.

Figure 8.13. LP^2 applied to a simple cylindrical deposit.

• The sensor should be robust vs interference from a variety of common laser wave-lengths.

A sensor meeting the above criteria has been designed, shown below in Figure 8.14a. The sensor utilizes a quadrant position detector from Thor Labs. This class of detectors is typically used for beam alignment. However, by using a lens and filter arrangement to image the melt pool and its surroundings onto the sensor's active area, as seen in Figure 8.14b, a measurement of both the melt pool size and position in image plane can be made. As the hotter (and therefore brighter) melt pool and its surroundings move off center in the image, the four quadrants of the sensor are differentially excited. The sensor returns analog signal proportional to the hot zone's position (X and Y, in the image plane) and size (SUM), as computed from the raw quadrant signals, as shown below in Equations 8.31 through 8.35.
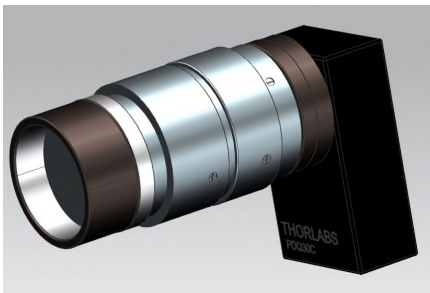
(a) A single unit of the deposition process sensor.
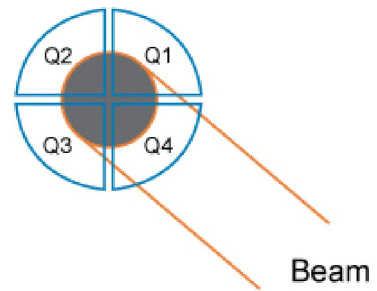
(b) Thor Labs quadrant position detector arrangement.

Figure 8.14. Deposition process sensor.

$$\Delta x = (Q2 + Q3) - (Q1 + Q4) \tag{8.31}$$

$$\Delta y = (Q1 + Q2) - (Q3 + Q4) \tag{8.32}$$

$$SUM = Q1 + Q2 + Q3 + Q4 \tag{8.33}$$

$$X = \frac{\Delta x}{SUM} \tag{8.34}$$

$$Y = \frac{\Delta y}{SUM} \tag{8.35}$$

$$TOP = \frac{\Delta y + SUM}{2} = \frac{(Q1 + Q2) - (Q3 + Q4) + Q1 + Q2 + Q3 + Q4}{2} = Q1 + Q2 \quad (8.36)$$

$$BOTTOM = \frac{SUM - \Delta y}{2} = \frac{(Q1 + Q2 + Q3 + Q4 - ((Q1 + Q2) - (Q3 + Q4))}{2} = Q3 + Q4$$
$$(8.37)$$

$$\frac{BOTTOM}{SUM} = k \quad (8.38)$$

The positional information from the X and Y signal does not translate literally to a deposit height, but instead tells us the center of brightness of the image on the sensor's image plane. This has implications on the height control application. As illustrated in Figure 8.15a, the Y signal (i.e. weighted center of the brightness), is not the same thing as measuring the deposit height. For control purposes, a better estimator for deposit height was achieved by computing the proportion of the brightness that is below the desired level, as seen in Figure 8.15b. With this setup, the perturbation in deposit height, i.e.the variation TOP value from equation 8.36, is relatively small with respect to the SUM signal. To increase the sensitivity of the control system, the BOTTOM/SUM ratio from equation 8.38 is linearly remapped to increase the change in the value given to the control system and to truncate irrational response values. This remapping can be seen in Figure 8.16.

While the power feedback is relatively robust to the accuracy of the sensor positioning, the aiming of the sensor is critical to the height control application. The height estimator, as computed in equation 8.38, approaches 1 when the entire hot area is below the line. However, if the value is exactly 1, then the system has lost the ability to resolve the deposit position. To avoid this, a setup procedure has been developed:

1. Move the deposition head into the correct position to deposit. (Henceforth referred to as Z=0mm.)

2. Turn the laser on at a low power (100W).

3. Adjust the yaw (left-right adjustment) of the sensor such that the ΔX and X converge to zero.

(a) Deposition height estimator error using the sensor's Y signal.

(b) Improved deposition height estimator using the ratio of the bottom quadrants to the total sum. Testing concluded that a k-value of approximately 0.9 provided satisfactory results.
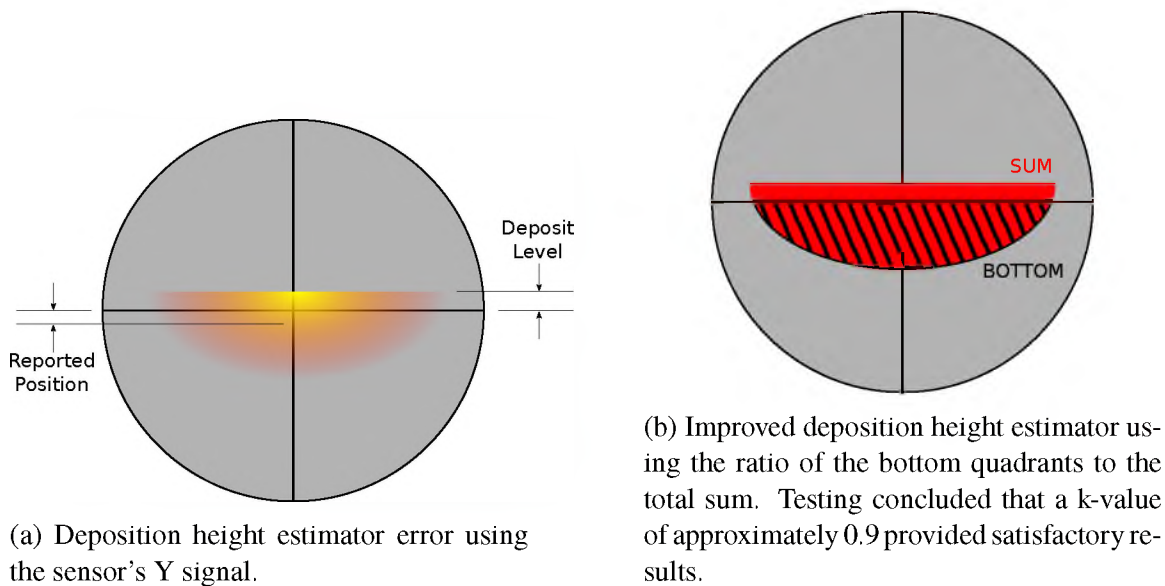
Figure 8.15. Feedback signal selection for deposit height control.
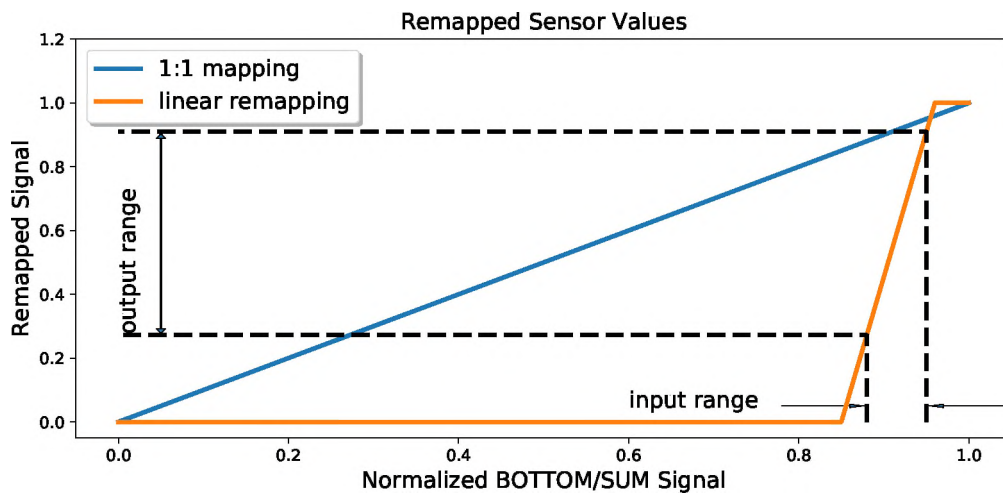
Figure 8.16. Linear remapping of the control signal for a more responsive height control system.

4. Move down towards Z=-4mm (2x the beam diameter at the working height). Adjust pitch of the sensor such that ΔY and Y converge to zero, as seen in Figure 8.17a.

5. Move back to Z=0mm.

6. Adjust the pitch of the deposition process sensor such that $\frac{BOTTOM}{SUM} = 0.9$.

7. Turn off the laser. The sensor is now aimed appropriately for feedback control.

(a) Initial state, $Z - 4mm, \Delta Y = 0, Y = 0$.

(b) Correctly aimed state, $Z = 0mm, \frac{BOTTOM}{SUM} = 0.9$.
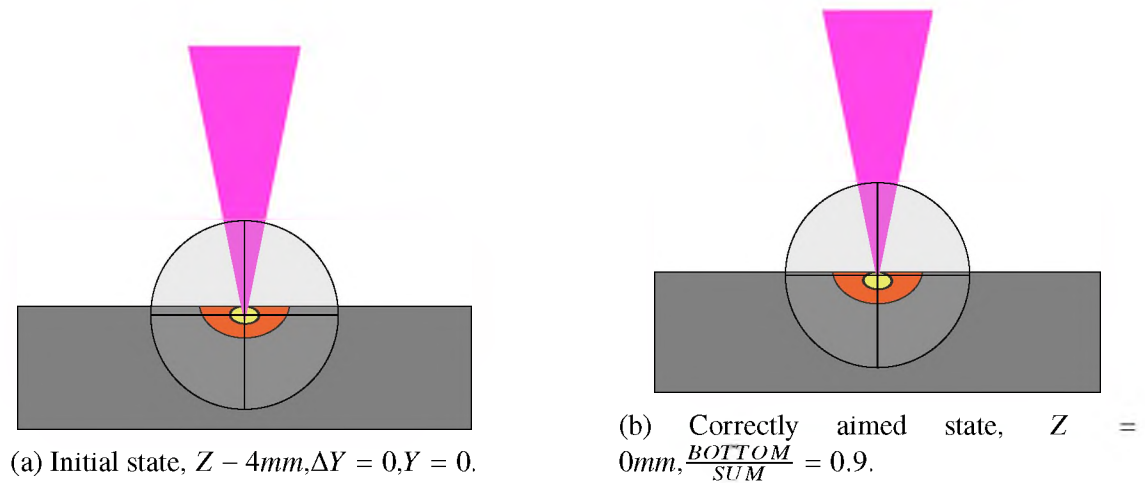
Figure 8.17. Feedback sensor aiming.

The positioning of the sensor relative to the additive process is illustrated in Figure 8.18a. A single sensor is sufficient for laser power feedback. However, simulations of the sensor functionality have shown the single sensor setup is only a partial solution for height control due to the height measurement being confounded with motion towards and away from the sensor. A single sensor unit is sufficient for simple unidirectional thin wall deposits that are typical in materials research. In fact, a single sensor was used for the demonstration presented in Section 8.27. However, the general usage case is for arbitrary geometry. An arrangement of three sensors arrayed around the deposition axis, as shown in Figure 8.18b, provides sufficient information to make the correct height measurement in all cases.

8.3.1. Feedback Sensor Simulation. A simulation was created to discern how to interpret the sensor signal and to inform the placement of the sensor within the additive environment. This simulation uses a ray tracing package to simulate the image of the additive process incident on the sensor's active area, then a python script to simulate the

(a) Single sensor positioning w.r.t. the additive process.

(b) Even distribution of sensors about the deposition axis.
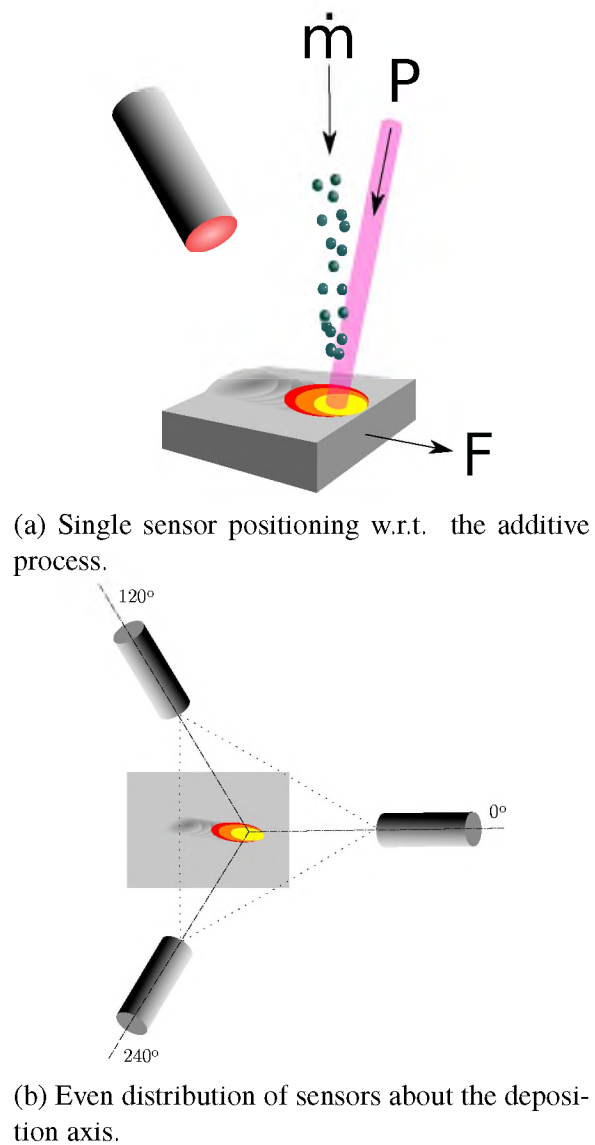
Figure 8.18. Deposition process sensor configuration within an additive system.

sensor's output signals from the incident image. Figure 8.19 shows a set of views created by simulating the optic axes of each sensor position. Figure 8.20 shows the expected SUM signal for selected materials and temperatures for use in laser power feedback control.
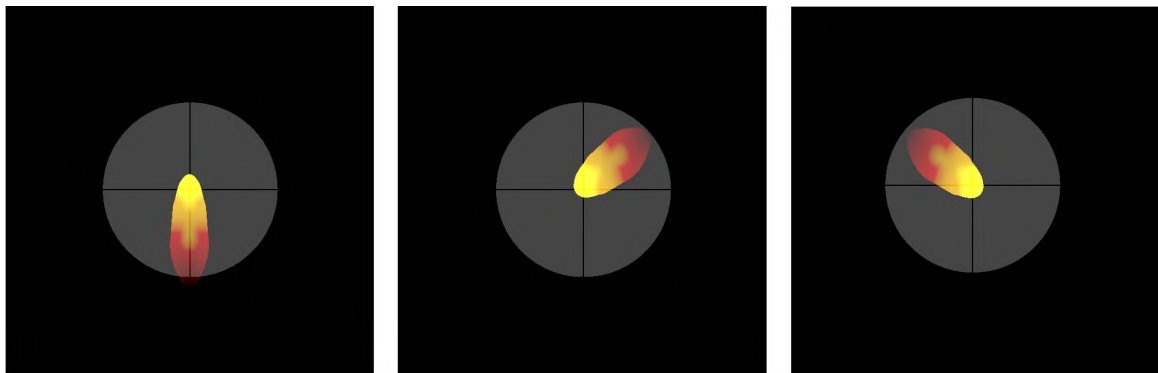
(a) Sensor 0, 0° orientation.   (b) Sensor 0, 120° orientation.   (c) Sensor 240, 0° orientation.

Figure 8.19. Simulated sensor viewpoints from selected orientations.
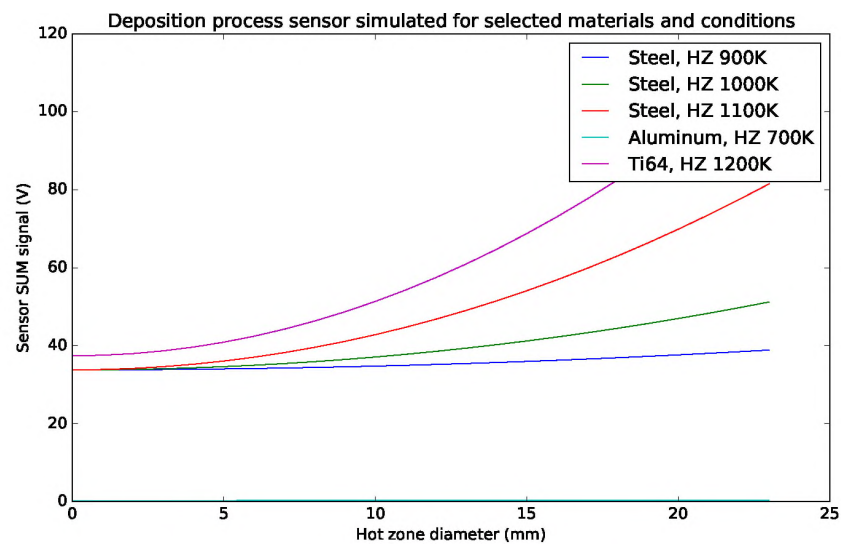
Figure 8.20. Simulated sensor signal for selected materials and temperatures.

During a laser deposition process, a tail of hot material trails the laser spot. Depending upon processing conditions and material properties, the melt pool itself can extend well past the boundaries of the laser spot. This leads to the height measurement being confounded with the effects from motions that align with the Y direction of the sensor when projected into the sensor's image plane. This effect can be seen in the single sensor responses plotted in Figure 8.21a shows the response when the motion is aligned to maximize the problem. Figure 8.21b illustrates a partial obfuscation. Finally, Figure 8.21c shows an orientation

which minimizes the issue. By using an evenly spaced array of three sensors, a composite signal (simply the minimum Y signal from the three sensors) can clear up any confusion by selecting the least confounded result of the measurements. Note the simulations used the raw Y signal value while the later testing indicated that the BOTTOM/SUM composite value provided a better measurement. Still, the observation that a minimum of three sensors will be necessary to capture the correct height signal in non-trivial cases.
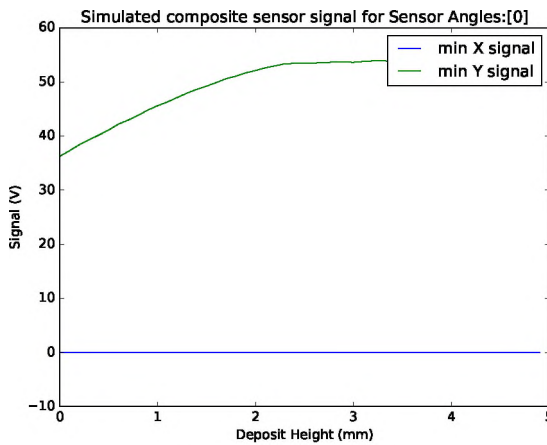
(a) Single sensor at 0°.
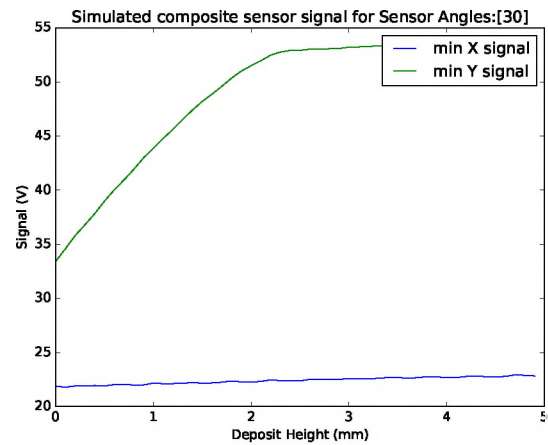
(b) Single sensor at 30°.
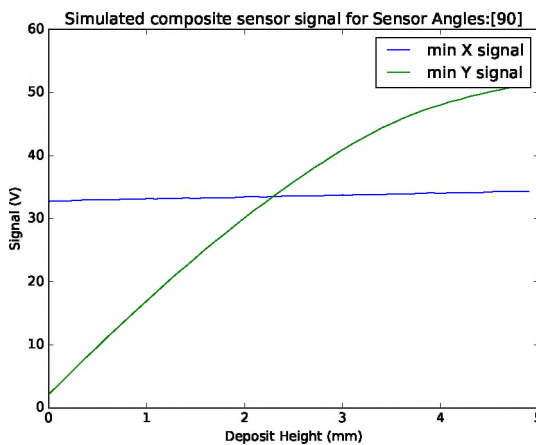
(c) Single sensor at 90°.
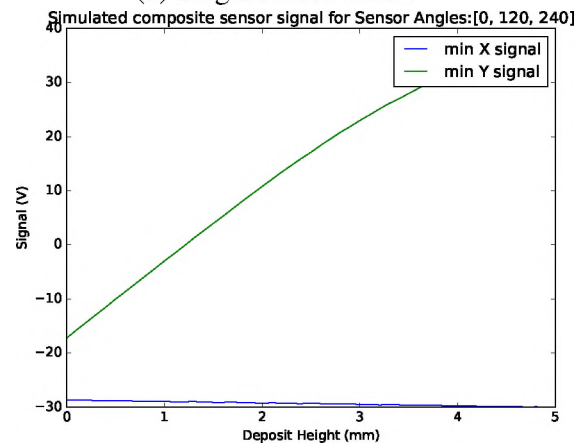
(d) Composite result obtained by using the minimum Y signal from three sensors at 20°, 140°, and 260°.

Figure 8.21. Height sensing using the deposition process sensor - The stated angle is w.r.t the +X axis. All sensors are placed at a 60°angle of inclination w.r.t the XY plane.

The quadrant overlays illustrate how the incident radiation would fall on each individual photodiode pad. To make use of the signals acquired by the sensors, some sensor fusion must be done, as illustrated in Figure 8.22. The resultant process estimators are:

- *Hot zone centroid* - An estimator for the location of the centroid of the hot zone (i.e. the melt pool and its immediate surroundings) w.r.t. the working point can be computed by doing a weighted sum as shown in equation 8.39.

$$C = \sum_{n=1}^{3} X_n \hat{x}_n \qquad (8.39)$$

where:

- C is the centroid estimator

- X_n is the X signal from sensor n

- $\hat{x}_n$ is the direction of the x axis in the image plane of sensor n

- *Deposition height estimator* - If the y axis of each sensor's image plane, $\hat{y}_n$, has some component in the system's Z axis, as articulated in equation 8.40, an estimator for the current melt pool location w.r.t to the processing head, and thus the deposition height, can be attained by a simple maximum of the Y signals from each sensor unit.

$$\hat{y}_n \cdot \hat{Z} \neq 0 \qquad (8.40)$$

- *Hot zone enthalpy estimator* - The sensor unit with the best view of the hot zone will have the highest SUM signal in the array. For this reason, the maximum of all of the SUM signals serves as an estimator for the hot zone size, and thus the enthalpy present in the hot zone.
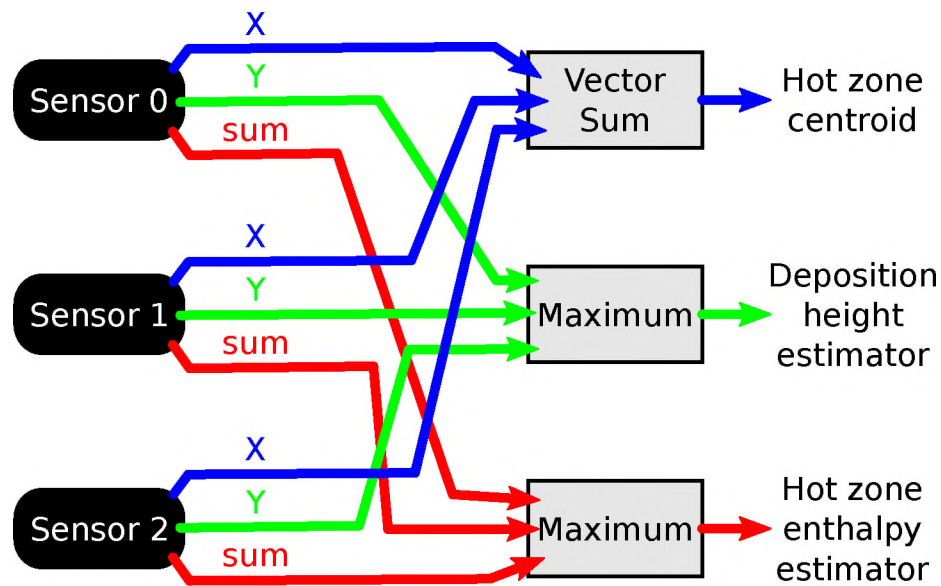
Figure 8.22. Sensor fusion logic for producing 3 process state estimators from raw sensor data.

The feedback system has been integrated into the deposition control system. Figure 8.23a shows the flow of information in the control system. The control scheme concept can be outlined as:

- A desired machine feed rate (F), powder flow rate ($\dot{m}$), laser power (P), and layer thickness (h) come from a part program or user input. These form the initial settings for those parameters.

- The Deposition Process Sensor subsystem uses the SUM measurement to make a suggested change to the laser power (ΔP) at a high rate (100Hz - 1kHz was found to be sufficient in prior implementations).

- The Deposition Process Sensor subsystem uses the composite Y measurement to adjust the feed rate (ΔF) of the machine. This feed rate update can happen an order of magnitude slower than the laser power update.

- The Deposition Process Sensor subsystem uses the difference between the desired feed rate and the current feed rate to adjust the mass flow rate of the powder feeder ($\Delta \dot{m}$). This update should happen an order of magnitude slower than the feed rate update. This loop is displayed in green in Figure 8.23a to denote that it is still an item in process.

The objective of this control scheme is to alleviate the need to be absolutely perfect in pre-planning process parameters. The feed rate is allowed to adjust to keep the build height consistent. The powder mass flow rate is allowed to adjust so that the feedback system can drive the needed feed rate closer to the desired rate. In short, the ΔF adjustment helps to fix high frequency issues while the $\Delta \dot{m}$ adjustment keeps the mean flow rate correct over time. This is all made possible by having the laser on its own feedback loop to control the input energy. A bench test rig, seen in Figure 8.23b using three of the Deposition Process Sensors has been constructed to aid the development of the sensor electronics.
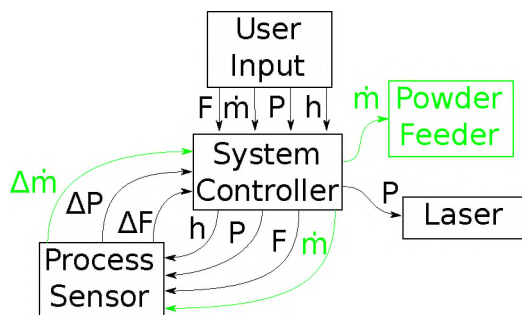
(a) Flow of information in the controls implementation. The loop for the powder flow, displayed in green has yet to be implemented.

(b) Triple sensor test bench setup.

Figure 8.23. Preparatory work for in-situ monitoring and controls.

The scheme described in Figure 8.24 separates the control of the additive equipment from the CNC or robot used for the motion system by partitioning the additive feedback controls into a state-based deposition process control system. This arrangement alleviates the need to have a custom CNC machine controller, which greatly increases the portability of the additive repair solution. This system imposes 2 requirements on the motion system:

1. The motion controller must be able to pass state information to the deposition process controller; and 2. The motion system controller must accept external input for modifying the speed at which it is traversing the path. There are several ways to satisfy these communication requirements so we feel that most vendors will be able to satisfy the requirements with the appropriate options package for the controller.
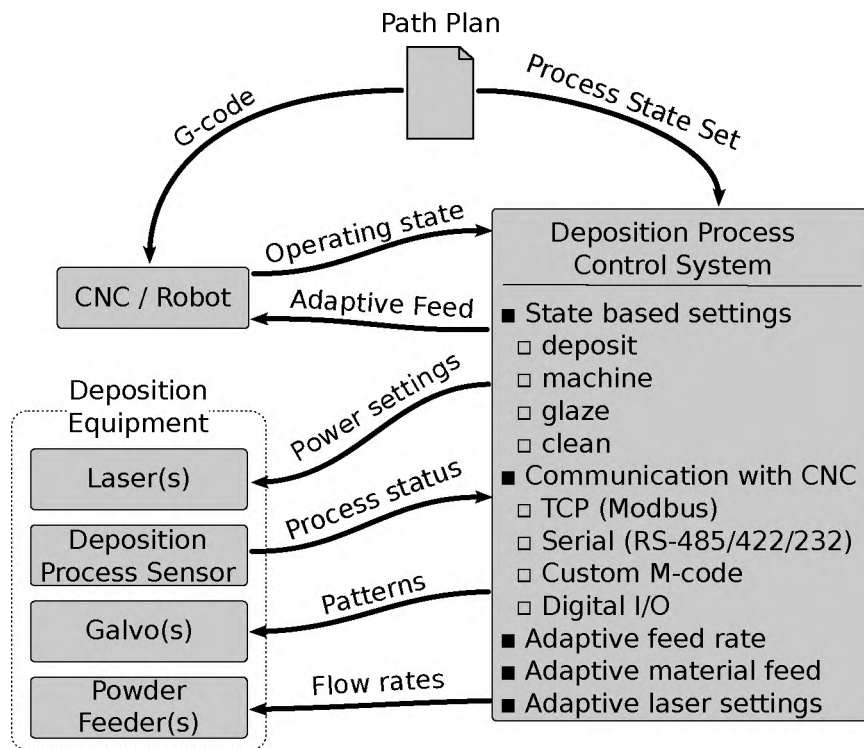
Figure 8.24. Integration scheme for a hybrid metal additive system using a state-based additive control system with minimal requirements on the CNC/Robot integration target for maximum flexibility.

A prototype application has been developed for visualizing the sensor fusion seen in Figure 8.22 and then using that information to make process decisions. Laser power, feed rate, and powder flow are adjusted so that the layer thickness and bead width remain within tolerance. This scheme was chosen because those three parameters can be adjusted on the fly without altering the path given to the CNC machine. This application, pictured in Figure 8.25, performs the following functions:

- *100 Hz* - The hot zone enthalpy estimator is used to adjust the laser power via a simple proportional control scheme. Updating the laser power via feedback allows the system to adjust for varying heat transfer conditions as the part is building. Feedback control for laser power is also the basic requirement for adjusting the other system parameters. (i.e. If the machine slows down, the melt pool will grow in volume if the laser power is not reduced.)

- *10 Hz* - A running average of the deposition height estimator is used to adjust the CNC machine's feed rate.

- *0.1 Hz* - The CNC machine's feed rate differential from nominal is used to adjust the powder flow rate.

It should be noted that all of the parameter adjustment numbers shown on the screen shot in Figure 8.25 are 0%-200% values used to scale the preprogrammed nominal parameter values. This arrangement keeps the parameter values within physically reasonable ranges. In practice, we were forced to restrict the system from coming to a full stop at 0% feed as this tended to induce a height error in the deposit that was not always recoverable. The main objective of the control scheme is to try to build the desired layer thickness and bead width at the desired cooling rate. By slowly adjusting the powder flow based on the feed rate, the system attempts to drive the feed rate back to the programmed value so that the cooling rate can approximate the desired value, or is at least consistent. This is critical as cooling rate is a significant driver of material properties in metal additive processes.

8.3.2. Feedback Sensor Tuning and Testing. A simple thin wall deposit of H13 tool steel onto mild steel was used to test the efficacy of the feedback system. This was done because it is a simple geometry to program and analyze as well as a fairly difficult test for the feedback system due to the frequent disruption in the steady state from both the direction reversal and shift in the Z axis. The extra time spent at the ends for the deceleration and Z level shift causes both additional powder and laser power to be dumped
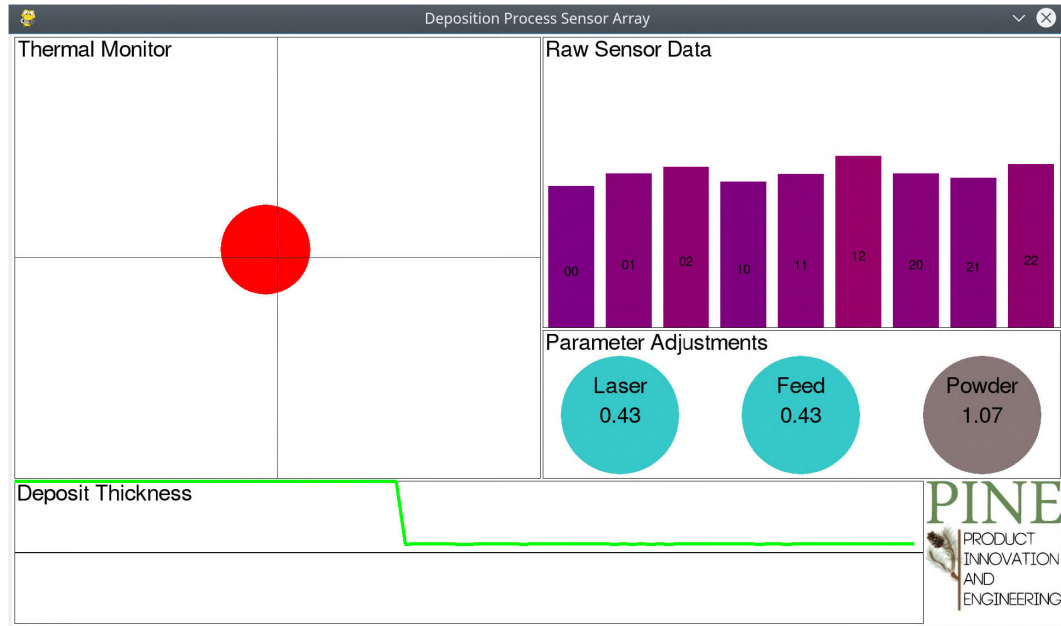
Figure 8.25. Sensor application screen shot taken using a candle flame as the IR source being tracked.

into the ends of the thin wall. Figure 8.26 shows one of the many iterations of test plates used to tune the PID controllers for both laser power and feed rate. The final proportional, integral, and derivative values arrived at after tuning are shown in Table 8.1. Note that for both controllers the derivative value is 0. We think that some derivative component may be valuable for the height control system to be a little more proactive, but the noise in the signal from hot powder in the scene renders any derivative component untenable.

Table 8.1. PID controller parameters.

	Power	Height
Proportional	3.5	1000
Integral	0.5	500
Derivative	0.0	0.0

An example of a completely uncontrolled thin wall deposit using static deposition parameters can be seen in Figure 8.27a. A set of three thin wall deposits are also shown in Figure 8.27 illustrating the progress garnered while tuning the feedback loop. Figure 8.27b represents one of the early depositions made with the system enabled. Figure 8.27c

Figure 8.26. PID loop tuning for the feedback sensor required many iterations.

represents a sample taking from midway through the tuning process. Finally, Figure 8.27d shows the capabilities of the current best parameter set (Table 8.1) for the control system. Deposit height and width measurements are shown in Table 8.2. Figure 8.28 shows a sample of the signal stream from the PID loops for both the height and power feedback loops taken when depositing the specimen in Figure 8.27d.

Table 8.2. Feedback system comparison

	height (mm)	width (mm)
design	12.0	2.5
OFF	14.7-18.2	3.4-4.9
FIRST	14.1-14.9	2.5-5.1
MIDWAY	13.6-14.2	2.2-3.3
FINAL	13.3-13.5	2.1-4.8

(a) OFF: Thin wall deposit with static parameters.

(b) FIRST: Thin wall deposit with the feedback system on, prior to PID loop fine tuning.
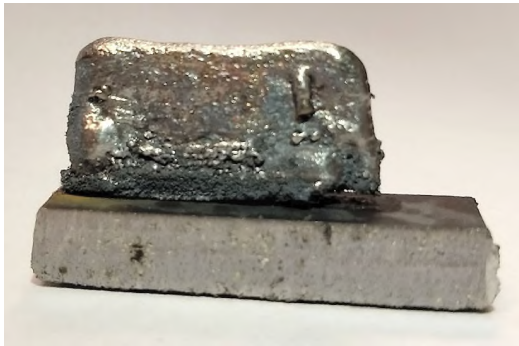
(c) MIDWAY: A thin wall deposit sampled during PID loop tuning. Note the delamination on the base layer at the right side.

(d) FINAL: A thin wall deposit after the PID loop tuning.

Figure 8.27. Sample deposits demonstrating the effect of the feedback system.
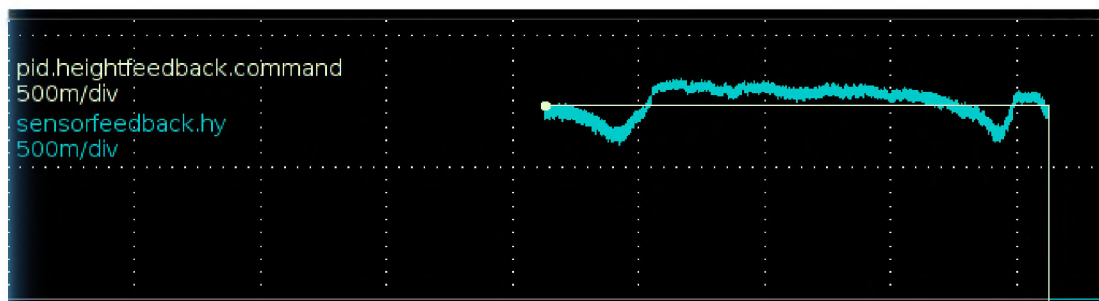
(a) Data from the height feedback PID loop
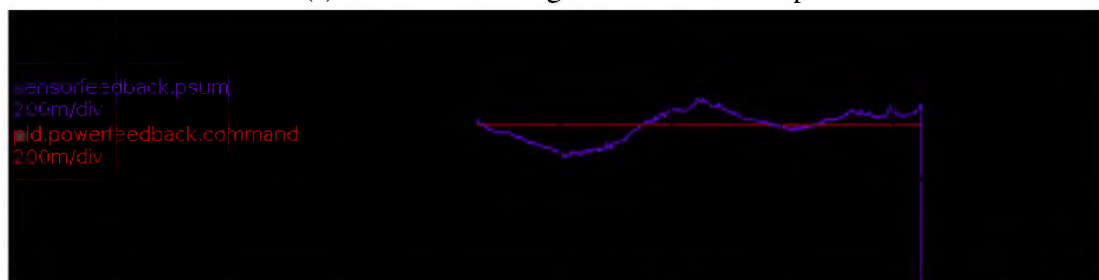
(b) Data from the power feedback PID loop

Figure 8.28. Data from the feedback controllers taken during the deposition of the FINAL sample from Figure 8.27d.

9. CONCLUSIONS

Additive manufacturing (AM) technologies have played a critical role in providing industries with a strategic business approach that stretches from product concept development to the manufacture of the product and to the end of the life of product. As a logistical advantage, an inventory of service parts can potentially be replaced with inventories of feedstock material, thus can greatly reduce the need for spare parts and the associated space. This work makes possible the automation of part restoration, which will lead to robust, high quality repairs that are critical for restoration process qualification.

Due to the complexity of part damage or wear conditions, a large degree of manual operations are necessary in the current repair practice, which introduces inconsistency in repair quality and dependency on experienced process experts. As techniques develop and part complexity increases, the knowledge requirement on the human side also increases, which can be very onerous for non-trivial parts. Increased automation lowers the technology threshold for personnel education and provides a quick response to a repair request. Inventory of parts can potentially be replaced with inventories of feedstock material.

This research presents a computational framework for addressing AM problems, including repair, by deeply integrating the entire work flow from geometry to the printing process. This is accomplished through a massively parallel, thread-safe computational framework where individual processes share information via standardized data structures kept in a key:value pair back end. This enables automated work flows that include preperatory steps such as on-machine scannning, intermediary steps such as optimization of path planning (e.g. Section 7) and process parameter estimation (e.g. Section 8.2), and preparation of data for on-machine feedback or monitoring (e.g. the feedback sensing discussed

in Section 8.3). Additionally, non-CAD driven planning techniques, such as the method discussed in Section 7.5, can empower end users in the ongoing right-to-repair fight by removing the reliance on OEM data.

APPENDIX

A SAMPLE HYBRID REPAIR APPLICATION

A possible procedure used to repair the an tool steel diecast core would proceed as follows as follows:

1. Clean the object's surface of foreign materials. - As seen in Figure 1a, below, there was a significant amount of aluminum adhered to the surface of an insert core. While a small wt% of aluminum might give a steel some precipitate hardening, a generous amount of aluminum would make the structure quite brittle. Thus, the core required some surface prep to remove the aluminum. A wire wheel on an angle grinder, proved to be effective, as shown below in Figure 1.

(a) Core surface as-received.

(b) Core surface after processing with a wire wheel.

Figure 1. Removing the aluminum from the surface of the H13 core.

2. Prepare the CAD model for additive process planning. - The model provided by Toyota was brought into NX, as shown in Figure 2a. The model was simplified to represent only the data we needed to pass to the additive process planner. Additionally, there was a groove around the base of the model that was not present in the physical article, so this was also removed. The resultant model is shown in Figure 2b.
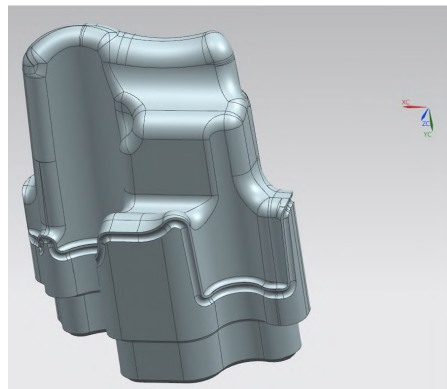
(a) Core model as-received.
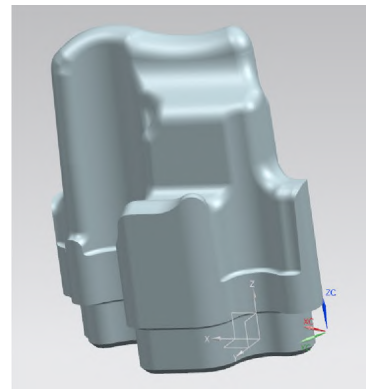
(b) Core model after removing unnecessary geometry and selecting a coordinate system.

Figure 2. CAD prep work

3. Design and fabricate a fixture to hold the object. - The bottom surface of the core has 2 holes for water lines and one large tapped hole. The fixture, as shown in Figure 3, uses the tapped hole to hold the core against a surface and the two water line holes to constrain translation and rotation in the plane of that surface.

4. Compute a process plan. For the purposes of this discussion, process planning is divided into the following four activities:

   (a) Import and convert the model - CAD formats contain a lot of extra data not needed for the subsequent steps in this process. This step strips all unnecessary and redundant data to streamline the model for the math necessary in the later steps.

Figure 3. Aluminum fixture machined to hold the core on a 5th axis trunnion.

(b) Slice - In this step, a series of parallel planes are used to cut the model to generate the shapes of the contours that will later be deposited. Theoretically, these planes should be equidistant from each other. In practice, this can lead to issues when the model is sliced directly at a facet vertex or through a facet parallel to the slice plane. To avoid this situation, cut level analysis, a technique from machining CAM processing, is employed. The cut level analysis detects problem slices and adjusts their plane positions by a minute amount to avoid the numerical instability.

(c) Process plan - The process planning step takes the slice data and generates the both the sequence in which the contours are covered and the approach directions. For this repair activity, a simple weighted average of a few measured items was used to calculate a collision-free set of approach directions.

(d) Post process - Analogous to CNC machining, the additive post processor's function is to take the machine-independent path plan and generate machine-specific NC code. This is the step where any machine-specific idiosyncrasies are compensated for. For example, in order to avoid path following errors due to
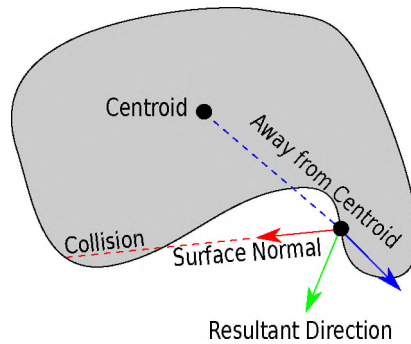
Figure 4. Laser approach direction determination.

axis acceleration issues, the underpowered motion system in the present system requires large approach direction changes to be decoupled from speed-controlled 5 axis linear motions.

The following parameters were used to generate the gcode:

- *Feed Rate:* 200 mm/minute

- *Laser:* 0 (a 500W Nd:YAG laser)

- *Laser Power:* 500 W

- *Bead Width:* 2mm

- *Powder Flow:* ≈ 5.5 grams/minute of H13

5. Test. - When developing new process planning routines, copious testing is in order. There were many iterations between coding for the path plan and testing on PINE's controller, shown below in Figure 5. The final test is, of course, a dry run.

6. Execute. - Once the code can pass a dry run, it is time to deposit. For the first layer, the part was protected with an oven bag in an attempt to keep argon near the process as much as possible. This initial setup is shown in Figure 6.
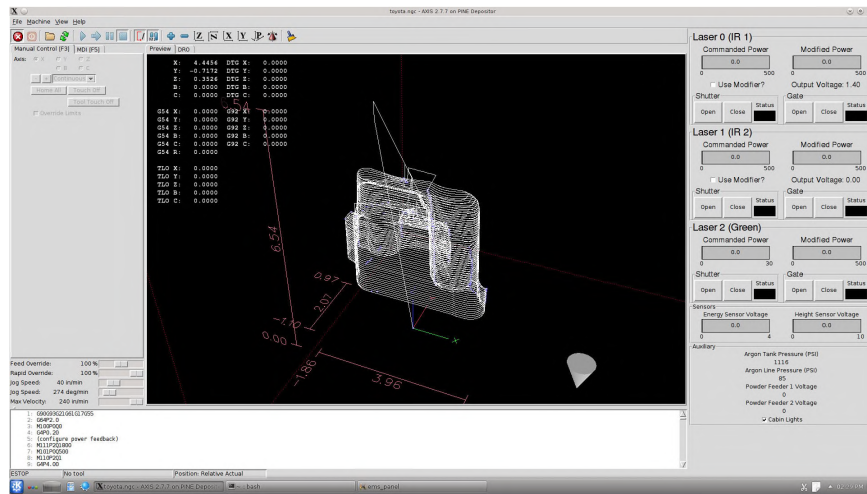
Figure 5. A portion of the core repair code shown in A LINUX CNC UI.

Figure 6. Depositing the first layer inside an oven bag argon shield.

REFERENCES

[1]   Mustafa Awd et al. "Very high-cycle fatigue properties and microstructural damage mechanisms of selective laser melted AlSi10Mg alloy." In: *International Journal of Fatigue* 124 (2019), pp. 55–69. DOI: `10.1016/j.ijfatigue.2019.02.040`.

[2]   Bert Bras and Mark W. McIntosh. "Product, process, and organizational design for remanufacturing- an overview of research." In: *Robotics and Computer Integrated Manufacturing* (1999), pp. 167–178.

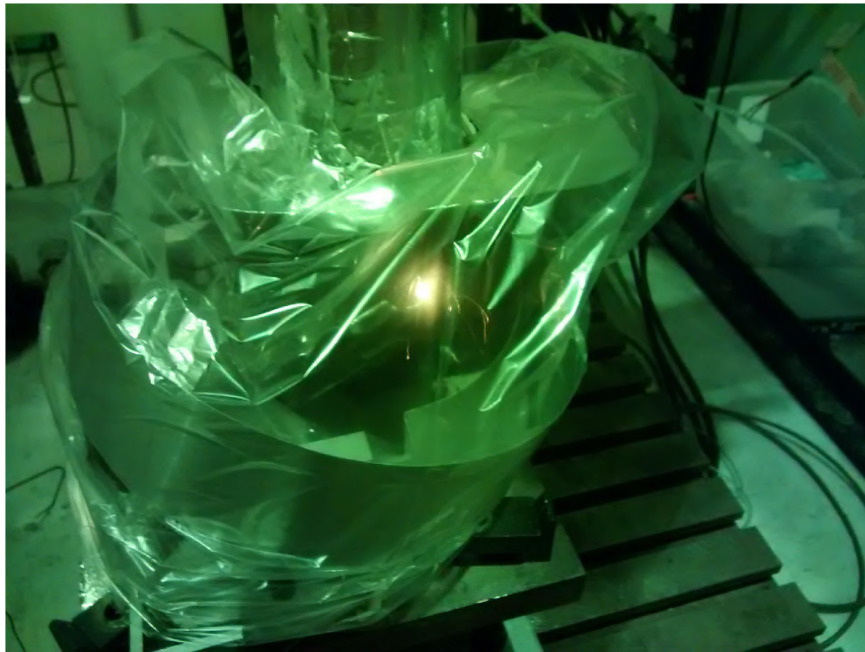[3]   Hahn Choo et al. "Effect of laser power on defect, texture, and microstructure of a laser powder bed fusion processed 316L stainless steel." In: *Materials & Design* 164 (2019), p. 107534. DOI: `10.1016/j.matdes.2018.12.006`.

[4]   Sean P. Donegan, Edwin J. Schwalbach, and Michael A. Groeber. "Zoning additive manufacturing process histories using unsupervised machine learning." In: *Materials Characterization* 161 (Mar. 2020), p. 110123. DOI: `10.1016/j.matchar.2020.110123`. URL: `https://doi.org/10.1016%2Fj.matchar.2020.110123`.

[5]   Kunnayut Eiamsa-ard et al. "Part Repair using a Hybrid Manufacturing System." In: *Proceedings of the Sixteenth Annual Solid Freeform Fabrication Symposium.* Austin, TX, Aug. 2005.

[6]   Wesley Everhart, Joseph Dinardo, and Christian Barr. "The Effect of Scan Length on the Structure and Mechanical Properties of Electron Beam-Melted Ti-6Al-4V." In: *Metallurgical and Materials Transactions A* 48.2 (Nov. 2016), pp. 697–705. DOI: `10.1007/s11661-016-3866-z`. URL: `https://doi.org/10.1007%2Fs11661-016-3866-z`.

[7]   Miranda Fateri, Jan-Steffen Hotter, and Andreas Gebhardt. "Experimental and Theoretical Investigation of Buckling Deformation of Fabricated Objects by Selective Laser Melting." In: *Physics Procedia* 39 (2012), pp. 464–470. DOI: `10.1016/j.phpro.2012.10.062`.

[8]   William E. Frazier, Donald Polakovics, and Wayne Koegel. "Qualifying of metallic materials and structures for aerospace applications." In: *JOM* 53.3 (Mar. 2001), pp. 16–18. DOI: `10.1007/s11837-001-0171-z`. URL: `https://doi.org/10.1007/s11837-001-0171-z`.

[9]   Haijun Gong et al. "The effects of processing parameters on defect regularity in Ti-6Al-4V parts fabricated by selective laser melting and electron beam melting." In: *24th Annual International Solid Freeform Fabrication Symposium—An Additive Manufacturing Conference, Austin, TX*. 2013, pp. 12–14.

[10]   T. Gonzalez. "Remanufacturing Technology." MA thesis. Massachusetts Institute of Technology, 1983.

[11]   Marco Grasso, Francesco Gallina, and Bianca Maria Colosimo. "Data fusion methods for statistical process monitoring and quality characterization in metal additive manufacturing." In: *Procedia CIRP* 75 (2018), pp. 103–107. DOI: `10.1016/j.procir.2018.04.045`. URL: `https://doi.org/10.1016%2Fj.procir.2018.04.045`.

[12]   H. Holzwasser. "Engineering for Remanufacturing." In: *SAE Technical Paper Series* (1983), No. 830549.

[13]   *Is Hybrid Manufacturing Technology the Future of Additive Manufacturing?* July 2018. URL: `https://amfg.ai/2018/07/10/hybrid-technology-the-future-of-manufacturing/`.

[14]   J.L. Koch and J. Mazumder. "Rapid Prototyping by Laser Cladding." In: *The International Society for Optical Engineering* 2306 (1993), p. 556.

[15]   R. Kutta. "Remanufacture of durable products: a value-preserving technology." MA thesis. Massachusetts Institute of Technology, 1980.

[16]   James Laeng, Jennifer Stewart, and Frank W. Liou. "Laser Metal Forming Processes For Rapid Prototyping – A Review." In: *International Journal of Production Research* 38.16 (2000), pp. 3973–3966.

[17]   Maija Leino, Joonas Pekkarinen, and Risto Soukka. "The Role of Laser Additive Manufacturing Methods of Metals in Repair, Refurbishment and Remanufacturing – Enabling Circular Economy." In: *Physics Procedia* 83 (2016), pp. 752–760. DOI: `10.1016/j.phpro.2016.08.077`. URL: `https://doi.org/10.1016%2Fj.phpro.2016.08.077`.

[18]   P. Li et al. "Towards predicting differences in fatigue performance of laser powder bed fused Ti-6Al-4V coupons from the same build." In: *International Journal of Fatigue* 126 (2019), pp. 284–296. DOI: `10.1016/j.ijfatigue.2019.05.004`.

[19]   Frank W. Liou. "A Multi-Axis Rapid Prototyping System." In: *SME Rapid Prototyping and Manufacturing Conference*. Apr. 1999, p. 565.

[20]   Frank W. Liou et al. "A Multi-Axis Hybrid Manufacturing Process." In: *Proceedings of the 2004 NSF Design and Manufacturing Grantees Conference*. 2004.

[21]   Frank W. Liou et al. "Development of a Precision Rapid Metal Forming Process." In: *Proceedings of the Eleventh Annual Solid Freeform Fabrication Symposium*. Austin, TX, Aug. 2000, pp. 362–368.

[22]   Frank W. Liou et al. "Research and Development of a Hybrid Rapid Manufacturing Process." In: *Proceedings of the Twelfth Annual Solid Freeform Fabrication Symposium*. Austin, TX, Aug. 2001, p. 138.

[23]   R. Lund. *Remanufacturing, United States experience and implications for developing nations*. Tech. rep. MIT Center for Policy Alternatives Report, CPA/83-17, 1983.

[24]   YW Luo et al. "Detecting void-induced scatter of fatigue life of selective laser melting-fabricated inconel 718 using miniature specimens." In: *Materials Research Express* (2019).

[25]   Zhibo Luo and Yaoyao Zhao. "A survey of finite element analysis of temperature and thermal stress fields in powder bed fusion Additive Manufacturing." In: *Additive Manufacturing* 21 (May 2018), pp. 318–332. DOI: 10.1016/j.addma.2018.03.022. URL: https://doi.org/10.1016%2Fj.addma.2018.03.022.

[26]   J. Mazumder et al. "Direct Metal Deposition Of H13 Tool Steel for 3-D Components: Microstructure and Mechanical Properties." In: *Journal of Metals* 49 (1997), pp. 55–60.

[27]   Sankhya Mohanty and Jesper H. Hattel. "Cellular scanning strategy for selective laser melting: Generating reliable, optimized scanning paths and processing parameters." In: *Laser 3D Manufacturing II* (2015). DOI: 10.1117/12.2079957.

[28]   Gunther Mohr et al. "In-Situ Defect Detection in Laser Powder Bed Fusion by Using Thermography and Optical Tomography—Comparison to Computed Tomography." In: *Metals* 10.1 (Sept. 2020), p. 103. DOI: 10.3390/met10010103.

[29]   David J. Newell et al. "Mitigation of scan strategy effects and material anisotropy through supersolvus annealing in LPBF IN718." In: *Materials Science and Engineering: A* 764 (Sept. 2019), p. 138230. DOI: 10.1016/j.msea.2019.138230. URL: https://doi.org/10.1016%2Fj.msea.2019.138230.

[30]   Bonny Onuike and Amit Bandyopadhyay. "Additive manufacturing in repair: Influence of processing parameters on properties of Inconel 718." In: *Materials Letters* 252 (Oct. 2019), pp. 256–259. DOI: 10.1016/j.matlet.2019.05.114. URL: https://doi.org/10.1016%2Fj.matlet.2019.05.114.

[31] Santanu Paul et al. "Critical deposition height for sustainable restoration via laser additive manufacturing." In: *Scientific Reports* 8.1 (2018). DOI: 10.1038/s41598-018-32842-z.

[32] A. D. Peralta et al. "Towards rapid qualification of powder-bed laser additively manufactured parts." In: *Integrating Materials and Manufacturing Innovation* 5.1 (May 2016), pp. 154–176. DOI: 10.1186/s40192-016-0052-5. URL: https://doi.org/10.1186%2Fs40192-016-0052-5.

[33] L. Portolés et al. "A qualification procedure to manufacture and repair aerospace parts with electron beam melting." In: *Journal of Manufacturing Systems* 41 (Oct. 2016), pp. 65–75. DOI: 10.1016/j.jmsy.2016.07.002. URL: https://doi.org/10.1016%2Fj.jmsy.2016.07.002.

[34] N. Raghunath and Pulak M. Pandey. "Improving accuracy through shrinkage modelling by using Taguchi method in selective laser sintering." In: *International Journal of Machine Tools and Manufacture* 47.6 (2007), pp. 986–995. DOI: 10.1016/j.ijmachtools.2006.07.001.

[35] Karl-Hermann Richter, Sven Orban, and Steffan Nowotny. "Laser Cladding of The Titanium Alloy Ti6242 to Restore Damaged Blades." In: *Proceedings of the 23rd International Congress on Applications of Lasers and Electro-Optics*. 2004.

[36] Jianzhong Ruan and Frank W. Liou. "Automatic Toolpath Generation For Multi-Axis Surface Machining In A Hybrid Manufacturing Systemg." In: *Proceedings of the 2003 ASME Design Automation Conference*. Paper No. DAC-48780. Chicago, Illinois, Sept. 2003.

[37] Jianzhong Ruan, Jun Zhang, and Frank W. Liou. "Support Structures Extraction For Hybrid Layered Manufacturing." In: *DETC*. 2001.

[38] Jianzhong Ruan et al. "Automatic Process Planning of A Multi-Axis Hybrid Manufacturing System." In: *DETC*. Montreal, Canada, Sept. 2002.

[39] Luke Scime and Jack Beuth. "A multi-scale convolutional neural network for autonomous anomaly detection and classification in a laser powder bed fusion additive manufacturing process." In: *Additive Manufacturing* 24 (Dec. 2018), pp. 273–286. DOI: 10.1016/j.addma.2018.09.034. URL: https://doi.org/10.1016%2Fj.addma.2018.09.034.

[40] Shafaqat Siddique et al. "Computed tomography for characterization of fatigue performance of selective laser melted parts." In: *Materials & Design* 83 (2015), pp. 661–669. DOI: 10.1016/j.matdes.2015.06.063.

[41] Todd Sparks, Heng Pan, and Frank W. Liou. "Determination of Dynamic Powder Modeling Parameters via Optical Methods." In: *Proceedings of the Sixteenth Annual Solid Freeform Fabrication Symposium*. Austin, TX, Aug. 2005.

[42] Todd Sparks, Heng Pan, and Frank W. Liou. "Development of Image Processing Tools for Analysis of Laser Deposition Experiments." In: *Proceedings of the Fifteenth Annual Solid Freeform Fabrication Symposium*. Austin, TX, Aug. 2004.

[43] S. Tammas-Williams et al. "The Influence of Porosity on Fatigue Crack Initiation in Additively Manufactured Titanium Components." In: *Scientific Reports* 7.1 (Apr. 2017). DOI: 10.1038/s41598-017-06504-5.

[44] Di Wang et al. "The Effect of a Scanning Strategy on the Residual Stress of 316L Steel Parts Fabricated by Selective Laser Melting (SLM)." In: *Materials* 11.10 (Sept. 2018), p. 1821. DOI: 10.3390/ma11101821. URL: https://doi.org/10.3390%2Fma11101821.

[45] Di Wang et al. "The Effect of a Scanning Strategy on the Residual Stress of 316L Steel Parts Fabricated by Selective Laser Melting (SLM)." In: *Materials* 11.10 (2018), p. 1821. DOI: 10.3390/ma11101821.

[46] P.j. Withers and H.k.d.h. Bhadeshia. "Residual stress. Part 2 - Nature and origins." In: *Materials Science and Technology* 17.4 (2001), pp. 366–375. DOI: 10.1179/026708301101510087.

[47] Bin Zhang, Shunyu Liu, and Yung C. Shin. "In-Process monitoring of porosity during laser additive manufacturing process." In: *Additive Manufacturing* 28 (Aug. 2019), pp. 497–505. DOI: 10.1016/j.addma.2019.05.030. URL: https://doi.org/10.1016%2Fj.addma.2019.05.030.

VITA

Todd Eugene Sparks has served as the R&D Director at Product Innovation and Engineering (PINE) since 2018. He has served as an industrial board member for the Center for Aerospace Manufacturing Technologies at S&T, since 2008. He has published over 60 technical publications in metal additive manufacturing area, including modeling, repair and restoration, and process monitoring. He recieved his PhD in Mechanical Engineering from Missouri University of Scient & Technology in August of 2020.

Relevant Awards:

- US Patent US9573224B2, "System and method for determining beam power level along an additive deposition path", granted 2017

- US Patent US10632566B2,"System and method for controlling the input energy from an energy point source during metal processing", granted 2020

- US Patent US9757902B2, "Additive layering method using improved build description", granted 2017